Modeled air-sea interactions around southeastern Greenland during extreme mesoscale wind events

by

Alice K. DuVivier

B.A., The Colorado College, 2008

M.S., University of Colorado, 2012

A thesis submitted to the

Faculty of the Graduate School of the

University of Colorado in partial fulfillment

of the requirement for the degree of

Doctor of Philosophy

Department of Atmospheric and Oceanic Sciences

2015

This thesis entitled:

Modeled air-sea interactions around southeastern Greenland during extreme mesoscale wind events

written by Alice K. DuVivier

Has been approved for the Department of Atmospheric and Oceanic Sciences

_____

John J. Cassano

_____

Nicole S. Lovenduski

Date _____

The final copy of this thesis has been examined by the signatories, and we find that both the content and the form meet acceptable presentation standards of scholarly work in the above mentioned discipline.

Abstract

DuVivier, Alice K. (Ph.D., Department of Atmospheric and Oceanic Sciences)

Modeled air-sea interactions around southeastern Greenland during extreme mesoscale wind events

Thesis directed by Associate Professor John J. Cassano

The coast along the southern tip of Greenland is one of the windiest locations in the world due to strong mesoscale barrier winds and tip jets that form when synoptic scale flow interacts with the topography of Greenland. This study addresses how modeled mesoscale wind events around southeastern Greenland impact air-sea interactions and the ocean's response to this forcing. Case study comparisons between Weather Research and Forecasting (WRF) model simulations run at four different resolutions (100 km, 50 km, 25 km, 10 km), in-situ observations, and QuikSCAT satellite data indicate that resolutions of 50 km and higher explicitly represent mesoscale winds. However, 10 km resolution is required to capture the vertical and horizontal structure of wind jets and to produce the greatest magnitude latent and sensible heat fluxes.

The self-organizing map (SOM) algorithm was used to identify and classify the range of 10 m wind patterns present during ten winters (1997-2007, NDJFM) in the ECMWF Interim Reanalysis (ERA-I) and 50 km WRF simulation. WRF simulated patterns with strong barrier-parallel flow more frequently than ERA-I, and WRF also had faster coastal winds than ERA-I during all types of strong wind events. The largest turbulent flux differences occur over the marginal ice zone where the near-surface atmospheric state depends on specified sea ice thickness in each model. The SOM algorithm was then used to identify 12 wind patterns present

during 20 winters (1990-2010, NDJFM) in the fully coupled Regional Arctic System Model (RASM). For all wind patterns the ocean loses buoyancy, primarily from turbulent sensible and latent heat fluxes. Patterns with westerly winds at Cape Farewell had the largest buoyancy loss over the Irminger and Labrador Seas while patterns with easterly flow at Cape Farewell have large buoyancy loss along the sea ice edge in the Denmark Strait and a secondary maximum immediately west of Cape Farewell. The ocean mixed layer is anomalously deep for wind patterns that have northerly flow with either easterly or westerly winds at Cape Farewell; mixed layer deepening is positively correlated to the frequency of those patterns and of greater magnitude for longer duration events.

Acknowledgements

First and foremost, I would like to thank my adviser, John Cassano, for teaching me to be an inquisitive, methodical and thorough scientist. He has given me the chance to work as a professional scientist, provided the opportunity to experience fieldwork in Antarctica, shown me how to be a good teacher, and has patiently guided me through writing this dissertation. His enthusiasm for the Poles is infections, and I hope one day to be as productive and successful a scientist as he is.

I am also grateful to my committee members Bill Neff, Chris Fairall, Nikki Lovenduski, and Mark Serreze for their input and feedback throughout the research process, and their suggestions have helped improve this thesis. I would also like to recognize the collaboration and support of the RASM development team – in particular Mimi Hughes, Andrew Roberts and Tony Craig – without whom I would not have had nearly as much fun working on research or learned nearly as much about modeling, supercomputers, and other components of the Arctic climate system. I am also grateful to the Cassano group past and present: Melissa Nigro, Shelley Knuth, Mimi Hughes, Elizabeth Cassano, Matthew Higgins, Catrin Mills, Cody Phillips, David Porter, Keah Schuenemann, Mark Seefeldt, and Michael Stone. Besides being a fun and friendly bunch to work with, they have all helped me by talking through science results, computer hiccoughs, coding bugs, future career goals, and life outside of science. Thanks also to Brian Vanderwende and Jesse Nusbaumer for their friendly and continual help with classwork, computer issues, and for being my peers throughout the duration of graduate school.

This dissertation research was supported by a NOAA ESRL/CIRES graduate fellowship, teaching assistantships through the Department of Atmospheric and Oceanic Sciences at the

University of Colorado at Boulder, Department of Energy (DOE) grants DE-FG02-07ER64462 and DE-SC000617, National Science Foundation (NSF) grant PLR 1107788, and the Department of Defense (DoD) High Performance Computing Modernization Program.

I am so lucky to have such a supportive network of family and friends who have continually encouraged me throughout the dissertation process. Thank you all! In particular, I would like to thank Becky Poore for listening to me talk through scientific blocks, statistics, results, and for generally broadening my view of the climate system. My brother, Emmett Perl, has been a lifelong supporter and competitor, and has encouraged me to reach my maximum potential. My mom, K.K. DuVivier, has fostered my love of learning and writing and is a constant source of positivity and support. I know my mom is very proud of me and that my dad, Jim Perl, would also be proud of me as I earn my Ph.D. My dog, Sprite (for the lightning!), is a role model for loving unconditionally and always prioritizing sleep and fun. Thanks to my daughter, Lennox, for being a bright spot at the end of every day and for being generally happy and sleeping well so that the last night-time push to complete this dissertation was possible. And finally, thanks to my husband, Michael Rhodes, who always shows me new ways to think about the world and without whom I would not be able to complete this dissertation and still be nearly as calm, supported, well rested, and well fed.

Table of Contents

Table list

Figure list

Supplementary Figure List

Chapter 1: Introduction

The coast along the southern tip of Greenland is one of the windiest locations in the world [*Sampe and Xie*, 2007] due to orographically enhanced winds. Greenland's high terrain impacts the Northern Hemisphere circulation and North Atlantic Storm tracks [*Petersen et al.*, 2004; *Tsukernik et al.*, 2007], and the Icelandic Low that lies between Greenland's east coast and Iceland reflects the large number of synoptic cyclones that occur in the region [*Tsukernik et al.*, 2007]. As cyclones move toward Greenland, synoptic flow interacts with and is deflected by the terrain [*Renfrew et al.*, 2008]. As seen in Figure 1, the Greenland ice sheet has a maximum elevation of 3208 m at Summit with a secondary peak of 2800 m in the southern tip, and the southeastern coast is particularly rugged with steep cliffs rising sharply from sea level. The flow distortion due to Greenland's topography results in several types of mesoscale (20-200 km) wind events: katabatic winds, barrier winds, westerly tip jets, and northeasterly tip jets. Because katabatic winds occur primarily over land instead of over the oceans, like the other three types of mesoscale winds, this dissertation will not explore katabatic events in detail. The strong mesoscale winds are also a significant hazard to commercial shipping, military operations, and scientific field studies in the region [*Doyle and Shapiro*, 1999]. Additionally, and of particular importance for this dissertation, the powerful mesoscale winds occur over seas where the downwelling component of the ocean's meridional overturning circulation occurs, so it is important to thoroughly understand the role of these winds on this process important to the global heat budget [*Bacon et al.*, 2003; *Pickart et al.*, 2003a].

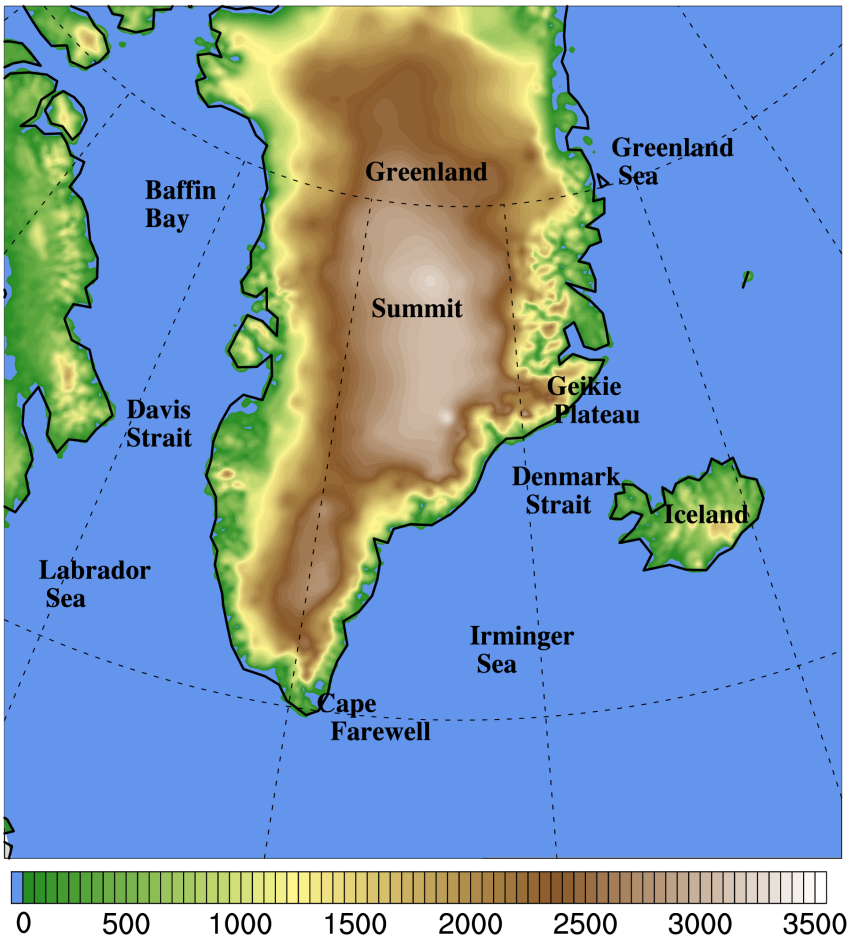

Figure 1: Greenland topography (m) and surrounding seas.

The barrier wind, westerly tip jet, and easterly tip jet events all occur along the southeast Greenland coast during winter months and can have surface wind speeds in excess of 25 m s^{-1} [*Moore*, 2003; *Moore and Renfrew*, 2005; *Sproson et al.*, 2008; *Våge et al.*, 2009; *Harden et al.*, 2011]. Barrier winds have been observed throughout the world where atmospheric flow interacts with steep topography (e.g. [*Parish*, 1982, n.d.; *Broeke et al.*, 2006; *Colle et al.*, 2006; *Loescher et al.*, 2006; *Nigro et al.*, 2012]). Barrier winds around Greenland occur when low-level cyclonic synoptic flow runs into the rugged southeast coast and the steep terrain blocks the air from flowing over the topography. This blocked air converges along the coast, causing a localized high-pressure region [*Doyle and Shapiro*, 1999; *Moore and Renfrew*, 2005] with a local pressure

gradient perpendicular to and away from the barrier. As the synoptic flow interacts with this local pressure gradient there is a directional shift to barrier-parallel northerly winds that are accelerated by the component of the pressure gradient along the jet [*Outten et al.*, 2009; *Petersen et al.*, 2009; *Ólafsson and Ágústsson*, 2009]. As a result of the frequent barrier flow, the southeast Greenland coast has high wind direction constancy [*Moore*, 2003; *Moore and Renfrew*, 2005].

Near Cape Farewell, however, there is low directional constancy in the average wind field [*Moore*, 2003; *Moore and Renfrew*, 2005] as a result of two dominant types of tip jets: easterly and westerly. Both types of tip jets are relatively short lived, shallow, and narrow bands of high wind speed that extend a few hundred kilometers out from the coast with maximum surface wind speeds up to 50 m s^{-1} – equivalent to category 3 hurricane wind speeds [*Moore*, 2003; *Moore and Renfrew*, 2005; *Våge et al.*, 2009]. The location of the driving synoptic cyclone center impacts what type of tip jet forms [*Moore*, 2003]. An easterly tip jet forms when a cyclone is located south of Cape Farwell, so when the barrier flow along the southeast coast of Greenland reaches Cape Farewell the local high pressure decreases and the pressure gradient aligns with the wind direction causing the air to accelerate [*Moore and Renfrew*, 2005; *Outten et al.*, 2009]. A westerly tip jet occurs when a cyclone center is located between Iceland and Greenland and air accelerates from the Labrador Sea around Cape Farewell or during orographic descent over the southern tip of Greenland [*Doyle and Shapiro*, 1999; *Moore and Renfrew*, 2005; *Våge et al.*, 2009].

During strong wind events the combination of fast wind speeds and large vertical temperature and moisture gradients between the cold, dry air and the relatively warmer ocean surface drive oceanic energy and buoyancy loss [*Petersen and Renfrew*, 2009; *Renfrew et al.*,

2009b; *Harden et al.*, 2011; *DuVivier and Cassano*, 2013; *Oltmanns et al.*, 2014]. Large turbulent heat fluxes are possible during all types of high wind events, and remove energy from the ocean. Open-ocean convection, or sinking of surface ocean water, is a localized process and only occurs in a few locations worldwide where there is cyclonic ocean circulation [*Clarke and Gascard*, 1983; *Gascard and Clarke*, 1983; *Killworth*, 1983]. Cyclonic circulation preconditions the ocean by driving the thermocline toward the surface thereby weakening vertical stability [*Killworth*, 1983; *Marshall and Schott*, 1999]. Subsequent heat loss or increase in salinity causes the surface waters to become denser and less buoyant, which erodes the stratification and allows for ocean convection [*Bacon et al.*, 2003; *Pickart et al.*, 2003b]. The Labrador Sea has cyclonic circulation and is a well-known area of convection and deep-water formation [*Clarke and Gascard*, 1983; *Gascard and Clarke*, 1983; *Killworth*, 1983]. The Irminger Sea also has cyclonic circulation and convection here is being actively investigated [*Pickart et al.*, 2003a, 2003b; *Spall and Pickart*, 2003; *Våge et al.*, 2011b]. Therefore, it is important to understand short-lived mesoscale wind events that have the capacity to drive large air-sea energy exchanges and may be an important factor for preconditioning the ocean and triggering convection in both the Irminger and Labrador Seas [*Pickart et al.*, 2003a, 2003b; *Spall and Pickart*, 2003; *Martin and Moore*, 2007; *Våge et al.*, 2008b, 2011b].

An aircraft campaign observed ocean swells as high as 3 – 9 m, strong white caps, and significant amounts of sea spray during these events [*Renfrew et al.*, 2009b], all of which make observations difficult yet indicate that there are strong atmosphere-ocean interactions occurring. Few in situ observations of these high wind events have been made due to complications due to the rugged terrain, intense weather, and remoteness. In this region surface buoys have been blown off their moorings within a few months [*Moore et al.*, 2008], coastal weather stations do

not reflect the flow over the ocean [*Pickart et al.*, 2003b], and ocean-based observations are difficult due to large waves driven by the strong near-surface winds. As a result of a dearth of observations, modeling studies are an important tool for understanding the physical process and connections between mesoscale winds and the ocean circulation. The focus of this dissertation is to answer the question: How do modeled mesoscale wind events around southeastern Greenland impact air-sea interactions and how does the ocean respond to this forcing?

Many ice-ocean models use global or reanalysis atmospheric data with low spatial and temporal resolution [*Hunke and Holland*, 2007; *Lisæter et al.*, 2007; *Kwok et al.*, 2008; *Hunke*, 2010], but low-resolution atmospheric models do not realistically represent mesoscale winds around Greenland [*Kolstad*, 2008; *Haine et al.*, 2009; *Sproson et al.*, 2010; *Shkolnik and Efimov*, 2013; *Tilinina et al.*, 2014]. Chapter 2 of this dissertation investigates how atmospheric models with resolutions of 10 – 150 km vary in their representation of an easterly tip jet and barrier wind event observed during the Greenland Flow Distortion Experiment (GFDex) in 2007 [*Renfrew et al.*, 2008]. By comparing high-resolution regional atmospheric model output from the Weather and Forecasting model (WRF) [*Skamarock et al.*, 2008] and the ECMWF Interim Reanalysis (ERA-I; [*Dee et al.*, 2011]) with in-situ dropsonde observations and QuikSCAT satellite observations [*Dunbar and Perry*, 2001; *Sampe and Xie*, 2007] of near surface wind it was determined that the highest resolution WRF model (10 km) replicated the structure of mesoscale winds the most realistically and that resolutions less than 50 km were unable to reasonably replicate the details of observed mesoscale winds. Additionally, by comparing turbulent flux observations from GFDex with the WRF model output it was determined that model resolution plays an important role in the flux magnitude and that high-resolution atmospheric models best capture the atmospheric state associated with the strong fluxes that occur during mesoscale

winds. Chapter 2 of this dissertation was published in *Monthly Weather Review* in an article titled "Evaluation of WRF Model Resolution on Simulated Mesoscale Winds and Surface Fluxes near Greenland" [*DuVivier and Cassano*, 2013]. Compared to observations, an atmospheric model resolution of 50 km was sufficient to capture mesoscale wind events, though the higher resolution 10 km simulations matched observations best.

The ice-ocean component of the Arctic climate system has a long memory and therefore models of the ice-ocean system require multidecadal atmospheric fording datasets. The analysis of how the winds and turbulent fluxes differ over 10 winters from two datasets – WRF at 50 km and ERA-I – is presented in Chapters 3 and 4. Using a 50 km WRF simulation sufficiently captures mesoscale winds and is computationally practical for the large domain and multidecadal forcing required by an ice-ocean model. The self-organizing map (SOM) algorithm [*Kohonen*, 2001] was used with winds around southeastern Greenland from both datasets. Chapter 3, titled "Comparison of wintertime mesoscale winds over the ocean around southeastern Greenland in WRF and ERA-Interim," details the range of wind patterns that occur in this region and explores the reasons for differences in the mean wind fields between both datasets. Understanding how the frequency with which particular patterns occur in each dataset and how the datasets simulate particular patterns differently is important to untangle how model resolution impacts wind representation for many samples of wind events. This work has been submitted to *Climate Dynamics* and is currently under review [*DuVivier and Cassano*, 2015]. In Chapter 4, "Exploration of turbulent heat fluxes and wind stress curl in WRF and ERA-Interim during wintertime mesoscale wind events around southeastern Greenland," the near-surface atmospheric state from each dataset is examined and the resulting air-sea turbulent heat fluxes and momentum flux, calculated with the COARE bulk flux algorithm [*Fairall et al.*, 2003], are compared.

Differences in the turbulent fluxes depend on differences in wind, temperature, and moisture, so these variables are explored for the wintertime mean state and for each SOM pattern. Additionally, the SOM patterns are evaluated for which have the largest turbulent fluxes and are therefore most likely to impact the ocean. This study is currently in review at *Journal of Geophysical Research- Atmospheres* [*DuVivier and Cassano*, 2014].

In the existing scientific literature, ocean model studies of convection in the seas around Greenland indicate that accurate representation of mesoscale events is necessary to simulate ocean convection, yet these studies have used simplified models [*Pickart et al.*, 2003a, p.200; *Våge et al.*, 2008b] or have been of short duration and limited in geographical domain [*Haine et al.*, 2009]. Explicitly representing mesoscale winds is required for realistic depiction of the physical processes and air-sea interactions occurring during a strong wind event, and this requires high-resolution regional atmospheric models. Therefore, we have used the high-resolution fully coupled Regional Arctic System Model (RASM) to investigate how explicitly represented strong wind events impact the ocean when both the atmosphere and ocean components of the climate system evolve together in a dynamically consistent manner. This analysis is presented in Chapter 5, titled "Atmospheric forcing and oceanic response during strong wind events around southeastern Greenland as modeled over 20 winters in the Regional Arctic System Model (RASM)." The SOM algorithm was used with 20 winters of near-surface atmospheric winds to identify the main wind patterns present around southeastern Greenland. The oceanic buoyancy loss due to thermal and haline components of the atmospheric forcing was then calculated for each of these wind patterns. The change in ocean mixed layer depth for each pattern was examined to determine which wind events impact the ocean most and where that impact occurs. This work is in preparation for submission to *Journal of Climate*.

Chapter 2: Evaluation of WRF model resolution on simulated mesoscale winds and surface fluxes near Greenland

This article appears in the March 2013 issue of Monthly Weather Review, Volume 141, Number 3 published by American Meteorological Society and available online through AMS Journals.
http://dx.doi.org/10.1175/MWR-D-12-00091.1

Abstract: Southern Greenland has short-lived but frequently occurring strong mesoscale barrier winds and tip jets that form when synoptic scale atmospheric features interact with the topography of Greenland. The influence of these mesoscale atmospheric events on the ocean, particularly deep ocean convection, is not yet well understood. Because obtaining observations is

difficult in this region, model simulations are essential for understanding the interaction between the atmosphere and ocean during these wind events. This paper presents results from Weather Research and Forecasting (WRF) model simulations run at four different resolutions (100 km, 50 km, 25 km, 10 km) and forced with the ECMWF ERA-Interim reanalysis product. Case study comparisons between WRF output at different resolutions, observations from the Greenland Flow Distortion Experiment (GFDex), which provides valuable in-situ observations of mesoscale winds, and QuikSCAT satellite data highlight the importance of high-resolution simulations for properly capturing the structure and high wind speeds associated with mesoscale wind events and surface fluxes of latent and sensible heat. In addition, the longer-term impact of mesoscale winds on the ocean is investigated by comparison of surface fluxes and winds between model resolutions over a two-month period.

1. Introduction

Greenland's southeastern coast is one of the windiest locations in the world [*Sampe and Xie*, 2007] because of frequent barrier winds and tips jets that form when synoptic flow interacts with and is deflected by Greenland's terrain [*Renfrew et al.*, 2008]. These powerful winds occur over the ocean in a region important to the downwelling component of the ocean's meridional overturning circulation (MOC). In the seas around Greenland (Figure 2), including the Irminger Sea, transfer of heat from warm North Atlantic surface waters to the atmosphere causes ocean water to sink as part of the MOC, an important component of the global heat budget [*Bacon et al.*, 2003; *Pickart et al.*, 2003a; *Sproson et al.*, 2008; *Petersen and Renfrew*, 2009; *Våge et al.*, 2011b]. Strong winds affect the ocean surface by inducing large sensible and latent heat fluxes from the ocean to the atmosphere, which decreases ocean water buoyancy and, in the right conditions, can lead to oceanic convection on horizontal scales of 1-10 km [*Gascard and Clarke*,

1983; *Lavender et al.*, 2002; *Pickart et al.*, 2003b; *Spall and Pickart*, 2003; *Martin and Moore*, 2007].

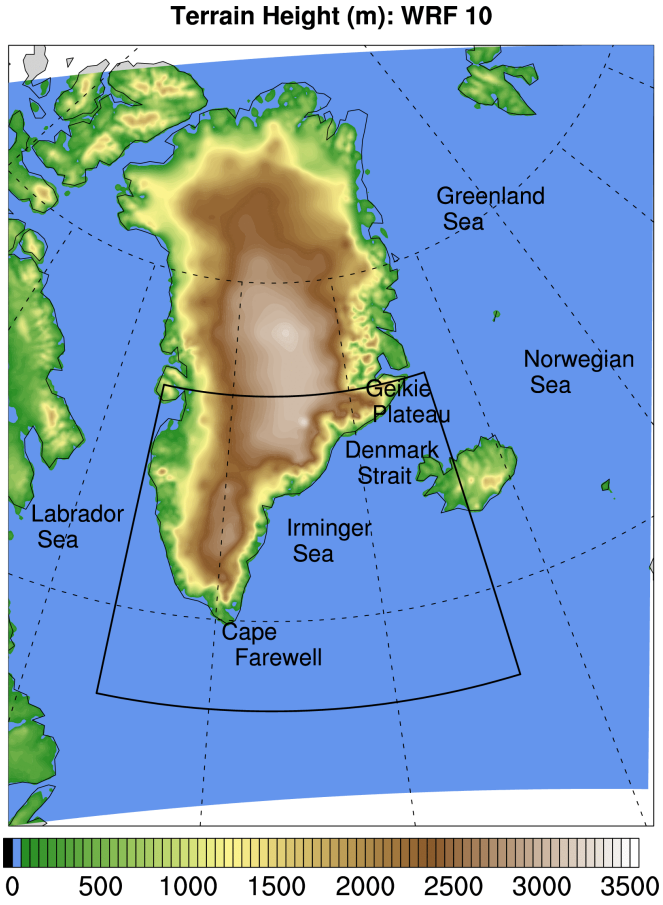

Figure 2: Map of WRF domain showing the terrain height (m) from the WRF10 simulation.

Understanding the detailed connection between short-lived winds and the longer term MOC is difficult due to the dearth of in-situ atmosphere and ocean observations, and because atmospheric reanalysis and large-scale global climate models do not resolve mesoscale winds well [*Kolstad*, 2008; *Sproson et al.*, 2010]. Previous studies have shown that an ocean model driven by large-scale atmospheric model or reanalysis data does not properly represent the ocean mixed layer depth and upper ocean currents, and that mesoscale atmospheric features, like high-speed tip jets, are important for accurately simulating these ocean features [*Våge et al.*, 2008b;

Haine et al., 2009]. However, because open-ocean convection occurs at so few sites globally, the connection between these winds and the ocean is an important topic of study because of the potential implications for global climate [*Bacon et al.*, 2003; *Petersen and Renfrew*, 2009]. Ideally, future model simulations with a high-resolution fully coupled atmosphere and ocean would better elucidate the importance of these high-speed mesoscale winds on the MOC.

The three types of high wind speed events that occur near the southeast coast of Greenland are barrier winds (BW), westerly ("forward") tip jets (WTJ), and easterly ("reverse") tip jets (ETJ) [*Moore*, 2003]. Climatologies of BW and tip jets show that these mesoscale wind events often have surface winds in excess of 25 m s^{-1} and occur frequently during the Northern Hemisphere winter months as synoptic flow from passing cyclones interacts with the high topography of Greenland [*Moore and Renfrew*, 2005; *Våge et al.*, 2009; *Harden et al.*, 2011]. BW form when low-level winds run into Greenland's east coast where steep terrain (Figure 2) can block the air from flowing over the topography. This blocked air converges along the coast, causing a localized high-pressure region [*Doyle and Shapiro*, 1999; *Moore and Renfrew*, 2005]. The resulting flow is northerly barrier-parallel winds that are accelerated by the component of the pressure gradient along the jet [*Outten et al.*, 2009; *Ólafsson and Ágústsson*, 2009].

Tip jets occur over the oceans near Cape Farewell, Greenland, and the location of the cyclone center is a main determinant for which type of tip jet occurs [*Moore*, 2003]. An ETJ forms when a cyclone is located south of Cape Farwell, so when barrier flow reaches Cape Farewell the local high pressure decreases and the pressure gradient aligns with the wind direction causing the air to accelerate [*Moore and Renfrew*, 2005; *Outten et al.*, 2009]. A WTJ occurs when a cyclone center is located between Iceland and Greenland, and air accelerates as it travels around Cape Farwell [*Doyle and Shapiro*, 1999; *Moore and Renfrew*, 2005; *Våge et al.*,

2009]. While these wind events have similarities, they can have differing effects on the ocean due to differences between wind stress curl of the jet, location of maximum winds, and near surface temperatures [*Spall and Pickart*, 2003; *Moore and Renfrew*, 2005; *Pickart et al.*, 2008; *Sproson et al.*, 2008; *Våge et al.*, 2009; *Harden et al.*, 2011].

Determining the impact of these mesoscale wind events on the ocean is important, yet there are still few in-situ observations of BW and tip jets. In summer 2004, a surface buoy was sited to measure high-speed winds over the ocean, but it was blown off its mooring before winter when the strongest mesoscale winds occur [*Moore et al.*, 2008]. No further standard surface observations are available over the ocean in this region, and land surface stations do not capture mesoscale flows above the ocean [*Pickart et al.*, 2003b]. Strong winds make scientific ocean cruises difficult and dangerous, and the authors know of only one aircraft campaign studying these mesoscale flows in the region [*Renfrew et al.*, 2008]. As a result of a dearth of observations, modeling studies are an important tool for understanding the connection between the ocean and mesoscale winds.

Many studies have been conducted to understand flow in complex terrain. These studies have demonstrated that high-resolution numerical models are important for capturing topographic effects such as low level gravity wave breaking and associated turbulence around Greenland, Iceland, and Norway [*Barstad and Grønås*, 2005; *Ágústsson and Ólafsson*, 2007; *Ólafsson and Ágústsson*, 2009], increased surface pressure drag by mountains [*Smith et al.*, 2006], and small scale variability in surface fluxes and wind speeds in Spitsbergen [*Kilpeläinen et al.*, 2011; *Reeve and Kolstad*, 2011]. These studies all use horizontal resolutions between 1 and 10 km and clearly demonstrate the importance of high-resolution for accurately modeling wind in complex terrain that can be important for forecasting.

However, to better understand the detailed coupling between the ocean and atmosphere during strong winds it is important to force the ocean with realistic winds, yet no large-scale data set at sub 10 km resolution for forcing ocean models exists to the authors' knowledge. Indeed, because of data constraints with large datasets of high-resolution data, many ocean models still use coarse reanalysis or global atmospheric model data for forcing [*Hunke and Holland*, 2007; *Lisæter et al.*, 2007; *Kwok et al.*, 2008; *Hunke*, 2010]. Previous work has created methods to parameterize mesoscale winds for ocean models driven by reanalysis [*Sproson et al.*, 2010], yet to tease out details in the atmosphere-ocean exchanges, explicit representation of mesoscale winds is ideal. In addition, many tip jet and barrier wind climatologies have used relatively low-resolution reanalysis data from NCEP [*Moore*, 2003; *Reeve and Kolstad*, 2011], ERA-Interim [*Harden et al.*, 2011], or ERA-40 [*Våge et al.*, 2009]. QuikSCAT scatterometer climatologies [*Moore and Renfrew*, 2005; *Kolstad*, 2008; *Reeve and Kolstad*, 2011] are problematic in the Arctic where sea ice concentration impacts data availability, and some wind events may not be captured in the satellite data. As such, using high-resolution models might provide a more accurate climatology of high wind events throughout the Arctic, and this paper will address model resolutions between current global model scales (~100km) and very high-resolution studies (~10km) to better understand what resolution is necessary to capture mesoscale wind events but is also data efficient enough to be used for forcing ocean models or creating multi-decadal climatologies of mesoscale winds.

This paper will use several case studies to compare simulations from the Weather Research and Forecasting (WRF) model during an ETJ and several BW events with observational data from an aircraft campaign and with QuikSCAT surface wind satellite data. These case study comparisons emphasize the importance of high-resolution numerical

simulations for accurately representing the horizontal and vertical wind structure and maximum speeds of mesoscale winds. Section 2 describes the numerical modeling methods and observational data used in the analysis. Section 3 illustrates the results from case study comparisons of mesoscale ETJ and BW events between WRF and the satellite and aircraft observations. Section 4 presents a two-month simulation comparison between WRF and QuikSCAT winds as well as longer-term differences between WRF at different resolutions. Finally, Section 5 offers conclusions and directions for future study.

2. Data and Methods

a. WRF Model Simulations

The WRF model is a regional mesoscale atmospheric model developed for research and forecasting applications [*Skamarock et al.*, 2008]. The WRF model has an effective resolution of $7\Delta x$, where Δx is the model's horizontal grid spacing [*Skamarock*, 2004]. The focus of this study is to determine what atmospheric resolution best captures mesoscale wind features by running the Advanced Research WRF (ARW) V3.2.1 model at four different horizontal grid increments: 10 km, 25 km, 50 km, and 100 km (respectively: WRF10, WRF25, WRF50, WRF100). The 10 km lower limit was chosen because high-resolution features are known to be important for forcing the ocean, but atmospheric resolutions greater than 10 km are still too computationally expensive for multi-decadal fully coupled model simulations that would more fully explore the connection between atmosphere and ocean during these events. The 100 km grid increment provides a baseline for WRF performance at the scale of global models or reanalyses. We have not included WRF100 figures in the remaining analysis because WRF's effective resolution suggests that tip jets, which have a scale of a few hundred kilometers, would need to be modeled with no less than 50 km horizontal grid increment, so we have focused our discussion on the

WRF10, WRF25 and WRF50 simulations. Inland, the maximum terrain heights were generally higher for high-resolution simulations in southern Greenland with WRF10 having a maximum terrain height of about 3260 m (WRF50: 3100 m) near the Geikie Plateau and 2785 m (WRF50: 2761 m) near Cape Farewell. Along the coasts, the slope is steeper in the 10 km model configuration than in the 50 km configuration; near the Geikie Plateau the slope for WRF10 was about 1.5 times greater than for WRF50, and near Cape Farewell the WRF10 slope was 1.6 times greater than for WRF50.

The domain for all WRF simulations is shown in Figure 2, and all WRF simulations had a 10 hPa model top and 40 vertical levels, about 10 of which are in the lowest 1 km of the atmosphere. The ERA-Interim reanalysis (see section 2.b) was used to specify the WRF lateral boundaries every 6 hours. Sea ice was specified from the NSIDC Bootstrap Sea Ice Concentration satellite product, which has a 0.25° x 0.25° resolution and provides sea ice fraction as a WRF lower boundary condition [*Comiso*, 2008]. For grid cells that contain sea ice WRF calculates surface variables over the open ocean and sea ice portion of the grid cell separately and then calculates an area-weighted average over the entire grid cell [*Bromwich et al.*, 2009]. We used WRF physics options (Table 1) found to maximize performance in a pan-Arctic domain [*Cassano et al.*, 2011]. For the case studies presented here, WRF was initialized two days before the date of aircraft or satellite observations (Table 2), and the model provided hourly output. Additionally, we performed continuous 1 February – 31 March 2007 simulations on the same domain for each WRF resolution to evaluate longer-term atmospheric differences due to resolution; these were initialized on 1 February and then run only with lateral boundary forcing until 31 March. No nesting was used in any WRF simulation, and the box in Figure 2 shows the area of particular interest for this study.

Planetary Boundary Layer	Mellor-Yamada-Janjic TKE
Surface Layer	Monin-Obukhov (Janjic Eta)
Radiation	rrtmg (both sw and lw)
Microphysics	Goddard GCE
Cumulus	Grell-Devenyi
Land Surface	Noah LSM

Table 1: WRF Physics Options [*Cassano et al.*, 2011]

Day	Wind Feature	GFDex Flight #	GFDex dropsondes	GFDex surface obs.	QuikSCAT satellite obs.
21 FEB	Easterly Tip Jet	B268	14 UTC		7UTC, 22UTC
02MAR	Barrier Wind	B274	12 UTC	14 UTC	7UTC, 22UTC
05MAR	Barrier Wind	B276		14 UTC	7UTC, 22UTC
06MAR	Barrier Wind	B277	15 UTC	11 UTC	7UTC, 22UTC
09MAR	Barrier Wind	B278		12 UTC	7UTC, 22UTC

Table 2: Observation Data Availability

We calculated the relative vorticity from QuikSCAT observations and wind stress curl from WRF 10 m winds to better understand how the different resolutions were able to capture the narrow jet features. Wind stress curl, like relative vorticity, is a measure of the change in horizontal wind speed over a horizontal distance and large values of wind stress curl or relative vorticity indicate strong horizontal wind shear. Furthermore, positive wind stress curl drives ocean upwelling from Ekman pumping and could lead to preconditioning of the water column for convection. In addition, to understand the forcing and dynamical differences between the different resolution simulations, we calculated the pressure gradient (PG), Coriolis, advection, and acceleration terms of the horizontal momentum equations [*Holton*, 2004] with remaining terms determined as a residual following the procedure of Nigro et al. [2012]. Grid points with terrain above 100 m were excluded because of errors associated with calculating derivatives over the terrain along Greenland's southeast coast, and the time derivative in the acceleration term

was calculated using a forward finite difference with model output from 0 and +1 hours relative to the time of interest.

Over the ocean, the surface layer physics scheme calculates sensible and latent heat fluxes (each with units of W m^{-2}) that describe energy exchange between the surface and the atmosphere [*Skamarock et al.*, 2008]. The sensible heat flux is given by

$$SH = \rho C_p u_* \theta_* \tag{1}$$

where ρ is air density, C_p is a dimensionless transfer coefficient, u_* is the friction velocity, and θ_* is a temperature gradient term. The friction velocity is given by

$$u_* = \frac{kV_\nu}{\ln\left(\frac{z_\nu}{z_0}\right) - \Psi} \tag{2}$$

where V_ν is the wind speed at the lowest model level, z_ν is the height of the lowest eta level, z_0 is the momentum roughness length, and Ψ is a stability function. The temperature gradient term is given by

$$\theta_* = \frac{k\Delta\theta}{\ln\left(\frac{z_\nu}{z_{0h}}\right) - \Psi} \tag{3}$$

where z_ν and Ψ are the same as in Equation 2, $\Delta\theta$ is the temperature difference between the surface and lowest model level, and z_{0h} is the heat roughness length (Dudhia 2010). Similarly, the latent heat flux is given by

$$LH = \rho L_e u_* q_* \tag{4}$$

ρ and u_* are the same as in Equation 1, L_e is the latent heat of vaporization of water, and q_* is a moisture gradient term given by

$$q_* = \frac{k\Delta q}{\ln\left(\frac{z_0}{z_{0q}}\right) - \Psi} \tag{5}$$

where z_n and Ψ are the same as in Equation 2, Δq is the temperature difference between the surface and lowest model level, and z_{0q} is the moisture roughness length (Dudhia 2010). However, the MYJ parameterization uses a single value for the momentum, heat, and moisture roughness lengths. Most bulk aerodynamic formulae have a form similar to Equations 1 and 4, and differ in the way that they calculate Ψ or other transfer coefficients.

b. ERA-Interim Reanalysis

In addition to being used as the WRF initial and lateral boundary conditions the European Centre for Medium-Range Weather Forecasts (ECMWF) Interim reanalysis (ERA-Interim or ERA-I) data were also compared with WRF simulations. When compared to the previous generation reanalysis ERA-40, the ERA-I data have a longer time range, more vertical levels, a higher resolution (~79 km), assimilated scatterometer winds (including QuikSCAT), and different physics parameterizations [*Dee et al.*, 2011]. The ERA-I data used in this study was gridded to a 1.5° x 1.5° resolution, 37 vertical pressure levels, about 6 of which are in the lowest 1 km of the atmosphere, and a 0.1 hPa model top (ECMWF). Data are available in 6-hourly increments (00UTC, 6UTC, 12UTC, 18UTC), and the nearest ERA-I output time was chosen to compare with observations and WRF. However, surface flux data are only available every 12 hours (00UTC and 12UTC), and these data were not used because these times often differed by more than two hours from observations.

c. QuikSCAT Satellite

The QuikSCAT satellite provides high-resolution surface wind data over the global oceans during two passes each day with an 1800 km wide swath [*Dunbar and Perry*, 2001; *Sampe and Xie*, 2007] from 1999 to 2009, when the scatterometer failed [*Dee et al.*, 2011]. Microwave radiation emitted from the satellite is backscattered off the ocean surface, and wind stress and wind vectors can be calculated based on the surface roughness. However, QuikSCAT is unable to provide observations in locations with heavy rainfall or over land, sea ice, or in the marginal ice zone because they do not have wind-altered surface roughness, so these areas are masked in the QuikSCAT product. Nevertheless, QuikSCAT is a valuable resource for verifying the spatial details of the simulated wind field. Table 2 lists the average time of the QuikSCAT passes used for comparison to WRF and ERA-I.

Two retrieval algorithms, NASA-DIRTH and RSS, are available for surface wind speed. Previous studies comparing aircraft and buoy observations with the QuikSCAT products found that both algorithms appear to have positive wind speed biases [*Moore et al.*, 2008; *Renfrew et al.*, 2009a, 2009b]. Over all types of observations, the NASA-DIRTH bias ranged from +1.9 to 2.6 m s^{-1}, and this algorithm had a more conservative sea ice mask than RSS. The RSS bias was +2.3 to 3.3 m s^{-1}, and this algorithm particularly overestimated speeds in high wind speed conditions. This study uses NASA Jet Propulsion Laboratory's Level 3 daily ocean wind vector data that has been gridded to 0.25° (~25 km) spacing and derived with the NASA-DIRTH algorithm [*Dunbar and Perry*, 2001]. These data have been flagged for land, sea ice, and heavy rain, so data gathered in these locations is flagged as missing in the dataset and the remaining data are quality controlled and located over the open ocean [*Dunbar and Perry*, 2001].

We calculated the relative vorticity of the QuikSCAT 10 m winds to evaluate the wind speed gradients associated with ETJ and BW and for comparison with the WRF wind stress curl. We linearly interpolated the missing wind values over open-ocean before calculating the relative vorticity. We did not calculate wind stress curl for QuikSCAT because wind stress curl requires use of the drag coefficient. In the following discussion we have compared the QuikSCAT relative vorticity with the WRF wind stress curl. While these two variables are not the same, they are both strongly influenced by horizontal wind gradients and comparing the horizontal scale of QuikSCAT vorticity with WRF wind stress curl gives an indication of the spatial scale of the horizontal wind shear features in the mesoscale winds of interest for this study.

d. Greenland Flow Distortion Experiment

The Greenland Flow distortion Experiment (GFDex) was the first aircraft campaign to obtain observations of an ETJ and BW near the southeast Greenland coast [*Renfrew et al.*, 2008]. GFDex flew a total of 12 missions between 21 February and 10 March 2007, and of these missions, one observed an ETJ while four others observed BW (Table 2). We use GFDex dropsonde measurements, which provide vertical information about winds, moisture content, and equivalent potential temperature, and observations of near-surface variables and fluxes [*Petersen and Renfrew*, 2009; *Petersen et al.*, 2009; *Renfrew et al.*, 2009a, 2009b]. These observations are important not only because they provide the first in-situ data of these mesoscale wind events, but also because they provide variables besides wind speed that are important for ocean-atmosphere interaction. Complete flight paths and observations can be found in Renfrew et al. [2009a] and Petersen et al. [2009], but the dropsonde flight legs used for comparison with WRF in this paper are shown on Figure 3.

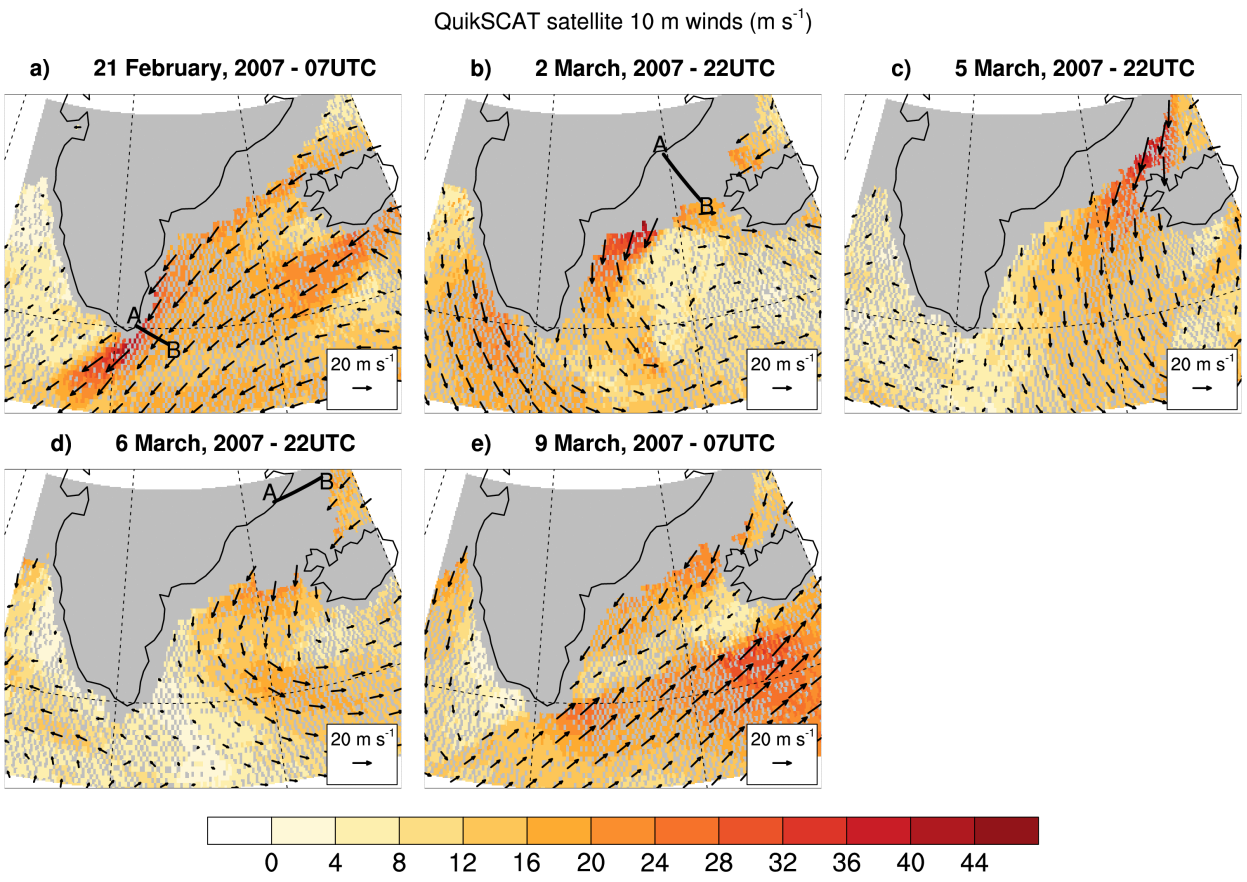

Figure 3: QuikSCAT satellite wind observations for each of the GFDex case study days. An Easterly Tip Jet was observed 21 February (a), and barrier winds were observed 2 March (b), 5 March (c), 6 March (d), and 9 March (e). Black lines on the figures for 21 February, 2 March, and 6 March mark the locations of GFDex dropsonde flight legs.

The aircraft and dropsonde observations of jet vertical structure as well as fluxes provide some of the only in-situ data for these high-wind events, and these data will be a basis for comparison in the rest of this paper. Vertical cross sections, interpolated from dropsonde observations [*Petersen et al.*, 2009; *Renfrew et al.*, 2009b], are compared with the simulated vertical structure in WRF. GFDex near-surface observations were taken at an average flight altitude of 39 m above sea level with a total range of 32-51 m. Surface temperature values are derived from a downward-looking Heimann radiometer, while the surface mixing ratio, 2 m mixing ratio, 2 m temperature, and 10 m winds were interpolated from flight altitude using the

COARE 3.0 bulk flux algorithm [*Renfrew et al.*, 2009a]. Following GFDex convention, in-situ covariance measurements of turbulent fluxes were not compared with WRF model data due to large variability in the observed fluxes [*Petersen and Renfrew*, 2009; *Renfrew et al.*, 2009a]; instead, latent and sensible heat fluxes were calculated using both the COARE 3.0 [*Fairall et al.*, 2003] and Smith [*Smith*, 1988] bulk flux algorithms. Only the COARE value will be shown here since the fluxes calculated using each algorithm match well [*Renfrew et al.*, 2009a]. The COARE 3.0 algorithm has been adjusted for use in higher wind speed conditions and uses separate values for momentum, heat, and moisture roughness lengths [*Smith*, 1988; *Fairall et al.*, 2003].

To compare with aircraft observations, WRF output was interpolated to the flight latitudes and longitudes using a distance weighted average of the four WRF grid points closest to the flight path. For cross sections, the horizontally interpolated WRF output was linearly interpolated to regular vertical levels. Equivalent potential temperature for the WRF cross sections was calculated from the WRF temperature, humidity, and pressure. For flux comparisons, the surface variables, q_{2m}, T_{sfc}, T_{2m}, were direct model output; surface saturation mixing ratio, q_{sfc}, was calculated using the surface temperature and sea level pressure. For the four near-surface flights, an average root mean squared error (RMSE) and correlation were found between the near-surface variables for each WRF simulation and the GFDex observations to evaluate how well the WRF simulations captured the GFDex observations.

3. Case Studies

a. Overview of case studies

Detailed analysis of the synoptic situation of each of these case studies has been explored in detail in the literature. The following descriptions are meant to provide a brief description of

each case for this study, but more information can be found in Renfrew et al. [2008], Petersen et al. [2009], Petersen and Renfrew [2009], Renfrew et al. [2009a, 2009b], Outten et al. [2009].

GFDex observed one ETJ in February 2007 and BWs in the Denmark Strait during four days in March 2007. Figure 3 shows the QuikSCAT 10 m winds for each of the five days examined and provides a snapshot of the synoptic situation during the mesoscale wind event present at the particular time when QuikSCAT observations were available. On each of the BW days, the QuikSCAT sea ice mask obscures coastal regions with strong wind speeds, but on some of these days GFDex dropsonde observations over the marginal ice zone provide information about the jet in this region. Dropsonde flights that will be discussed in this paper are marked on Figure 3; 'A' marks the starting point (0 km) for cross-sections created from the dropsonde data. Additionally, on the BW days GFDex flights observed surface variables and fluxes.

On 21 February 2007 (Figure 3a) there was a strong, distinct ETJ present during the 07 UTC QuikSCAT satellite pass that extended from Cape Farewell over the southeast Labrador Sea. This ETJ was present, though weakening, during the 22 UTC pass (not shown). GFDex dropsonde observations were available at 15 UTC along the marked flight path near Cape Farewell, but in-situ surface data are not available.

On 2 March at 22 UTC there was a BW to the southwest of the Denmark Strait, along the Greenland Coast (Figure 3b). A strong BW in the Denmark Strait existed at 22 UTC on 5 March (Figure 3c) and at both 07 UTC (not shown) and 22 UTC on 6 March (Figure 3d). The 5 March QuikSCAT sea ice mask covers half of the Denmark Strait (Figure 3c), while the 6 March sea ice mask covers the entire Denmark Strait (Figure 3d), possibly from sea ice advection by the strong winds. By 9 March 07UTC (Figure 3e) the BW was weaker.

The following sections will discuss each flow regime – ETJ and BW – in more detail with particular emphasis on the low level winds, boundary layer structure, and surface fluxes because these are particularly important for understanding how the atmosphere and ocean interact. Exemplary comparisons have been chosen to highlight relevant differences for the case study days between the different resolution WRF simulations.

b. Easterly Tip Jet (ETJ) Regime

Comparison between QuikSCAT observed winds, ERA-I, and WRF reveal differences in maximum wind speeds and shape of the ETJ due to resolution. QuikSCAT observations (Figure 4a) show a sharp distinction between the windward east coast of Greenland with maximum ETJ speeds of 42 m s^{-1} over the ocean and the leeward west coast that has wind speeds below 10 m s^{-1}. The WRF10 (Figure 4b) and WRF25 (Figure 4c) simulations show a discrete ETJ that closely matches QuikSCAT observations in location, shape, and length, but WRF10 has 35 m s^{-1} maximum wind speeds, while WRF25 has 32 m s^{-1} maximum speed. As resolution decreases, the ETJ becomes less distinct and the maximum wind speeds over the ocean decrease, and there is a less distinct lee region on the west side of Greenland, particularly in WRF50 (Figure 4d), WRF100 (not shown), and ERA-I (not shown).

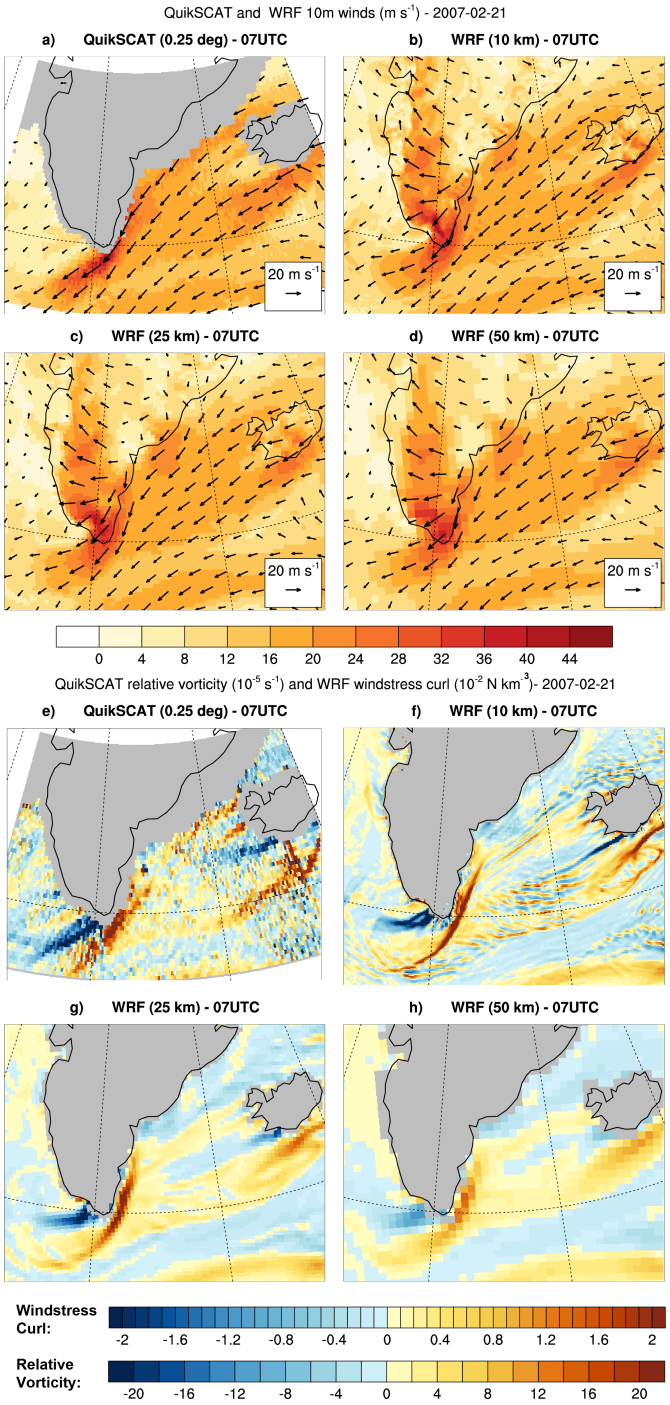

Figure 4: Easterly tip jet 10 m wind speed (m s^{-1}) on 21 February 2007 at 07UTC from the QuikSCAT satellite (a), WRF10 (b), WRF25 (c), WRF50 (d). The relative vorticity (10^{-5} s^{-1}) corresponding to the 10 m winds for the QuikSCAT satellite (e), and wind stress curl (10^{-2} N km^{-3}) for WRF10 (f), WRF25 (g), WRF50 (h). The QuikSCAT wind field (a) has been linearly interpolated to replace missing data and this interpolated field was used when calculating the QuikSCAT relative vorticity (e).

Using the half-width of the tip jet as defined from QuikSCAT, we found the wind speed gradient for each simulation starting at the maximum wind speed of each simulated jet. We found that the wind speed gradient in QuikSCAT was about 1.6 times greater than the gradients in WRF10 and WRF25, 1.7 times greater than the WRF50 gradient, 4 times greater than the WRF100 gradient, and 3.5 times greater than the ERA-I gradient. This means that the low-resolution ERA-I and WRF100 simulations were not able to capture the observed narrow, high-speed jet as well as the higher resolution WRF simulations. Additionally, the QuikSCAT relative vorticity (Figure 4e) shows the small spatial scale of strong wind shear around the ETJ. The wind stress curl for WRF10 (Figure 4f) and WRF25 (Figure 4g) have a similar spatial scale to the relative vorticity shown by QuikSCAT. In addition, the magnitude of wind stress curl in WRF10 and WRF25 had a more detailed structure and was about 2 times larger than WRF50 (Figure 4h) and 10 times larger than WRF100 (not shown). The high-resolution WRF simulations better capture the strong, narrow jet and the sharp wind speed drop from the center to the edge of the jet.

The sea level pressure field and calculated PG (not shown) during the ETJ illustrate the importance of correctly representing the terrain slope. Comparison between the WRF10 and WRF100 sea level pressure fields shows that the WRF10 pressure along the coast is higher when compared with WRF100, and the result is that the PG momentum term is larger and nearer the coast in WRF10 than WRF100. While the wind fields are similar between WRF10 and WRF25, the PG fields show that there is more detailed structure in the WRF10 field, particularly near terrain and in the lee of Iceland. Differences in terrain height between the WRF resolutions are most pronounced along the coast, and the lower resolution simulations lose the sharp elevation gradient near the coast necessary for proper flow blocking. WRF simulations run at 10 km but with 100 km terrain heights imposed (not shown) have reductions in ETJ wind speeds by 6-10 m

s^{-1} and reductions in both sensible and latent heat fluxes by 100-200 W m^{-2}. The simulations emphasize that having both high-resolution to adequately represent atmospheric processes and the correct terrain heights and slopes are important for simulating observed wind speeds. Without the necessary barrier the winds are effectively smeared over land and are not confined to the coast where the localized high-pressure causes the high-speed ETJ as seen in the QuikSCAT data.

Cross-sections of wind speed and equivalent potential temperature with height, from the GFDex dropsondes, show the vertical structure of the jet. The GFDex observed winds (Figure 5a) indicate that the jet core, with speeds of 48 m s^{-1}, is located approximately 800 m above sea level. With increasing distance from the coast the speed of the jet decreases, and aloft the jet core tilts slightly upward away from the coast. The WRF output shows distinct differences with the simulated jet between the different model resolutions used. The simulated winds from the WRF10 (Figure 5b), WRF25 (Figure 5c), and WRF50 (Figure 5d) simulations have jet cores near 800 m with 46 m s^{-1} maximum wind speed for WRF10 and WRF25 and 48 m s^{-1} for WRF50, while the WRF100 jet (not shown) has a higher core and lower core speeds. In addition, the WRF10, WRF25, and WRF50 simulations capture the shape, tilt, extent, and speeds of the jet core with distance from the coast shown from GFDex.

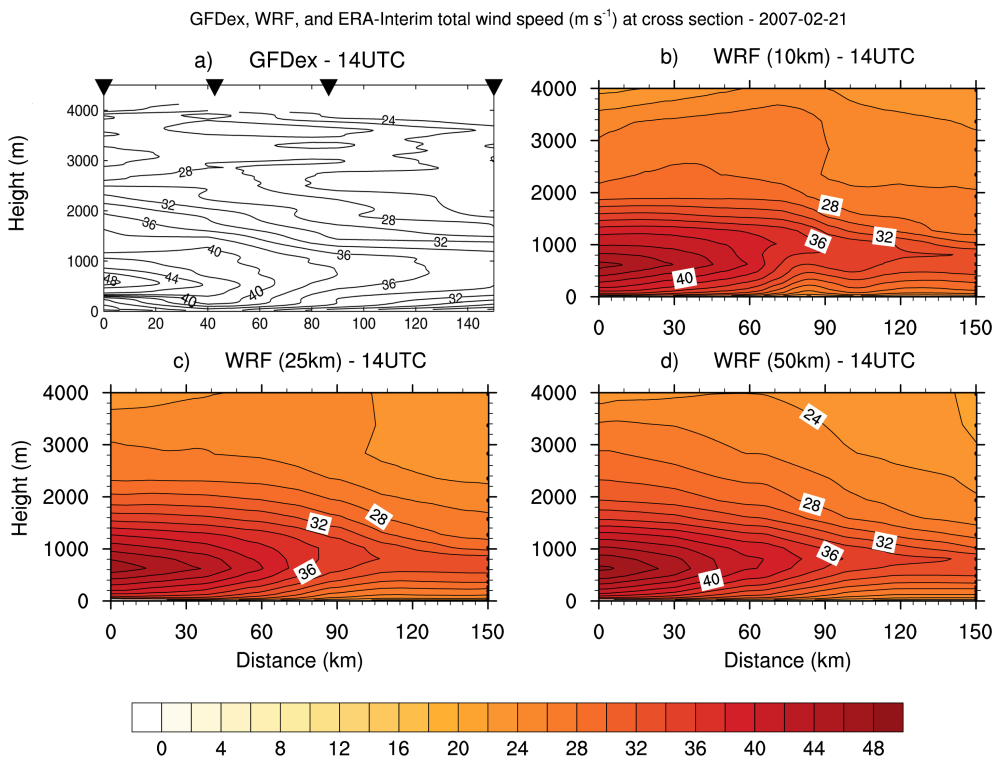

Figure 5: Cross section of total wind speed (m s^{-1}) from GFDex flight path on 21 February 2007 at 14UTC from the GFDex dropsonde observations (a), WRF10 (b), WRF25 (c), WRF50 (d). 'A' on Figure 3a marks 0 km on the cross section and 'B' marks 150 km on the cross section.

The GFDex equivalent potential temperature observations (Figure 6a) show an unstable surface layer, topped by an 800 m deep well-mixed boundary layer near the coast that increases in depth away from the coast. Additionally, above 800 m a strong vertical equivalent potential temperature gradient marks an inversion above the jet. WRF10 (Figure 6b), WRF25 (Figure 6c), and WRF50 (Figure 56d) all capture the unstable surface layer and boundary layer depth, but WRF10 best captures the strong inversion above 800 m as well as the horizontal equivalent potential temperature gradient. One key difference between GFDex and all WRF simulations is that WRF has a cold equivalent potential temperature bias ranging from 6 K (WRF10 and WRF25) to 4 K (WRF50). However, the physical structure of the boundary layer in the WRF simulations match observations, which implies that the simulations are correctly replicating the

fluxes and associated surface layer temperature gradients necessary to create the unstable surface layer and mixed layer depths in spite of the temperature bias.

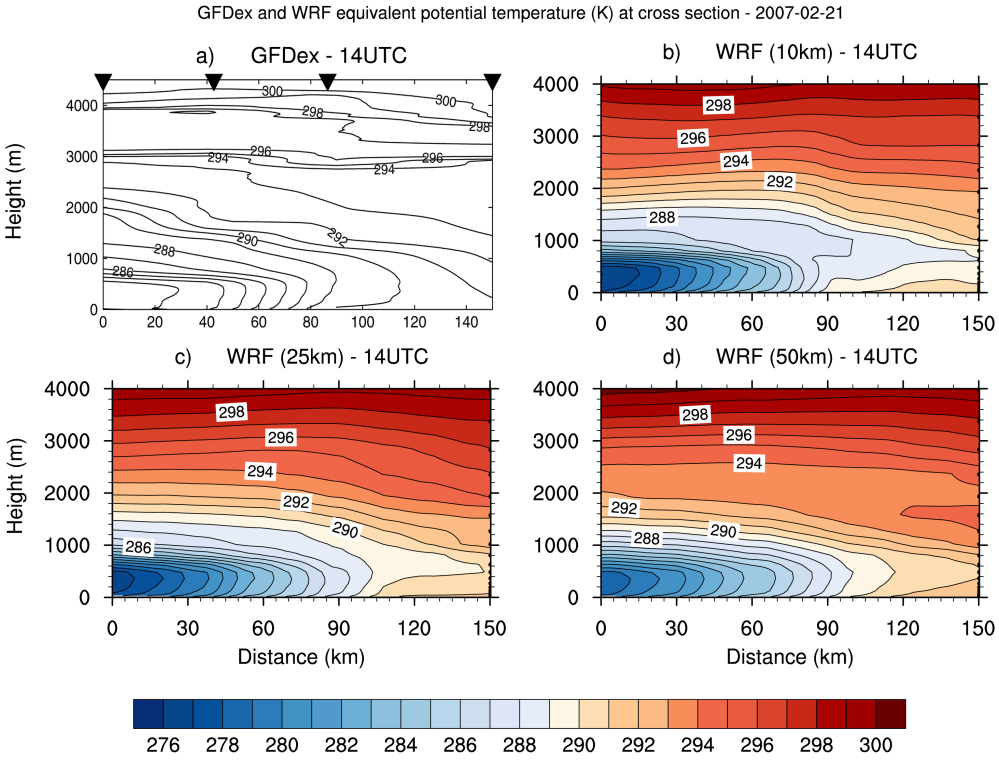

Figure 6: Cross section of equivalent potential temperature (K) from GFDex flight path on 21 February 2007 at 14UTC from the GFDex dropsonde observations (a), WRF10 (b), WRF25 (c), WRF50 (d). 'A' on Figure 3a marks 0 km on the cross section and 'B' marks 150 km on the cross section.

Comparisons between simulated surface sensible (Figure 7) and latent (not shown) heat fluxes reveal differences between resolutions in the vicinity of the ETJ. The WRF10 (Figure 6a) and WRF25 (Figure 7b) simulations' maximum surface sensible heat fluxes are both above 400 W m^{-2} and are directly co-located with the ETJ. In contrast, the WRF50 (Figure 7c) sensible heat fluxes do not exceed 200 in the ETJ region and the WRF100 fluxes are the same in the ETJ region as the surrounding Irminger Sea (not shown), which has strong implications for air-sea exchanges in the ETJ vicinity. In addition, the large fluxes occur where we find large positive

wind stress curl, and the resulting upwelling would shoal the thermocline and lead to a shallower surface layer that would need to lose less energy before ocean convection could take place. Similar differences in flux magnitude can be seen just south of Iceland where strong winds to the south of the island drive larger fluxes in higher resolution WRF simulations. The maximum fluxes for the high-resolution simulations are more physically plausible because bulk flux formulae show that the magnitude of both sensible and latent heat fluxes depends linearly on the low level wind speed. Thus, all other physical inputs being approximately equal (not shown, although verified), one would expect both latent and sensible fluxes to peak with highest surface winds. Thus, it seems reasonable that the large heat fluxes co-located with high-speed winds in the high-resolution simulations are more realistic, and over a long period of time the increased fluxes would have a greater impact on the ocean than the fluxes in the low-resolution simulations.

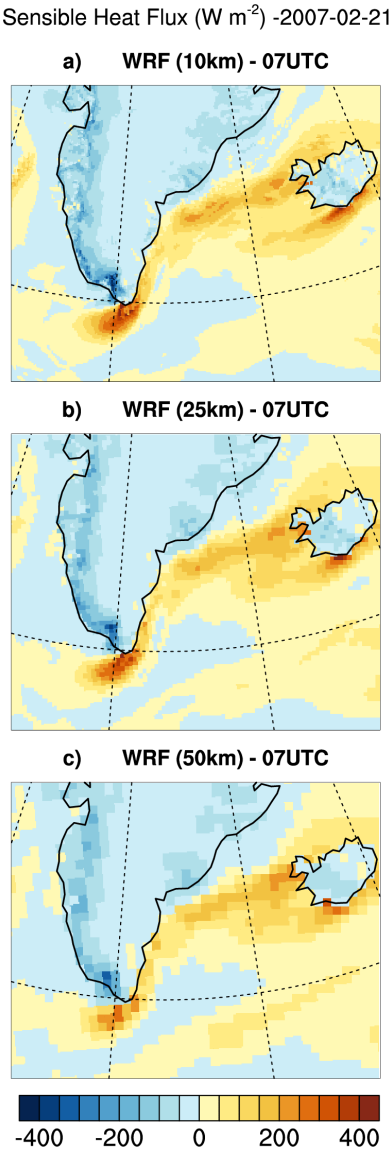

Figure 7: Surface sensible heat flux (W m^{-2} – positive upward) on 21 February 2007 at 07UTC from WRF10 (a), WRF25 (b), and WRF50 (c).

c. Barrier Wind (BW) Regime

On 5 March, at 22 UTC QuikSCAT observations identified an area with wind speeds greater than 44 m s^{-1} in the Denmark Strait north of Iceland (Figure 8a). WRF10 (Figure 8b) and WRF25 (Figure 8c) simulate peak BW speeds between 34-36 m s^{-1}, but the WRF50 (Figure 8d) and WRF100 (not shown) maximum wind speed is less than 33 m s^{-1} and the strong winds do not extend as far south as those in the high-resolution simulations. In WRF10, there is a wake region

south of the plateau that becomes less pronounced with decreasing resolution. The directions of the winds are also subtly different: WRF10 has an easterly component to the winds that is not as strong for WRF25, WRF50, or WRF100, implying that in WRF10 the air is being forced through the Denmark Strait instead of flowing over the Geikie Plateau (elevation ~2 km) to the north.

Like the ETJ case, the wind stress curl has a greater magnitude and more detailed structure in WRF10 (Figure 8f) than WRF25 (Figure 8g), WRF50 (Figure 8h), or WRF100 (not shown). The high-resolution WRF10 wind stress curl field has features that are similar in size to the QuikSCAT (Figure 8e) relative vorticity field. This reinforces that the wind gradients and jet locations are better simulated in high-resolution WRF. In addition, the WRF10 PG momentum term (not shown) has strong pressure gradients around the Geikie Plateau that would lead to strong winds, but the structure is less defined and the PG is weaker in the other WRF simulations. Thus, lower resolution WRF have less distinct and weaker BW because of flow over the Geikie Plateau instead of around the plateau due to blocking similar to the ETJ. While these spatial wind field features are not verifiable with QuikSCAT due to the sea ice mask, the physical explanation of reduced terrain blocking in low-resolution WRF makes sense and would result in weaker PG forces, weaker maximum winds, and an indistinct lee.

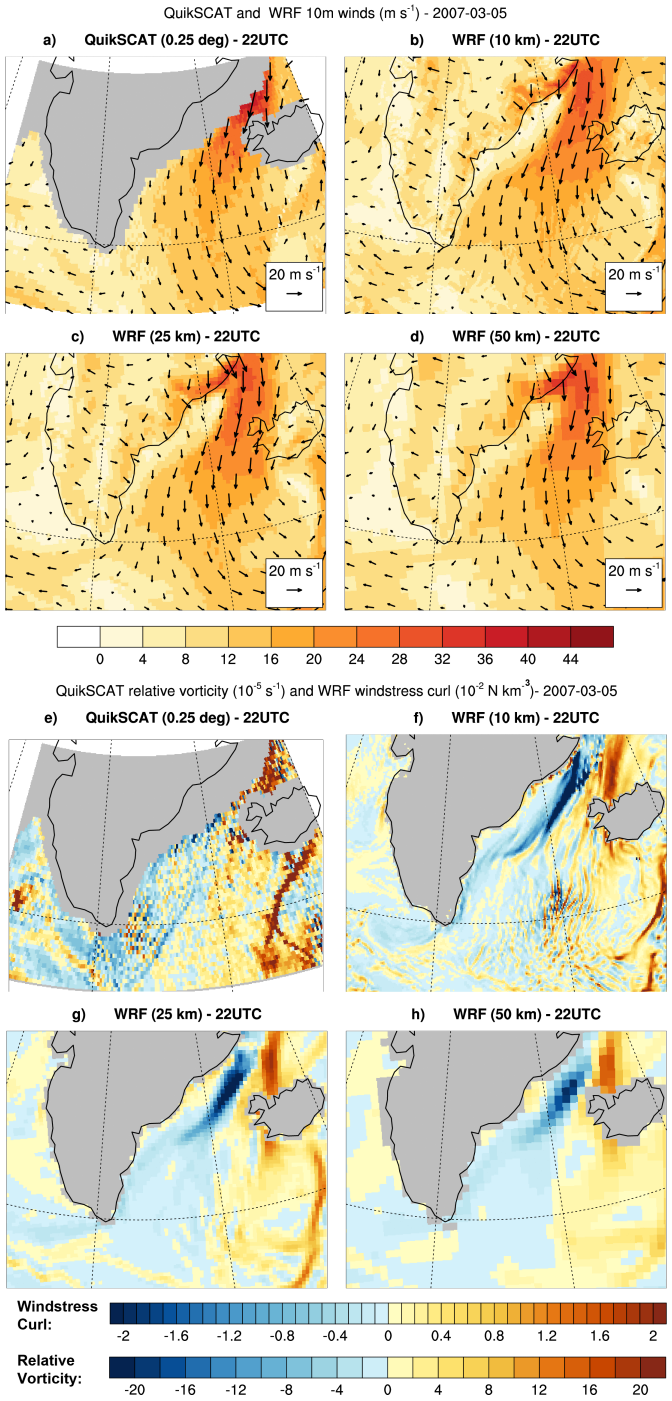

Figure 8: Barrier wind 10 m wind speed (m s^{-1}) on 5 March 2007 at 22UTC from the QuikSCAT satellite (a), WRF10 (b), WRF25 (c), WRF50 (d). The relative vorticity (10^{-5} s^{-1}) corresponding to the 10 m winds for the QuikSCAT satellite (e), and wind stress curl (10^{-2} N km^{-3}) for WRF10 (f), WRF25 (g), WRF50 (h). The QuikSCAT wind field (a) has been linearly interpolated to replace missing data and this interpolated field was used when calculating the QuikSCAT relative vorticity (e).

In addition to QuikSCAT observations, GFDex dropsonde observations help illustrate how the different resolutions simulate the BW. Comparison between GFDex observations and WRF output show that low-resolution WRF does not distinguish between barrier and downslope flow, two flow regimes forced by different dynamics. On 6 March, observations in the north Denmark Strait reveal a BW with maximum speeds of 35 m s^{-1} hugging the coast below 1000 m and a second jet over the land (Figure 9a). WRF10 (Figure 9b) simulates the primary jet core to be approximately the same height and distance off the coast as observations, though it has maximum wind speeds of 45 m s^{-1}. In WRF10, like in the observations, the secondary jet over land is distinct from the over-sea BW, but the other WRF simulations (Figures 9c and 9d) merge the two jets and have lower total wind speeds.

Breaking down the total wind into flow parallel and perpendicular to the cross section reveals that these two jets are different flow regimes that WRF is not able to separate in low-resolution simulations. The parallel component shows that WRF10 (Figure 9e) and WRF 25 (not shown) clearly have strong westerly downslope flow tied to Greenland's topography, but WRF50 (Figure 9f) shows weaker downslope flow. In WRF10 (Figure 9g) the BW dominates the southerly perpendicular flow over the ocean, while a smaller along slope jet is present along the Greenland terrain. WRF25 (not shown) and WRF50 (Figure 9h) combine the barrier and downslope flow perpendicular to the cross section into a weaker jet.

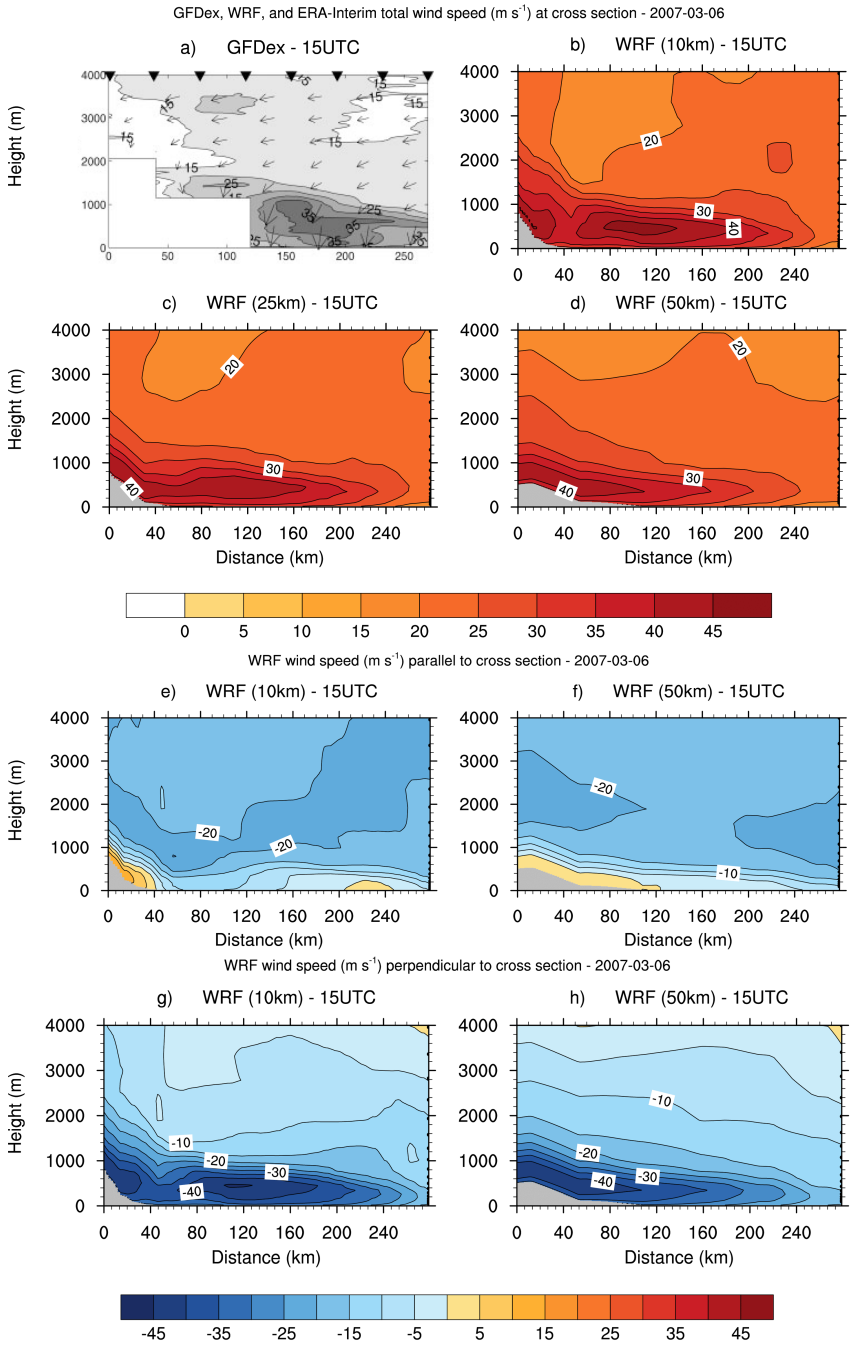

Figure 9: Cross section of wind speed (m s^{-1}) from GFDex flight path on 6 March 2007 at 15UTC. Total wind speed from GFDex dropsonde observations (a), WRF10 (b), WRF25 (c), WRF50 (d). Cross-section parallel flow for WRF10 (e) and WRF50 (f) and cross-section perpendicular flow for WRF10 (g) and WRF50 (h). For the cross-section parallel figures easterly winds are shown in blue and westerly winds in orange. For the cross-section perpendicular figures northerly winds are shown in blue and southerly winds in orange. 'A' on Figure 3d marks 0 km on the cross section and 'B' marks 280 km on the cross section.

The equivalent potential temperature cross sections in the BW regimes indicate that high-resolution WRF simulates more realistic boundary layer structure than low-resolution WRF. On 2 March, GFDex shows the deepest boundary layer depth as approximately 2 km over the sea, and the boundary layer height decreases toward the Greenland coast (Figure 10a). WRF10 (Figure 10b), WRF25 (Figure 10c), and WRF50 (Figure 10d) all capture the boundary layer depth along the cross section, but WRF10 best matches observed surface horizontal gradient of equivalent potential temperature and vertical equivalent potential temperature gradient.

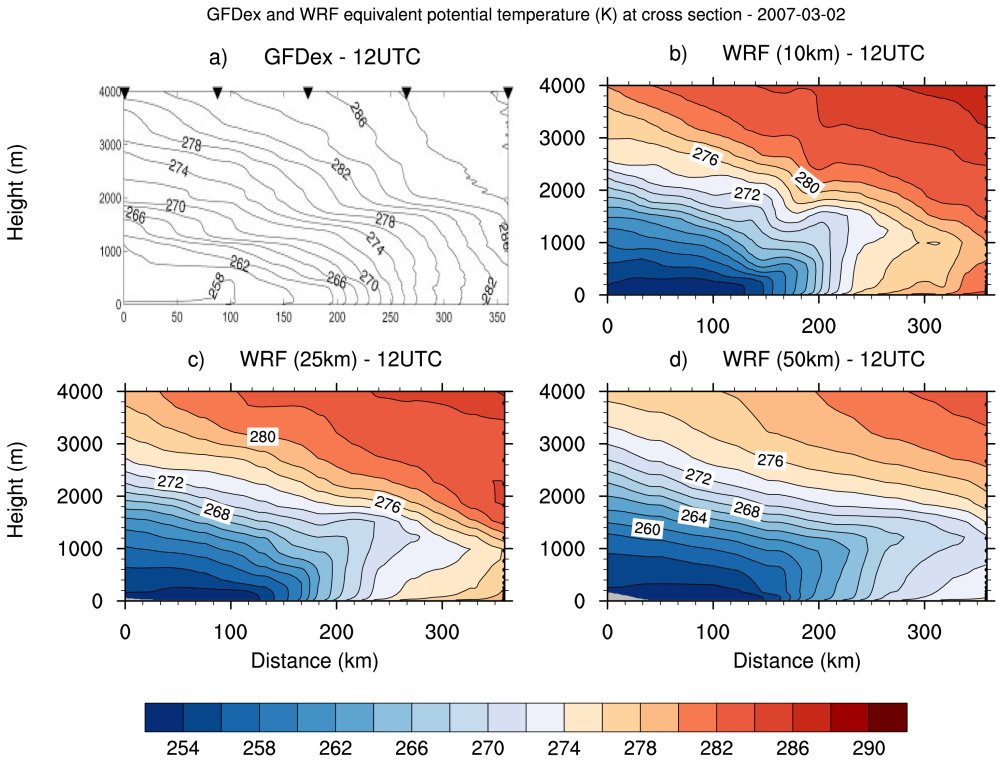

Figure 10: Cross section of equivalent potential temperature (K) from GFDex flight path on 2 March 2007 at 12UTC from the GFDex dropsonde observations (a), WRF10 (b), WRF25 (c), WRF50 (d). 'A' on Figure 3b marks 0 km on the cross section and 'B' marks 358 km on the cross section.

A combination of WRF simulated surface fluxes and in-situ observations reveal important differences between WRF simulated fluxes due to resolution. On 6 March at 22 UTC, QuikSCAT observations show a strong BW in the Denmark Strait (Figure 3d). The surface

sensible (Figure 11) and latent (not shown) heat fluxes on this day reflect the large differences in wind speed across the WRF resolutions. WRF10 (Figure 11a) produced sensible heat fluxes greater than 500 W m^{-2} along the marginal ice zone, while WRF25 (Figure 11b), WRF50 (Figure 11c), and WRF100 (not shown) have fewer grid cells with large sensible heat fluxes. High-resolution WRF was better able to represent the marginal ice zone and thus had more grid cells with open or partially ice-covered ocean. So in WRF10 more open water was exposed to strong winds and large temperature and moisture gradients, and resulted in a larger ocean surface area covered by high fluxes when compared with the other WRF simulations. While the WRF simulations have similar sea ice extent, the high-resolution simulations are better able to capture the gradient from full ice cover to open ocean (not shown). The better simulated wind field and marginal ice zone in WRF10 allows for more grid points with high positive fluxes because where the highest winds are located more of the ocean surface is totally or partially ice-free.

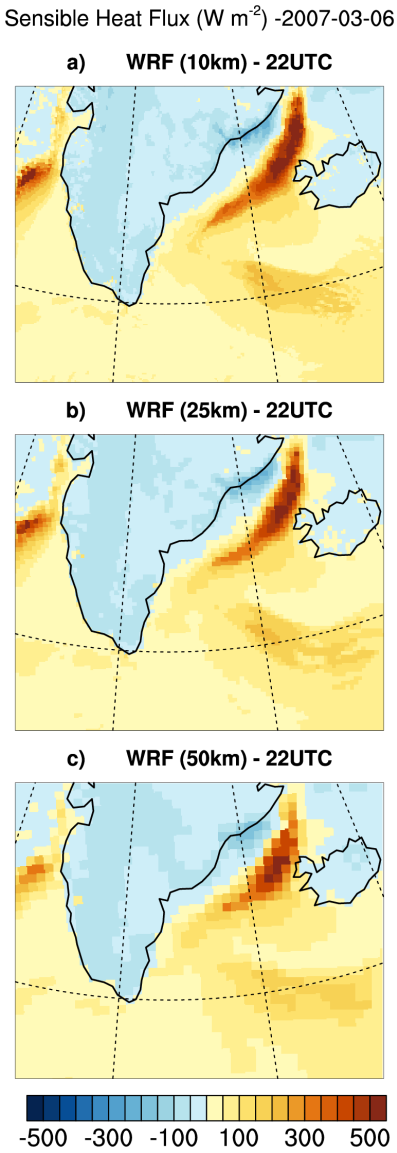

Figure 11: Surface sensible heat flux (W m^{-2} – positive upward) on 6 March 2007 at 22UTC from WRF10 (a), WRF25 (b), and WRF50 (c).

GFDex took near-surface observations during the four BW flights. The 2, 6, and 9 March BW flights took place over open-ocean, while the 5 March flight was over open water and the marginal ice zone [*Renfrew et al.*, 2009a]. Data from the 2 and 5 March flights and simulations are shown in Figure 12. On 2 March there is a large difference between the WRF and GFDex surface mixing ratio and temperature (Figure 12a and d). On 2 March, the 2 m mixing ratio and temperature best match between WRF10 and GFDex (Figure 12b and 12e); however the surface

bias results in large positive mixing ratio and temperature vertical gradients for WRF (Figures 12c and 12f), with the WRF10 gradients most closely matching the GFDex gradients. Additionally, on 2 March the 10 m simulated wind speed (Figure 12g) from WRF10 and WRF25 better represent the higher speeds from GFDex. On 5 March the surface and 2m variables and the wind speeds have less spread between resolutions and generally match the GFDex observations at the surface, 2 m, and 10 m.

The average RMSE and correlation between the model simulations and the GFDex observations are given in Table 3, and bolded RMSE values indicated RMSE values for WRF25, WRF50 and WRF100 that are significantly different than the WRF10 RMSE at the 95% confidence level. The mixing ratio gradient and temperature gradients have significantly different RMSE values, and decrease with increasing WRF resolution. The 10 m wind speed RMSE is significantly different for WRF50 and WRF100 and also decreases with increasing resolution. For the vertical gradients and 10 m wind speed the correlation with GFDex increases with higher WRF resolution. Surprisingly, the RMSE for the latent and sensible fluxes did not decrease with higher resolution despite the better representation of the physical variables with high resolution WRF.

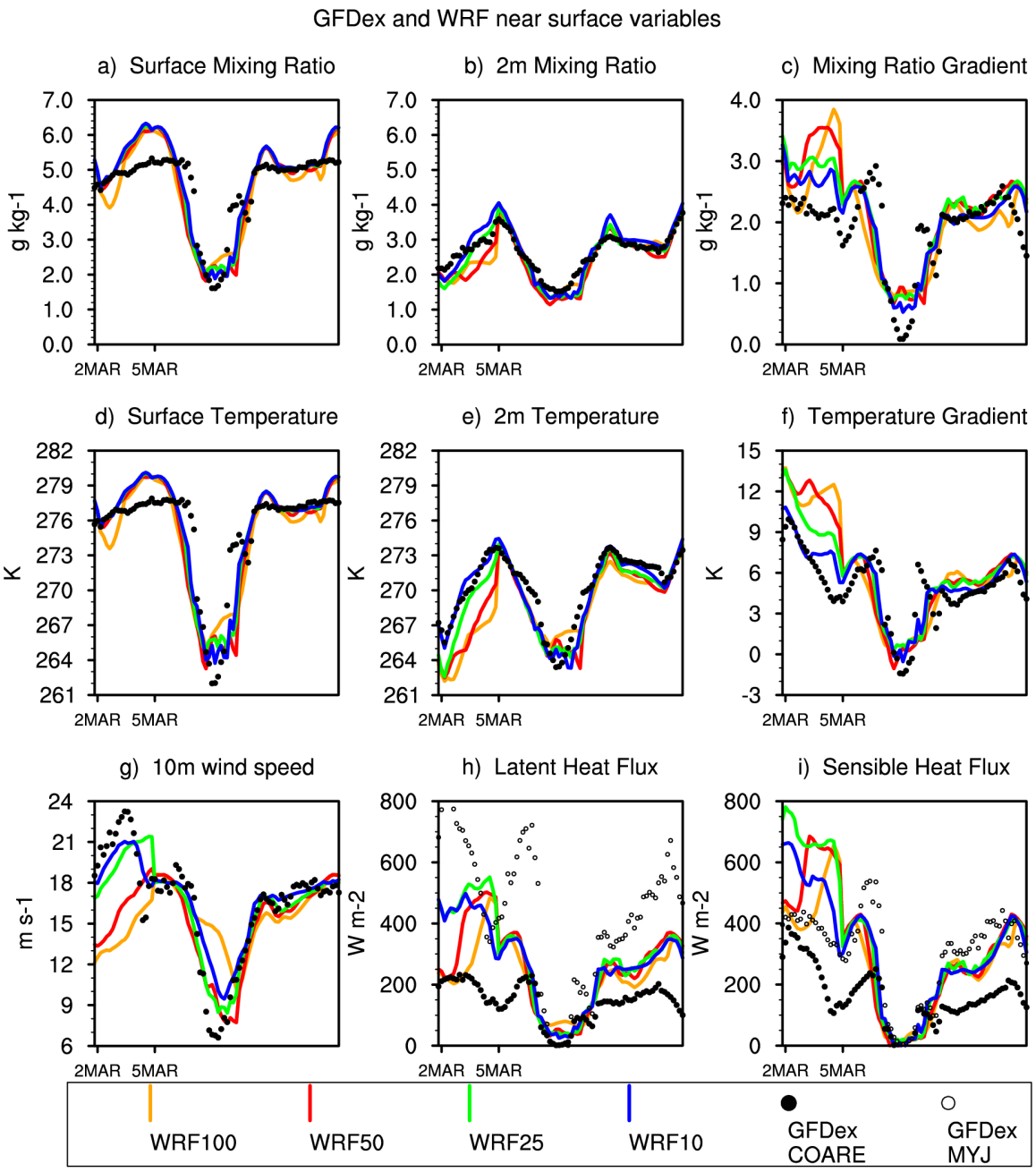

Figure 12: Surface variables and turbulent fluxes along the GFDex flight track on 2 and 5 March 2007, both taken around 14UTC. WRF10 is the blue line; WRF25 is the green line; WRF50 is the red line; WRF100 is the orange line; GFDex observations are the solid black dots; GFDex fluxes recalculated with the WRF MYJ parameterization are the unfilled black dots. The mixing ratios associated with the latent heat flux are in the top row: surface saturation mixing ratio (a), 2 m mixing ratio (b), and mixing ratio gradient (surface – 2m) (c). The temperatures associated with the sensible heat flux are in the middle row: surface temperature (d), 2 m temperature (e), and temperature gradient (surface – 2m)(f). The bottom row has 10 m wind speed (g), latent heat flux (h), and sensible heat flux (i).

	WRF10	WRF25	WRF50	WRF100
Surface mixing ratio ($kg\ kg^{-1}$)	0.64 0.89	0.64 0.88	0.67 0.87	0.67 0.84
2m mixing ratio ($kg\ kg^{-1}$)	0.41 0.98	0.42 0.97	0.48 0.96	0.42 0.95
Mixing ratio gradient ($kg\ kg^{-1}$)	0.41 0.75	**0.51** 0.68	**0.60** 0.62	**0.61** 0.51
Surface temperature (K)	1.9 0.91	2.1 0.88	**2.3** 0.86	2.2 0.84
2m temperature (K)	1.1 0.96	**1.5** 0.95	**2.1** 0.91	**2.3** 0.87
Temperature gradient (K)	1.3 0.84	**1.8** 0.79	**2.4** 0.74	**2.6** 0.67
10m Wind speed ($m\ s^{-1}$)	1.5 0.93	1.6 0.89	**2.6** 0.72	**3.4** 0.34
Latent Heat Flux ($W\ m^{-2}$)	133.7 0.85	151.2 0.77	128.67 0.68	**101.1** 0.57
Sensible Heat Flux ($W\ m^{-2}$)	156.0 0.90	**198.2** 0.83	174.0 0.73	144.2 0.65

Table 3: Root mean squared error (RMSE) and Correlation calculated between WRF and GFDex for near-surface variables shown in Figure 12. Values correspond to RMSE (top) and correlation (bottom) respectively. Bold RMSE values indicate that the WRF10 RMSE is statistically significant compared to WRF25, WRF50, or WRF100 RMSE at the 95% confidence level.

As seen in Figure 12, there are large differences between the simulations and the observations in the latent and sensible heat fluxes. In general the WRF fluxes are larger than the GFDex COARE fluxes, sometimes by more than 200 W m^{-2} (Figures 12h and 12i). The discrepancy between these flux values is surprising considering the physical variables for flux calculations – the vertical gradients and wind speed – agree relatively well between GFDex and the WRF simulations. There are two explanations for this difference. The first is related to surface conditions: on 2 March the WRF temperature and mixing ratio gradients between the surface and 2 m have a positive bias when compared with the GFDex gradients. Larger vertical gradients in WRF would lead to larger fluxes, which is what we observe on 2 March. WRF10, in particular, best matches the 2 m mixing ratio and temperature, but has a large positive bias for the surface mixing ratio and temperature; thus, the poor surface initialization in WRF10 could be

a large driver for the vertical gradient biases on 2 March. Previous WRF studies have found that the temperature gradient can be more important than wind speed for determining surface fluxes [*Kilpeläinen et al.*, 2011], so better initialization of the sea surface to more realistic temperatures could help improve the flux bias we see. Unfortunately, the Arctic is data sparse and we were not able to find satellite data of sufficient spatial and temporal resolution to attempt simulations initialized with observed sea surface temperatures.

The second potential reason the WRF fluxes have a positive bias is due to the WRF flux parameterization; on 5 March the temperature and mixing ratio gradients between the WRF simulations and GFDex are similar, yet all WRF resolutions have positive flux biases. Because the physical gradients and wind speed agree closely between WRF and GFDex, the way WRF calculates the fluxes must cause this bias. We investigated this algorithm bias several ways. First, we ran experiments using the YSU surface layer parameterization instead of MYJ, and the results also indicated a positive WRF flux bias (not shown). The YSU and MYJ parameterizations differ in how they determine friction velocity, stability, and roughness length. When strong winds lead to a large friction velocity ($u_* > 0.7$), both parameterizations use a single value for momentum, heat, and moisture roughness lengths (see Equations 2, 3, and 5). Therefore, we experimented with the roughness length calculation by altering the Charnock parameter to 0.015 from the default value of 0.018 because the lower value is more appropriate for open-ocean [*Charnock*, 1955], but this did not result in a noticeable change in surface fluxes in either the MYJ or YSU simulations (not shown).

Finally, we used the MYJ parameterization to re-calculate the latent and sensible heat fluxes using the GFDex observed sea surface and 2 m mixing ratios and temperatures, and the 10 m wind speed to calculate the friction velocity. The re-calculated latent heat flux (Figure 12h)

had a positive bias even greater than the WRF fluxes, and the re-calculated sensible heat flux (Figure 12i) had a positive bias around the same magnitude as the WRF simulation biases. Because the physical mixing ratio and temperature gradients and the 10 m winds going into the flux calculation were the same as the COARE values, we can narrow down which variables may be causing the WRF flux bias. The WRF calculated friction velocity exceeded the GFDex COARE calculated friction velocity at all open water points, and a larger friction velocity would cause both larger sensible and latent heat fluxes, as seen in the re-calculated fluxes. In addition, because of the large friction velocities, the re-calculated fluxes used a single value for momentum, heat, and moisture roughness lengths, while the COARE algorithm uses separate roughness lengths [*Fairall et al.*, 2003]. The COARE stability parameterization [*Fairall et al.*, 2003] is also more detailed than the MYJ stability parameterization. Thus, we conclude that the root cause for the bias between WRF fluxes and GFDex reported fluxes is related to the simplified surface layer parameterization in WRF, specifically the calculation of friction velocity in high wind conditions, the use of a single roughness length value for momentum, heat, and moisture, and the stability calculation that are not appropriate for conditions such as those observed around Greenland. Despite the positive WRF bias concerning fluxes, the spatial patterns we see with regard to where the largest fluxes are located, the total area covered, and the correlation between high winds and high fluxes demonstrates that high-resolution WRF capture the patterns expected for turbulent fluxes, even if the parameterization needs to be modified for this region.

d. Case Studies Summary

Table 4 provides a summary of the differences between each resolution simulation for each case study over the ocean grid points in the box shown in Figure 2. The table lists the

maximum and average values for 10 m wind speed and surface latent and sensible heat fluxes, all of which are important for understanding the atmosphere-ocean connection during mesoscale wind events. The maximum wind speeds are located in the ETJ or BW for each case study day, and for each day WRF10 simulated the highest maximum wind speed, and these maximum winds exceeded the WRF25 maximum winds by 5-11%, the WRF50 winds by 6-14%, and the WRF100 winds by 24-32%. Additionally, comparison between WRF10 and QuikSCAT show that QuikSCAT maximum wind speeds generally exceed WRF10 except 6 March, when the QuikSCAT sea ice mask obscured the Denmark Strait and likely the strongest winds. However, the average wind speed between all resolutions and QuikSCAT on each day was similar; the largest difference between WRF10 and WRF25 was 3% and between WRF10 and WRF100 was 22%. Spatial analysis shows that during the ETJ and BW events the higher-resolution WRF simulations yielded more correct wind fields during the mesoscale wind events due to more detailed and realistic PG forcing.

For all case study days WRF10 simulated the greatest maximum latent and sensible heat fluxes. The largest difference in maximum latent heat flux between WRF10 and WRF25 was 20%, though WRF10 was at most 6% higher than WRF25 for average latent heat flux. WRF10 exceeded WRF25 by at most of 29% for maximum sensible heat flux, but the average sensible heat flux values between the two were no more than 3% different, with WRF25 sometimes exceeding WRF10. However, the difference in maximum fluxes was larger when comparing WRF10 with WRF50 and WRF100: WRF50 (WRF100) had maximum latent heat flux values 3-32% (17-56%) less than WRF10 values and maximum sensible heat flux values 5-60% (29-71%) less than WRF10 values. The average values were closer and WRF10 differed from WRF50 (WRF100) by a maximum of 9% (17%) for latent heat flux and 5% (21%) for sensible heat flux.

	Maximum wind speed ($m\ s^{-1}$)	Average wind speed ($m\ s^{-1}$)	Maximum latent heat flux ($W\ m^{-2}$)	Average latent heat flux ($W\ m^{-2}$)	Maximum sensible heat flux ($W\ m^{-2}$)	Average sensible heat flux ($W\ m^{-2}$)
Feb. 21, 2007 07 UTC	34.7	15.1	610.0	69.3	775.0	31.2
	32.4 (93)	15.1 (100)	487.9 (80)	68.6 (99)	548.6 (71)	32.3 (103)
	32.7 (94)	15.0 (100)	412.0 (68)	66.3 (96)	308.3 (40)	31.3 (100)
	25.6 (74)	14.9 (99)	268.8 (44)	62.0 (89)	221.7 (29)	24.7 (79)
	26.9 (76)	13.1 (87)	-	-	-	-
	42.2 (122)	14.5 (96)	-	-	-	-
Mar. 2, 2007 22 UTC	34.9	13.3	883.2	168.9	1528.7	177.9
	30.9 (89)	12.9 (97)	776.5 (88)	158.7 (94)	1291.6 (84)	173.3 (97)
	29.0 (83)	12.2 (92)	613.1 (69)	153.5 (91)	984.6 (64)	168.5 (95)
	25.6 (73)	11.8 (89)	556.4 (63)	143.1 (85)	795.5 (52)	154.3 (87)
	26.2 (75)	10.4 (78)	-	-	-	-
	45.8 (131)	12.8 (96)	-	-	-	-
Mar. 5, 2007 22 UTC	36.1	12.1	558.5	107.2	830.8	84.9
	34.2 (95)	11.9 (98)	552.8 (99)	108.4 (101)	789.1 (95)	87.8 (103)
	33.2 (92)	12.1 (100)	551.1 (99)	111.4 (104)	791.8 (95)	90.8 (107)
	31.2 (86)	12.4 (102)	464.0 (83)	103.2 (96)	587.2 (71)	79.7 (94)
	26.7 (74)	9.4 (78)	-	-	-	-
	41.4 (115)	11.7 (97)	-	-	-	-
Mar. 6, 2007 22 UTC	42.2	10.6	503.6	99.4	813.8	71.6
	39.2 (93)	10.5 (99)	501.4 (100)	96.8 (97)	663.7 (82)	70.0 (98)
	37.4 (89)	10.7 (100)	487.2 (97)	95.4 (96)	613.9 (75)	69.5 (97)
	34.5 (82)	10.8 (102)	343.8 (68)	82.3 (83)	421.8 (52)	56.5 (79)
	28.9 (68)	9.2 (87)	-	-	-	-
	24.2 (57)	10.4 (98)	-	-	-	-
Mar. 9, 2007 07 UTC	34.8	14.5	629.1	167.3	861.5	114.8
	31.6 (91)	14.5 (100)	552.1 (88)	166.2 (99)	612.7 (71)	116.4 (101)
	30.1 (86)	14.1 (97)	470.5 (75)	159.8 (96)	478.6 (56)	115.8 (100)
	27.1 (78)	14.0 (97)	483.5 (77)	150.8 (90)	382.7 (44)	107.6 (94)
	25.4 (73)	11.5 (79)	-	-	-	-
	33.4 (96)	16.6 (114)	-	-	-	-

Table 4: GFDex case study maximum and average wind speed, latent heat flux, and sensible heat flux. These values are calculated from the oceanic portion of the model domain shown by the boxed region in Figure 2. Listed values correspond to WRF10, WRF25, WRF50, WRF100, ERA-I, and QuikSCAT top to bottom respectively. Dashes are given for the QuikSCAT and ERA-I flux values. ERA-I data was taken from the daily 06UTC output for Feb. 21 and Mar. 9, and the 00UTC following day output for Mar. 2, 5, and 6. Following each value is the percentage of the corresponding WRF10 value given in parenthesis.

Because latent and sensible turbulent fluxes depend on wind speed, simulating a realistic wind field including the strongest speeds is essential for capturing the strongest fluxes. As seen in Figures 6 and 11, the high-resolution WRF has concentrated maximum sensible heat fluxes

co-located with the strongest winds over open-ocean. WRF has a positive flux bias that appears to be related to both incorrectly initialized surface variables due to lack of observational data with sufficiently high temporal and spatial resolution and a parameterization problem that is not related to resolution. However, the differences we see between the flux fields are caused by the wind fields, which are better simulated by high-resolution WRF.

4. Two-month Simulations

A simulation from 1 February – 31 March 2007 was run for each WRF resolution to examine longer-term implications of model resolution since the previous case studies are snapshots of short-lived mesoscale wind events. This analysis focuses on the surface winds and surface latent and sensible heat fluxes because of their impact on the ocean and is restricted to the boxed area in Figure 2. The two-month average values of these variables will be analyzed to assess differences due to resolution. However, the largest wind speeds and fluxes occur during BW and tip jets, so to better understand how the extreme conditions vary due to model resolution, the standard deviation and 95th percentile values of the variables are discussed as well.

BW and both ETJ and WTJ dominate spatial plots of both the mean and the highest 95th percentile wind speeds (not shown) over this two-month period. As with the case studies, the mesoscale wind features are more distinct in high-resolution WRF; the difference between 95th percentile WRF10 and both WRF50 and WRF100 wind speeds shows WRF10 with winds 4-6 m s^{-1} greater in the ETJ and BW regions, while both WRF50 and WRF100 have winds 6-8 m s^{-1} greater in the wake regions of Cape Farewell and the Geikie Plateau. The mean wind speed for the two months is similar for all WRF simulations, but the maximum values from the two-month mean and two-month 95th percentile wind fields are from WRF10 and decrease with resolution (Table 5). Both the average and 95th percentile winds reinforce that the high-resolution

simulations show stronger winds along the southeast Greenland coast and better defined BW and tip jet features. The standard deviation in wind speed, particularly in the locations where barrier winds and tip jets occur, is also larger for high-resolution simulations, which means that these high-resolution simulations are able to capture extreme outlier events that low-resolution is not able to capture.

	Maximum wind speed ($m\ s^{-1}$)	Average wind speed ($m\ s^{-1}$)	Maximum latent heat flux ($W\ m^{-2}$)	Average latent heat flux ($W\ m^{-2}$)	Maximum sensible heat flux ($W\ m^{-2}$)	Average sensible heat flux ($W\ m^{-2}$)
Mean (Feb-Mar 2007)	17.3 15.5 (90) 15.0 (87) 14.0 (81)	11.7 11.7 (100) 11.5 (98) 11.5 (98)	222.9 192.6 (86) 178.8 (80) 175.0 (79)	100.8 101.2 (100) 93.6 (93) 90.3 (90)	284.4 231.9 (82) 212.2 (75) 197.9 (70)	75.9 78.9 (104) 72.9 (96) 68.7 (91)
95% values (Feb – Mar 2007)	35.9 32.2 (90) 30.3 (84) 28.8 (70)	20.1 20.1 (100) 19.7 (98) 19.4 (97)	627.1 524.9 (84) 460.1 (73) 463.0 (74)	279.5 278.4 (100) 259.5 (93) 244.2 (87)	840.3 982.0 (117) 708.3 (84) 632.1 (75)	240.6 253.7 (105) 236.0 (98) 221.1 (92)

Table 5: WRF two-month maximum and average wind speed, latent heat flux, and sensible heat flux. These values are calculated from the oceanic portion of the model domain shown by the boxed region in Figure 2. Listed values correspond to WRF10, WRF25, WRF50, WRF100 top to bottom respectively. Following each value is the percentage of the corresponding WRF10 value given in parenthesis.

The average and 95th percentile turbulent surface fluxes in this region are both large, reflecting the frequent presence of cold air over warm ocean waters and the influence of strong winds. The two-month mean fluxes for WRF10 and WRF25 have three areas of maximum oceanic heat loss that correspond to locations associated with BW or tip jets. The two-month mean WRF10 (Figure 13a) and WRF25 (Figure 13b) sensible heat flux exceeds 100 W m^{-2} along most of the southeast Greenland coast, with many points exceeding 150 W m^{-2}. WRF50 (Figure 13c) has fewer grid cells with fluxes exceeding 100 W m^{-2} in locations with strong surface winds,

possibly because WRF50 simulates lower wind speeds and less distinct mesoscale wind features. All simulations show a sharp division between the open ocean, with high mean fluxes, and sea ice, where there are low or negative fluxes. In general, the latent heat fluxes (not shown) follow a similar pattern to the sensible heat flux field. Again, Table 5 illustrates that the maximum mean fluxes are from the WRF10 simulation and decrease in magnitude with decreasing resolution.

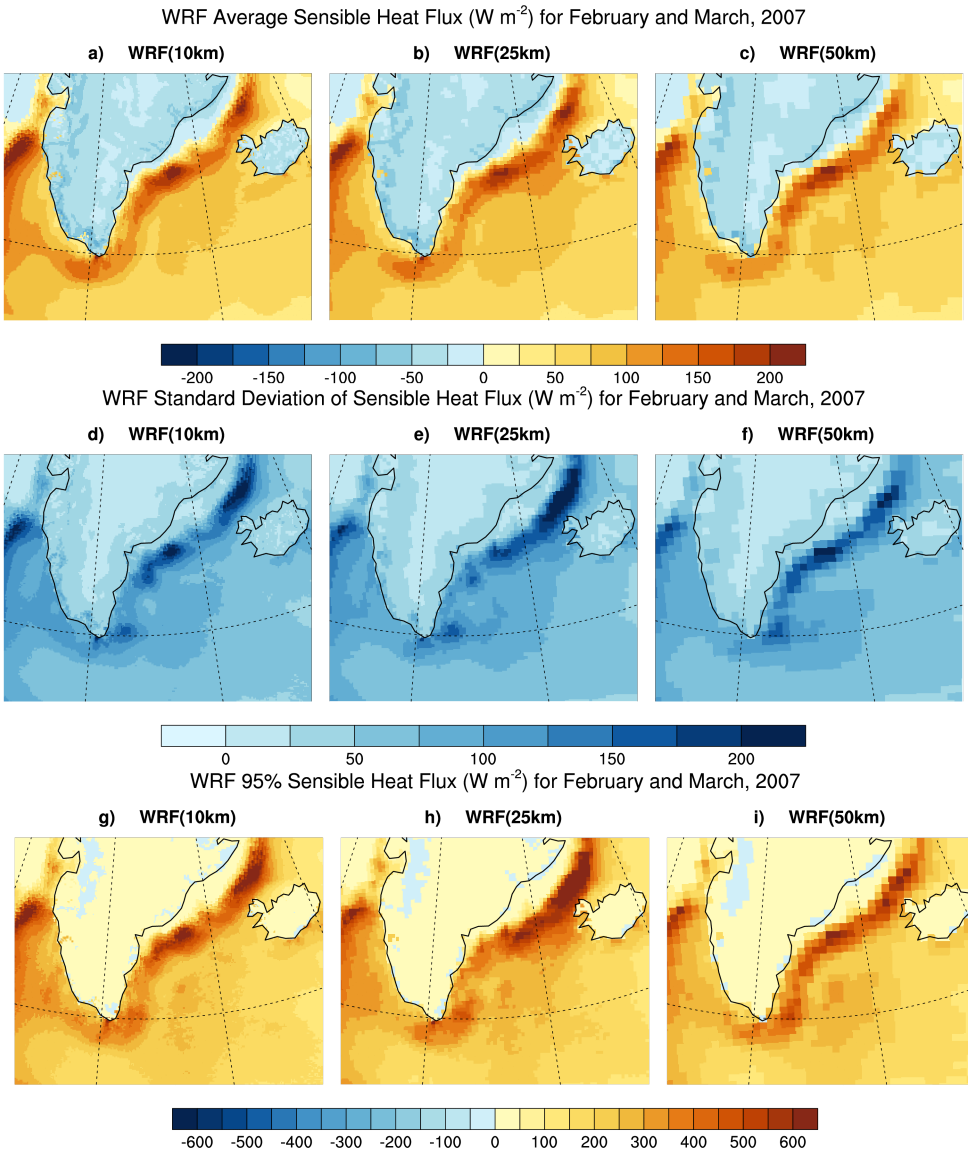

Figure 13: Surface sensible heat flux (W m^{-2} – positive upward) from the February 1 – March 31, 2007 simulations. The mean, standard deviation, and 95th percentile highest sensible heat flux values are shown for WRF10 (a, d, g - respectively), WRF25 (b, e, h - respectively), and WRF50 (c, f, i - respectively).

The high-resolution WRF10 (Figure 13d) and WRF25 (Figure 13e) have the largest standard deviations for sensible heat flux, and because there are high standard deviations co-located with tip jets or barrier winds this means that these high-resolution simulations are able to capture the strongest fluxes from the ocean to the atmosphere that occur in this region. Along the Greenland coast in all WRF simulations, the highest 95th percentile latent and sensible heat fluxes exceed 600 W m^{-2}. For WRF10 (Figure 13g) and WRF25 (Figure 13h) there are many grid cells with sensible heat fluxes greater than 600 W m^{-2}; for WRF50 (Figure 13i) there are fewer grid cells with fluxes of this magnitude. The same pattern is true of latent heat flux values (not shown). In all cases, the highest of the 95th percentile sensible and latent heat fluxes are co-located with the regions where high-speed tip jet and barrier winds occur over open ocean. The maximum and average turbulent fluxes from the 95th percentile fields tend to have the highest magnitude in WRF10 simulations and decrease with decreasing resolution. In addition, the mean 95th percentile flux values and standard deviations shown in Table 5 also have the highest magnitude for WRF10 and decrease with decreasing resolution, and this reinforces that using high-resolution WRF results in more events with a larger net oceanic energy loss and would therefore be more likely to induce ocean convection when compared with WRF50 or WRF100 simulations. The total energy loss decreases with decreasing resolution, so the lower the WRF resolution the less likely the ocean would lose enough energy to cause convection.

5. Conclusion

Comparison between WRF simulations and available observational data reveal the importance of high-resolution in accurately simulating the mesoscale BW and tip jets that occur around the southeast Greenland coast. In general, higher resolution WRF simulations had similar and more physically realistic winds and PG fields when compared with lower resolution WRF.

While all model resolutions tended to simulate the placement of synoptic features similarly, the higher resolution simulations were better able to capture local modifications to the synoptic pressure field and the resulting intense winds. The low-resolution WRF simulations used terrain that was smoothed out – too high over the ocean and too low inland – so physically realistic pressure gradients did not build up and force strong mesoscale winds in the correct locations.

Comparisons between GFDex dropsondes and WRF indicate that WRF10 simulated the vertical structure of the ETJ and BW best when compared with WRF25 and WRF50. We have confidence that WRF10 physically models the boundary layer well because the WRF10 simulations generally capture the observed boundary layer winds and mixed layer depth, despite the near-surface equivalent potential temperature bias evident in the simulations. Comparisons between the ETJ and BW sensible heat flux fields show that the surface area covered by high fluxes is larger for higher-resolution WRF and for the BW cases, likely due to slightly stronger winds and a larger near-surface temperature gradient. In addition, high-resolution WRF simulated stronger maximum fluxes in the case studies and two-month simulations. However, the main concern was that WRF had a positive flux bias that is likely due to surface conditions and model parameterizations, neither of which can be improved by increasing resolution. Investigations into improved surface initialization did not return any data with enough spatial and temporal resolution to be included in the simulations.

This study shows that using WRF at 10 km resolution is necessary for properly simulating the mesoscale wind field and boundary layers associated with BW and tip jets. Because turbulent fluxes depend on the wind field, a high-resolution atmosphere is necessary for simulating localized and intense energy removal from the ocean. Tables 3 and 4 illustrate that for both case studies and the two-month simulations the mean energy removal across all WRF

resolutions is similar, but that high-resolution WRF produces the maximum fluxes. Examination of spatial flux fields reveals that in high-resolution WRF the energy loss is concentrated in small areas instead of spread across the region, while low-resolution WRF has a smaller spatial area with the maximum fluxes. Without localized and intense fluxes, captured by high-resolution WRF, small-scale (~10 km) ocean convection might not occur because energy is not being lost in the necessary locations.

Ultimately we plan to use a fully coupled regional model, the Regional Arctic System Model (RASM), to study connections at the atmosphere-ocean interface, and better quantify how important mesoscale atmospheric features are for driving ocean convection. RASM uses WRF as its atmospheric component, and this study has shown the importance of using a high-resolution atmospheric model to best simulate tip jets and barrier winds. By using RASM to examine the atmosphere-ocean connection using a high-resolution atmosphere we can be sure that we are driving the ocean behavior with realistic and reasonable high-speed wind events. The use of the high-resolution atmosphere will be important for understanding how precisely tip jets and barrier winds impact the ocean over which they take place.

6. Acknowledgments

This research was supported by the United States Department of Energy (DOE) grants DE-FG02-07ER64462 and DE-SC0006178, as well as a NOAA ESRL / CIRES graduate fellowship. We thank two anonymous reviewers and the editor for their comments, which have improved this paper. Thanks also to Melissa Nigro and Mimi Hughes for guidance with the momentum budget analysis.

Chapter 3: Comparison of wintertime mesoscale winds over the ocean around southeastern Greenland in WRF and ERA-Interim

Abstract: Strong, mesoscale tip jets and barrier winds that occur over the ocean near southern Greenland have the potential for impacting deep convection in the ocean. The self-organizing map (SOM) training algorithm was used to identify and classify the range of 10 m wind patterns present during ten winters (1997-2007, NDJFM) in the ECMWF Interim Reanalysis (ERA-I) and from a regional simulation using the Weather Research and Forecasting (WRF) model at 50 km into a SOM. The SOM is used to identify differences in the manifestation of westerly tip jets, easterly tip jets, and barrier flow. The North Atlantic Oscillation (NAO) index is well correlated with the type of tip jet present at Cape Farewell, but the NAO was not well correlated with the absence or presence of barrier flow. WRF simulated patterns with strong barrier-parallel flow more frequently than ERA-I, and WRF also had faster coastal winds than ERA-I during all types of strong wind events. The difference in coastal winds is likely related to model resolution and the resulting ability of each model to simulate strong mesoscale winds that are driven by Greenland's steep terrain.

1. Introduction

Tip jets and barrier winds occur along Greenland's southeastern coast when wintertime synoptic storms interact with Greenland's steep topography. Barrier winds occur when air forced against a high, steep topographic barrier is unable to pass over the barrier and the flow adjusts to become parallel to the barrier [*Moore and Renfrew*, 2005; *Harden et al.*, 2011]. Tip jets, which can be either easterly or westerly, occur over the ocean to the southeast or southwest of Cape Farewell [*Doyle and Shapiro*, 1999; *Moore*, 2003, 2012]. Easterly tip jets occur when barrier

flow is no longer constrained by Greenland's topography [*Outten et al.*, 2009], while westerly tip jets form when flow accelerates around Cape Farewell and down sloping terrain [*Doyle and Shapiro*, 1999; *Moore and Renfrew*, 2005; *Våge et al.*, 2009]. The resulting strong surface winds occur over the Irminger Sea, a location identified as one of few sites in the world where open ocean convection occurs [*Bacon et al.*, 2003; *Pickart et al.*, 2003a; *Våge et al.*, 2011b]. During mesoscale wind events, the combination of fast winds and large temperature and moisture gradients between the cold, dry air and the relatively warm, moist ocean surface drive oceanic energy and buoyancy loss [*Petersen and Renfrew*, 2009; *Renfrew et al.*, 2009a; *Harden et al.*, 2011; *DuVivier and Cassano*, 2013; *Oltmanns et al.*, 2014].

Understanding how strong mesoscale wind events can force convection and the downwelling branch of the oceanic meridional overturning circulation is important to fully understand the climate. Previous studies have shown that strong easterly and westerly tip jets and barrier winds around Greenland are important for both preconditioning the ocean for and for forcing convection [*Spall and Pickart*, 2003; *Martin and Moore*, 2007; *Våge et al.*, 2011b; *Oltmanns et al.*, 2014]. Therefore, a detailed understanding of these mesoscale winds is beneficial for fully understanding ocean convection as a climatological process. Because observational data are sparse in this region, computer simulations are an important tool for understanding connections between the atmosphere and ocean.

Many ice-ocean models have been designed to use low spatial and temporal resolution atmospheric data from reanalyses or global models [*Hunke and Holland*, 2007; *Lisæter et al.*, 2007; *Kwok et al.*, 2008; *Hunke*, 2010]. Yet, we know global scale atmospheric models do not accurately represent mesoscale winds around Greenland [*Kolstad*, 2008; *Sproson et al.*, 2010] and that high-resolution regional climate models better represent mesoscale winds [*DuVivier and*

Cassano, 2013; *Shkolnik and Efimov*, 2013; *Tilinina et al.*, 2014]. Studies using ice-ocean models have shown that adding parameterizations of strong mesoscale winds is important for simulating open-ocean convection [*Våge et al.*, 2008b; *Condron and Renfrew*, 2013], and that using high resolution atmospheric forcing can increase the Atlantic meridional overturning circulation [*Jung et al.*, 2014]. To be sure the physical processes in an ice-ocean model are representative of the true air-sea interactions, we need to be sure that the mesoscale winds and corresponding atmospheric state are represented realistically.

Climatologies show that the strongest mesoscale winds around southeastern Greenland occur in winter and are associated with cyclones passing by and interacting with Greenland's steep coastal topography. Low-resolution models do not capture the steep terrain gradients necessary for realistic flow blocking, yet extant climatologies use relatively low-resolution model data from the NCEP/NCAR reanalysis (210 km, [*Moore*, 2003]), or the ERA-40 reanalysis (250 km, [*Våge et al.*, 2009]). The newer generation ECMWF Interim Reanalysis (ERA-I) has been used in climatologies (150 km, [*Harden et al.*, 2011; *Moore*, 2012; *Oltmanns et al.*, 2014]), but comparisons with the recently released 30 km Arctic System Reanalysis (ASR) [*Bromwich et al.*, 2010] show that ERA-I does not have as detailed spatial structure during extreme wind events and simulates extreme events less frequently than the ASR [*Moore and Renfrew*, 2014]. QuikSCAT satellite climatologies (25 km, [*Moore and Renfrew*, 2005; *Kolstad*, 2008]) provide valuable observational data over the Irminger Sea, but QuikSCAT cannot collect data over sea ice, which is typically present in winter along the southeastern Greenland coast. Additionally, QuikSCAT has twice-daily passes, but because mesoscale winds can be short lived the satellite may not capture the peak of an event. Analysis that uses the NARR reanalysis (32km,

[*Moore*, 2014]) has recently been used to identify four sub-types of tip jets that occur over the Irminger Sea. A detailed description of the extant climatologies will follow later in the paper.

In this study, we explore the variability in mesoscale wind events around southeastern Greenland. This study uses the self-organizing map (SOM) training algorithm to explore the diversity of wind events that would otherwise be indistinct. Additionally, we use differences in wind pattern frequency and details in how wind patterns are represented to understand differences between datasets with varying spatial resolution. The paper is organized as follows: data and methods used for analysis are explained in section 2. In section 3, the SOM pattern classification is described and compared with existing climatologies, including a discussion of how the SOM enhances these climatologies. Section 3 also explores why the differences in the winter mean wind speed between ERA-I and a Weather Research and Forecasting (WRF) model. Section 4 discusses implications of this study and future directions for exploration.

2. Data and Methods

a. ERA-Interim Reanalysis

ERA-I is a modern global reanalysis that is comparable in resolution to global climate models and other reanalysis products [*Dee et al.*, 2011]. ERA-I was found to have the overall best performance in the Arctic, particularly for wind speed, when compared to other reanalyses [*Lindsay et al.*, 2014] and it has been confirmed to reasonably represent strong wind events around Greenland observed during the Greenland Flow Distortion Experiment [*Renfrew et al.*, 2009a]. Therefore, this paper focuses on differences between the WRF and ERA-I representation of mesoscale winds and does not consider other reanalysis products. ERA-I analyses are

available every 6 hours and these data were interpolated from the 1.5° x 1.5° (150 km) product to the WRF grid so that direct comparisons could be made between datasets.

b. WRF model simulations

This study uses the Advanced Research WRF version 3.2.1 [*Skamarock et al.*, 2008] for regional simulations over a pan-Arctic domain (Figure 14) with 50 km horizontal grid spacing. A pan-Arctic domain was chosen so that the WRF data could be used for forcing regional ice-ocean models that fully represent circulation of the Arctic Ocean, and the 50 km resolution is the minimum resolution that can capture mesoscale wind events [*DuVivier and Cassano*, 2013] while still being computationally feasible for multi-decadal simulations. For this study we focus only on the winds located around Greenland's southeastern coast (Figure 14 inset).

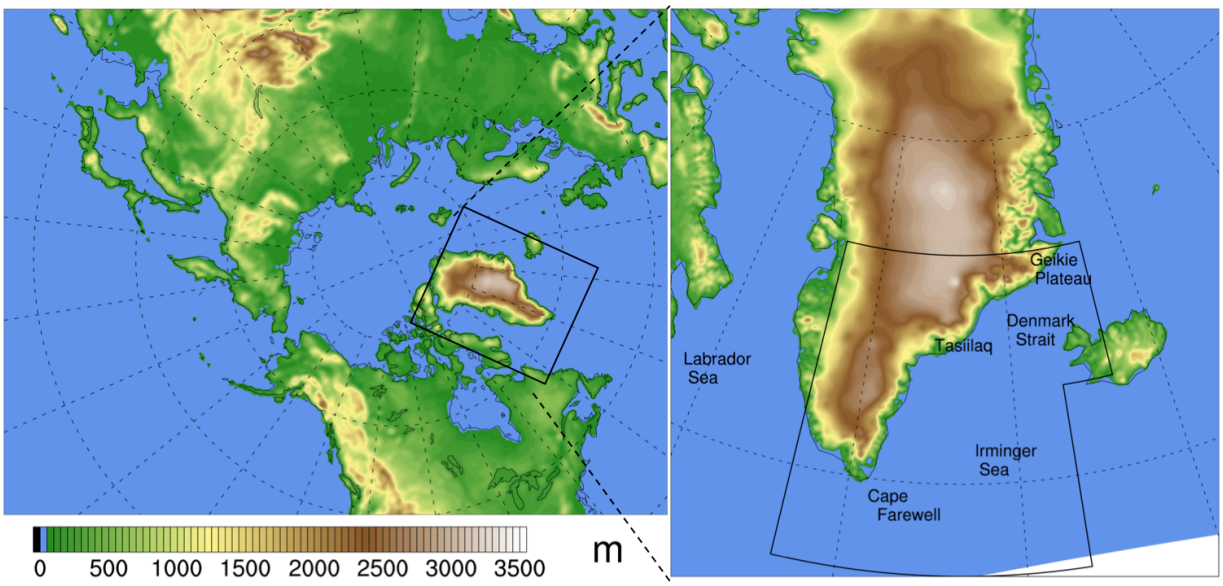

Figure 14: Map of pan-Arctic WRF domain showing the WRF terrain height (m), and inset of Greenland study region. The SOM training area is boxed in black. For reference, the width of the Denmark Strait is about 400 km from the Geikie Plateau to the northwestern tip of Iceland.

The WRF simulation uses 40 vertical levels, and over the ocean there are 10 levels in the lowest 1 km. ERA-I provides the lateral and lower boundary conditions, and the sea ice fraction

is specified from the National Snow and Ice Data Center Bootstrap Sea Ice Concentration satellite product, which has a 0.25° x 0.25° resolution [*Comiso*, 2008]. The WRF physics parameterizations used are: the Goddard microphysics scheme [*Tao and Simpson*, 1993], the Grell 3D sub-grid scale convection scheme [*Grell and Dévényi*, 2002], CAM longwave and shortwave radiation [*Collins et al.*, 2004], Noah land surface model [*Chen and Dudhia*, 2001], and the YSU planetary boundary layer [*Hong et al.*, 2006] with MM5 similarity theory in the surface layer [*Dyer and Hicks*, 1970; *Paulson*, 1970; *Webb*, 1970]. The WRF data are from a single, continuous simulation from September 1, 1989 through January 1, 2008.

The WRF model is not expected to produce identical weather to ERA-I due to the long simulation and large domain. To ensure similar large-scale circulation between the WRF simulation and ERA-I while still allowing WRF to respond dynamically to surface conditions, we spectrally nudge the top half of the atmosphere with ERA-I [*Cassano et al.*, 2011]. Temperature and winds in the top 20 levels of WRF were nudged to wavenumber two with nudging linearly ramped from no nudging at level 20 to a nudging strength of 0.0002 sec^{-1} at level 40. Skamarock et al. [2008] provide the precise meaning of these nudging parameters. We confined the nudging to the upper atmosphere and planetary wave scales so that the WRF and ERA-I large-scale circulation will be similar, but the mesoscale surface features will be unaffected.

c. Wind pattern classification

This study uses the SOM neural network algorithm to identify near-surface wind patterns around southeast Greenland. The SOM training algorithm is an unsupervised, iterative training process that identifies a user-specified number of representative patterns within a dataset [*Kohonen*, 2001; *Hewitson and Crane*, 2002; *Cassano et al.*, 2007] and has been shown to be a

robust method for identifying dominant patterns across a spectrum of individual weather patterns [*Reusch et al.*, 2005; *Sheridan and Lee*, 2011]. The SOM algorithm arranges similar patterns (also referred to as nodes) together into a two-dimensional array, or SOM, where the linear distance between patterns indicates the similarity of the pattern. The user specifies the number of patterns to be included in the SOM, and the representative patterns are determined objectively during training.

This project's SOM training algorithm is based on wintertime (NDJFM) wind data since these are the months when strong mesoscale winds occur [*Moore*, 2003]. In addition to the WRF and ERA-I data, two years of 10 km WRF data over the same domain and using the same parameterizations as the 50 km WRF simulation were used in the SOM training algorithm. However, to keep the focus of this paper on the comparison on ERA-I and WRF at 50 km, a comprehensive discussion of the comparison of the winds in the 10 km and 50 km WRF simulations is found in Hughes and Cassano [2015]. During training the grid must be identical for all data, so ERA-I and WRF data were interpolated to the 10 km WRF grid using a distance weighted average of the four nearest neighboring points.

The training data for ERA-I and WRF data spanned ten winters between 1997-2007; ERA-I analyses are available every 6 hours, and instantaneous WRF data are available every 3 hours. Both datasets are required for training so that the range of wind patterns across all datasets are taken into account when the SOM training algorithm determines the representative wind patterns that make up the SOM. We use the zonal and meridional wind components for grid points along the southeastern Greenland coast and over the ocean so that the SOM training algorithm identifies patterns based on mesoscale wind features' speed and direction (Figure 14 inset, boxed region). To train the SOM we used 10 m wind data from ERA-I and the lowest

model level (approximately 12 m) WRF wind data. The 10 m and lowest model level WRF winds were found to have small (less than 1 m s^{-1}) and statistically insignificant differences, so all subsequent analysis, after the SOM algorithm training, uses 6 hourly data and 10 m wind data for consistency between ERA-I and WRF.

The SOM can be likened to a digital elevation model (DEM), which represents a continuous field of topographic height at a finite number of grid points. A coarse DEM will broadly represent the topographic features but will not reveal details such as narrow but high mountains that are identifiable in a fine DEM. Both the coarse and fine resolution DEM are realistic but differ in how much detail is represented. The SOM behaves in the same way: a small SOM broadly represents the range of conditions in the training data while a large SOM resolves finer details present in the training data but not represented in the smaller SOM. A number of SOM array sizes (3x2, 4x2, 4x3, 6x4, 7x5, and 8x6) and training parameters were investigated during the training process, as detailed in Hewitson and Crane [2002].

For each SOM array size the training parameter combinations were analyzed and the SOM of that size was chosen to minimize the root mean squared difference (RMSD) between the patterns identified and the data used for training. All SOM sizes identified similar wind patterns with varying degrees of generalization, and the 7x5 array (Figure 15) was chosen because it represents the dominant wind patterns identified from climatologies of southeast Greenland, yet identifies physically meaningful differences between adjacent patterns that are not present with smaller SOM arrays and that are important for investigating differences between patterns. After the SOM has been determined, the data from each of the times from the ERA-I and WRF training datasets are mapped to one of the 35 SOM patterns based on the minimum RMSD

between that time's wind vectors and the wind vectors represented in the SOM patterns. The 7x5 SOM arrangement used for this work has an average RMSD of 2.61 m s^{-1} for all training samples.

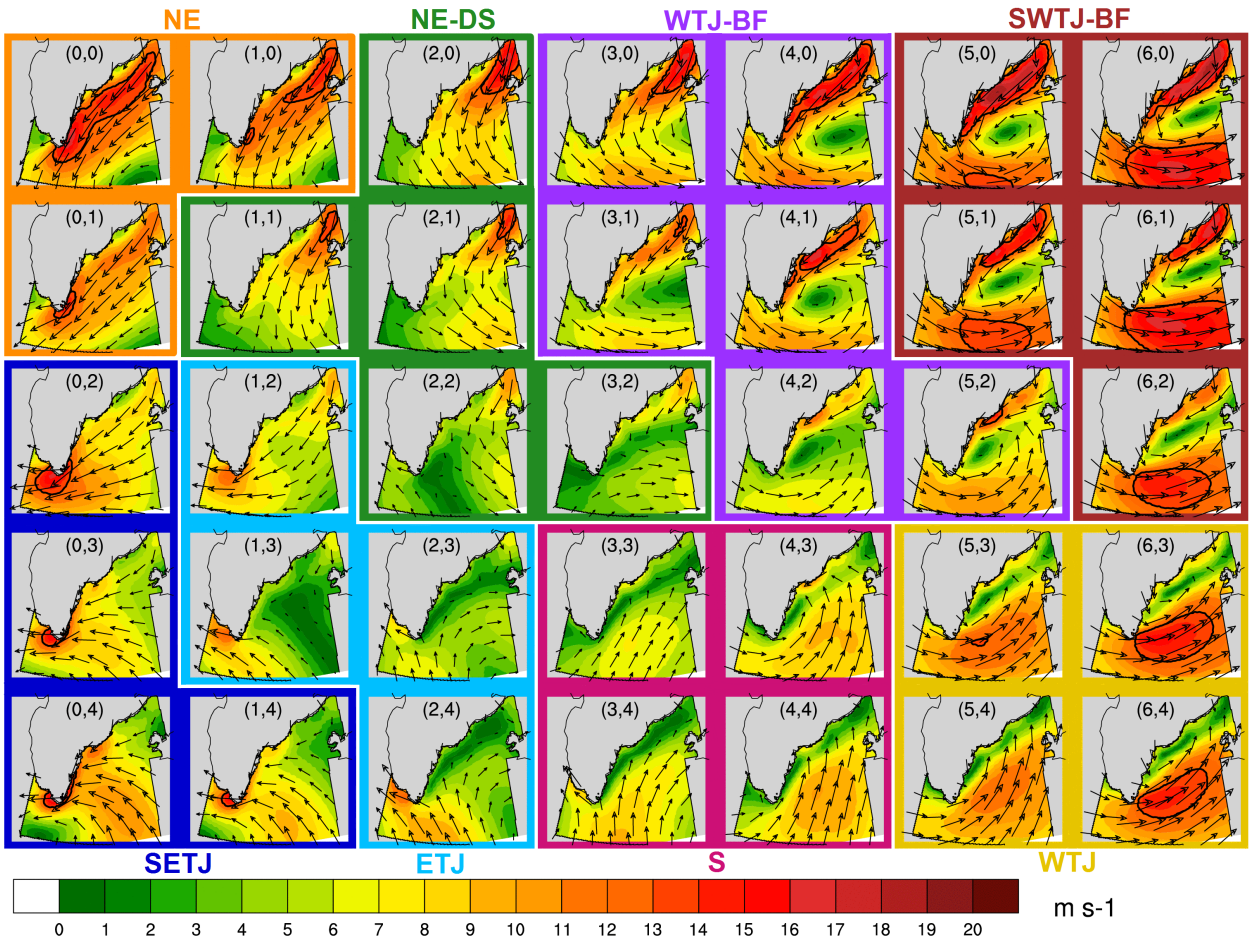

Figure 15: SOM of near-surface wind field with wind speed (m s^{-1}) shown by color shading. The dark black contour indicates "strong" winds that correspond to speeds greater than 13.8 m s^{-1}. Colored borders around the patterns and labels at the top and bottom of the SOM indicate groupings described in the text.

For each dataset, the pattern frequency is found by the determining the number of time periods from that dataset that maps to a particular pattern. By comparing the data mapped to each pattern from each dataset we are able to distinguish differences in how the datasets represent each of the 35 patterns in the SOM. The pattern average wind speed for a dataset is calculated by averaging all of the wind speed values that map to a particular pattern. The pattern frequency or

pattern average wind speed can be determined for all times or for a subset of times or training datasets.

d. Identifying difference between datasets

For a given dataset, the mean wind speed at each grid point can be calculated in two equivalent ways. The first method uses the wind speed from a dataset (e.g. ERA-I and WRF) over ten winters to calculate a mean for that dataset. The second method uses the SOM pattern frequencies and pattern average wind speed and combines them using Equation 6:

$$U_{mean} = \sum_{n=1}^{N} f_n U_n \tag{6}$$

where n represents a single pattern in the SOM, f_n is that pattern's frequency, and U_n is that pattern's mean wind speed. The sum over all SOM patterns gives the mean wind speed. The mean wind speed is found for each dataset using the corresponding pattern frequency and pattern average wind speeds for that dataset. Following Cassano et al. [2007] the difference in mean wind speed between two datasets can be found using Equation 7:

$$U_{diff(WRF-\square RA)} = \sum_{n=1}^{N} \left(\Delta f_n U_{ERA,n} + f_{ERA,n} \Delta U_n + \Delta f_n \Delta U_n \right) \tag{7}$$

Δf_n is the difference in the ERA-I and WRF frequency ($\Delta f_n = f_{ERA,n} - f_{WRF,n}$) for a given pattern, and ΔU_n is the difference in the ERA-I and WRF pattern average wind speeds ($\Delta U_n = U_{ERA,n} - U_{WRF,n}$). The sum over all patterns in the SOM is the difference in mean wind speed between the two datasets. At each grid point we calculate the average and variance, and the student's t-test is used to determine which grid points from the two datasets have a statistically significant difference at the 95% level.

We determine the relative contribution to the mean wind speed difference due to difference in frequency and in pattern mean wind speed using the method developed by Cassano et al. [2007] and described in Higgins and Cassano [2009]. In Equation 7, the sum of the first term, $\sum_{n=1}^{N} \Delta f_n U_{ERA,n}$, is the total contribution to the mean difference due to changes in SOM pattern frequency. The sum of the second term, $\sum_{n=1}^{N} f_{ERA,n} \Delta U_n$, is the total contribution to the mean difference due to intrapattern differences in pattern average wind speeds. The sum of the final term, $\sum_{n=1}^{N} \Delta f_n \Delta U_n$, is the total contribution to the mean difference that is due to changes in frequency and intrapattern differences working together. The sum of each of the three terms for an individual pattern is the total contribution to the mean wind speed difference for that pattern.

To calculate the percent contribution of the total frequency, total intrapattern, and total combined terms to the mean difference we used the percent contribution of each grid point. We took the constructive (positive) and destructive (negative) contributions into account separately and then added them together for the total percent contribution to the mean wind speed difference. In order to focus on the region with the largest differences, all percent contribution calculations use only points at which there was a statistically significant difference at the 95% level and the magnitude of wind speed difference was greater than 1 m s^{-1}. The use of a minimum wind speed difference threshold also avoids large percent differences when the wind speed is small. The percent contribution of each pattern to the mean difference uses the same method described above.

3. Results

a. SOM wind patterns

The SOM shows the total range and variability of wintertime wind patterns across the ocean south of Greenland (Figure 15). The patterns with the largest differences from one another are mapped to the corners of the SOM and tend to be more extreme, while smoothed or transitional patterns are near the center. Patterns with barrier-parallel winds along the southeast coast are in the topmost rows of the SOM, and patterns with weak coastal winds are in the bottom rows. Additionally, the left columns of the SOM have winds with an easterly component near Cape Farewell while the right columns have winds with a westerly component near Cape Farewell. The patterns in the four corners of the SOM correspond to the four sub-types of tip jets chosen subjectively in Moore [2014]: northeasterly (pattern 0,0), southeasterly (pattern 0,4), northwesterly (pattern 5,0), and southwesterly (pattern 5,4). However, the SOM training algorithm objectively determined the patterns shown in the SOM, and the SOM is shows the range of manifestations of these wind patterns.

To facilitate discussion of particular types of wind patterns and how the representation of these patterns differs in ERA-I and WRF, we have subdivided the SOM into groups (colored outlines in Figure 15). The 35 SOM patterns were grouped into the following eight categories: northeasterly flow (NE, orange); northeasterly flow in the Denmark Strait (NE-DS, green); westerly tip jet with barrier flow (WTJ-BF, purple); strong westerly tip jet with barrier flow (SWTJ-BF, red); strong easterly tip jet (SETJ, dark blue); easterly tip jet (ETJ, light blue); southerly flow (S, magenta); westerly tip jet without barrier flow (WTJ, yellow). Initial groupings were defined objectively based on the RMSD and correlation between adjacent SOM patterns' zonal and meridional wind components and total wind speed. When RMSD and correlation did not clearly identify the group to which a pattern belonged, a subjective assessment of the physical similarity of winds in adjacent patterns and a threshold value of

"strong winds" (13.8 m s^{-1} – solid black contour in Figure 15 - "near gale" on the Beaufort Sea Scale) were used to place those patterns into the final groups shown in Figure 15. For the remainder of this paper we will primarily discuss the SOM data with respect to these groups.

b. Comparison with climatologies

This study focuses on comparing spatial variability between the WRF and ERA-I datasets and is not itself a climatology due to the relatively short ten-winter period. However, we briefly compare ERA-I and WRF with existing climatologies to verify that ten years capture the regional mean wind state and also to understand what additional information is provided by a SOM analysis that is not provided in a more traditional climatology. The Icelandic Low in ERA-I and WRF align well and the strength is similar, which is shown by the small differences in mean sea level pressure (Figures 16a and 16b), and is a result of the upper atmospheric spectral nudging in WRF. Therefore, differences in the mesoscale wind representation are not due to differences in large scale forcing but instead are due to differences in dataset physics, dynamics, and/or resolution.

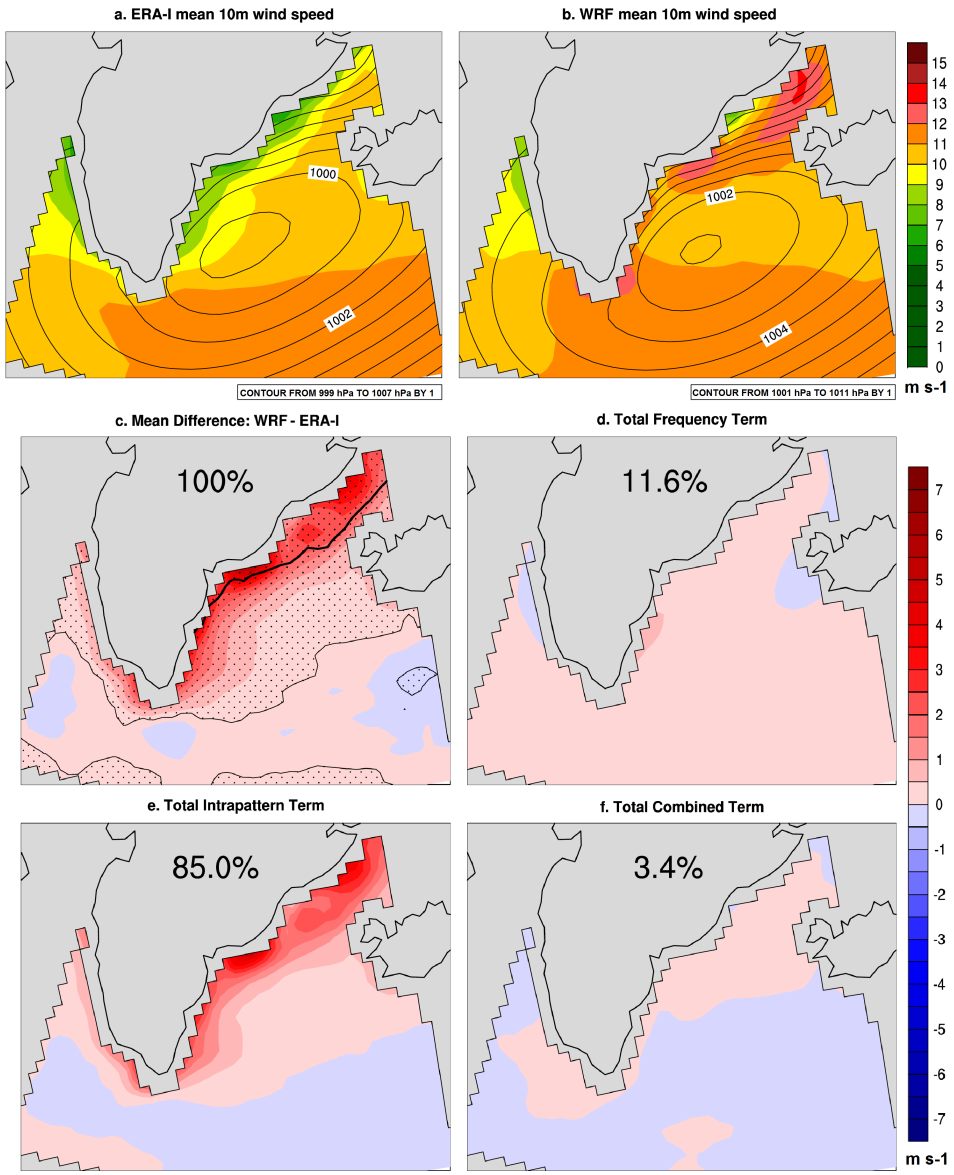

Figure 16: Mean 1997-2007 winter 10 m wind speed (m s^{-1} – shading) and sea level pressure (hPa – black contours) for (a) ERA-I and (b) WRF and the (c) mean wind speed difference (WRF-ERA). Contributions to the mean difference due to (d) total frequency differences, (e) total intrapattern variability, and (f) total combined frequency and intrapattern differences. Stippling in Figure 16c indicates the area of statistically significant difference between the two datasets at the 95% confidence level.

In a 1979-2012 winter (DJF) climatology using ERA-I, Moore (2012) found mean wind speeds of 8-10 m s^{-1} along the Greenland coast and speeds south of Cape Farewell around 11-12 m s^{-1} (Figure 2b in [*Moore*, 2012]). The ERA-I ten-winter mean wind speed (Figure 16a)

matches the 34-year spatial pattern and magnitude of wind speeds. A 1999-2004 winter (DJF) QuikSCAT climatology identifies three locations with costal wind speed maxima: south of Cape Farewell, south of Tasiilaq, and in the Denmark Strait [*Moore and Renfrew*, 2005]. The WRF ten-winter mean wind speed (Figure 16b) has three coastal wind speed maxima that occur in the same locations and have similar magnitude (13-14 m s^{-1}) as the observations. The observed coastal wind speed maxima are not present in ERA-I, but away from the coast, the QuikSCAT [*Moore and Renfrew*, 2005] and ERA-I [*Moore*, 2012] climatologies and ten-winter means agree well.

Wile the patterns identified in the SOM (Figure 15) correspond to types of winds identified in previous climatologies, using a SOM allows us to identify how frequently different patterns occur and to understand differences in pattern frequency for each dataset. The frequency data for each group of patterns over the ten-winter period (1997 to 2007, 6652 times from each dataset) is shown in Figure 17a, and both datasets represent all types of patterns but with different frequencies. The difference in WRF frequency relative to ERA-I is shown below the ERA-I frequency for each pattern, and statistically significant differences in the frequencies were calculated using the method from Cassano et al. [2007]. WRF simulates patterns of NE, WTJ-BF, SWTJ-BF, and SETJ more frequently than ERA-I. The patterns simulated more frequently by WRF have winds driven by strong topographic influences [*Outten et al.*, 2009; *Harden and Renfrew*, 2012]. Conversely, NE-DS, ETJ, southerly flow, and WTJ patterns are more frequent in the ERA-I data than the WRF data. The largest and statistically significant differences in frequency tend to occur in patterns at the corners and on the edges of the SOM (Supplementary Figure 1), which indicates that the largest differences in WRF and ERA-I occur in the most

extreme versions of the patterns present in the SOM. The implications for the difference in frequencies will be addressed in detail in section 4.

a. 1997-2007 ERA-I group frequency and difference (WRF - ERA-I)

ERA-I: 8.19% **WRF: 2.03%**	ERA-I: 16.61% **WRF: -2.27%**	ERA-I: 15.70% WRF: 0.65%	ERA-I: 13.31% **WRF: 1.70%**
ERA-I: 11.41% **WRF: 3.76%**	ERA-I: 10.27% **WRF: -1.29%**	ERA-I: 11.22% **WRF: -1.61%**	ERA-I: 13.29% **WRF: -2.96%**

b. 1997-2007 ERA-I and WRF correlation with NAO monthly index

ERA-I: -0.48 WRF: **-0.25**	ERA-I: **0.21** WRF: 0.35	ERA-I: **0.06** WRF: **0.05**	ERA-I: **0.26** WRF: 0.46
ERA-I: **-0.20** WRF: -0.32	ERA-I: **-0.23** WRF: -0.28	ERA-I: **0.07** WRF: **0.05**	ERA-I: **0.23** WRF: **0.24**

Figure 17: 1997-2007 winter (NDJFM) (a) ERA-I group frequencies and group frequency difference (WRF-ERA), and (b) correlation between ERA-I and WRF group frequency and NAO monthly index. For Figure 17a, grey shading indicates the relative ERA-I frequency for each pattern; the difference in group frequency between WRF and ERA-I is shown below the ERA-I frequency and bold text indicates statistically significant differences. For Figure 17b bold text indicates correlations that are statistically significant at the 95% level.

Moore [2003] and Vage et al. [2009] found that westerly tip jets are correlated with the positive phase of the North Atlantic Oscillation (NAO), while easterly tip jets are correlated with the negative phase of the NAO. The correlation of monthly frequencies for ERA-I and WRF with

the corresponding monthly NAO index (NOAA-CPC) over the ten-winter period is shown in Figure 17b. In agreement with Moore [2003], we find that SWTJ-BF and WTJ patterns are most strongly correlated with a positive NAO, while NE, SETJ, and ETJ patterns are inversely correlated with a positive NAO. The magnitude of the correlation coefficient is largest around corners of the SOM while correlation coefficients for the center patterns have smaller magnitude (Supplementary Figure 2). Varying phases of the NAO will result in different wind directions near Cape Farewell [*Moore*, 2003; *Våge et al.*, 2009], so it makes sense that patterns on the edges and corners of the map have the largest correlations to the NAO because they are most different from one another and span the range of idealized NAO behavior. The center, transitional patterns are not expected to be as well correlated with the NAO since they may exhibit winds representative of both NAO phases.

The SOM has 15 patterns (43% of the total patterns) that are classified as variations of westerly tip jet, yet the strength of correlation with the NAO for patterns in these groups varies. While the WTJ-BF and SWTJ-BF are visually similar, patterns belonging to strong variation have higher correlations with a positive NAO. SWTJ-BF and WTJ patterns have regions of strong winds in the westerly tip jet but differ with respect to inclusion of barrier flow (Figure 15). Yet patterns in both these groups have similar, positive correlations with the NAO. Therefore, the NAO appears to be correlated more with the strong westerly tip jet and not reflective of how barrier flow is represented. Thus, the NAO may not be a good gauge for ocean response to strong wind events because it is not well correlated with barrier flow and previous studies have found that barrier flow is important for determining atmosphere-ocean fluxes [*Harden et al.*, 2011].

Bakalian et al. [2007] found that the latitude of the Icelandic Low was also important for determining the frequency of westerly tip jets, and Moore et al. [2011] showed that other modes

of variability, such as the East Atlantic teleconnection or the Canadian Polar Trough, in conjunction with the NAO are important for determining the types of tip jets that occur near Cape Farewell. The combination of these studies and our results showing that for westerly tip jets NAO is not well correlated with barrier flow indicate that complexities arise when using a large scale index for predicting ocean response to atmospheric forcing.

c. Differences in WRF and ERA-I

Over most of the southeast Greenland coast and the southern Irminger Sea WRF has faster mean wind speeds than ERA-I (Figure 16c), and adjacent to the coast the difference is significant at the 95% level. The largest differences are found near the coast where WRF speeds exceed ERA-I speeds by up to 6 m s^{-1}. The weaker ERA-I winds are consistent with previous work that found ERA-I underestimated wind speeds in high wind conditions [*Harden et al.*, 2011; *DuVivier and Cassano*, 2013; *Oltmanns et al.*, 2014; *Tilinina et al.*, 2014], but the prominent coastal differences indicate there may be additional differences between WRF and ERA-I related specifically to flow that is influenced by the topography.

Greenland's terrain can block the synoptic-scale flow, which causes the sea level pressure along the southeastern coast to increase. Compared to ERA-I, WRF's higher resolution topography resolves steeper coastal terrain gradients [*DuVivier and Cassano*, 2013]. Because of the more realistic topography, WRF has greater blocking than ERA-I, which is shown by the higher coastal sea level pressures and larger mesoscale pressure gradient in WRF (Figures 16a and 16b). Over the Irminger Sea, synoptic-scale pressure gradients primarily drive winds, and topographic effects on the pressure gradient are less important. Consequently, better topographic representation impacts the wind speeds along the coast but is not as important for resolving the forcing and wind speeds over the ocean.

The group average wind speed (Figure 18a) is calculated using all the times that map to patterns within a particular group and reflects the patterns shown in the SOM. In comparing the ERA-I and WRF group average wind speeds we use the t-test to determine which grid points are statistically different at the 95 % confidence level, and the mean and variance at each grid point are calculated from the individual events that map to a particular group. WRF has faster coastal winds for all groups, and the coastal wind speed difference is largest for the WTJ-BF and SWTJ-BF (Figure 18b). Over the ocean, the sign of the wind speed difference depends on the type of pattern, which indicates that away from topography there is not the consistent difference between WRF and ERA-I that is found along the coast.

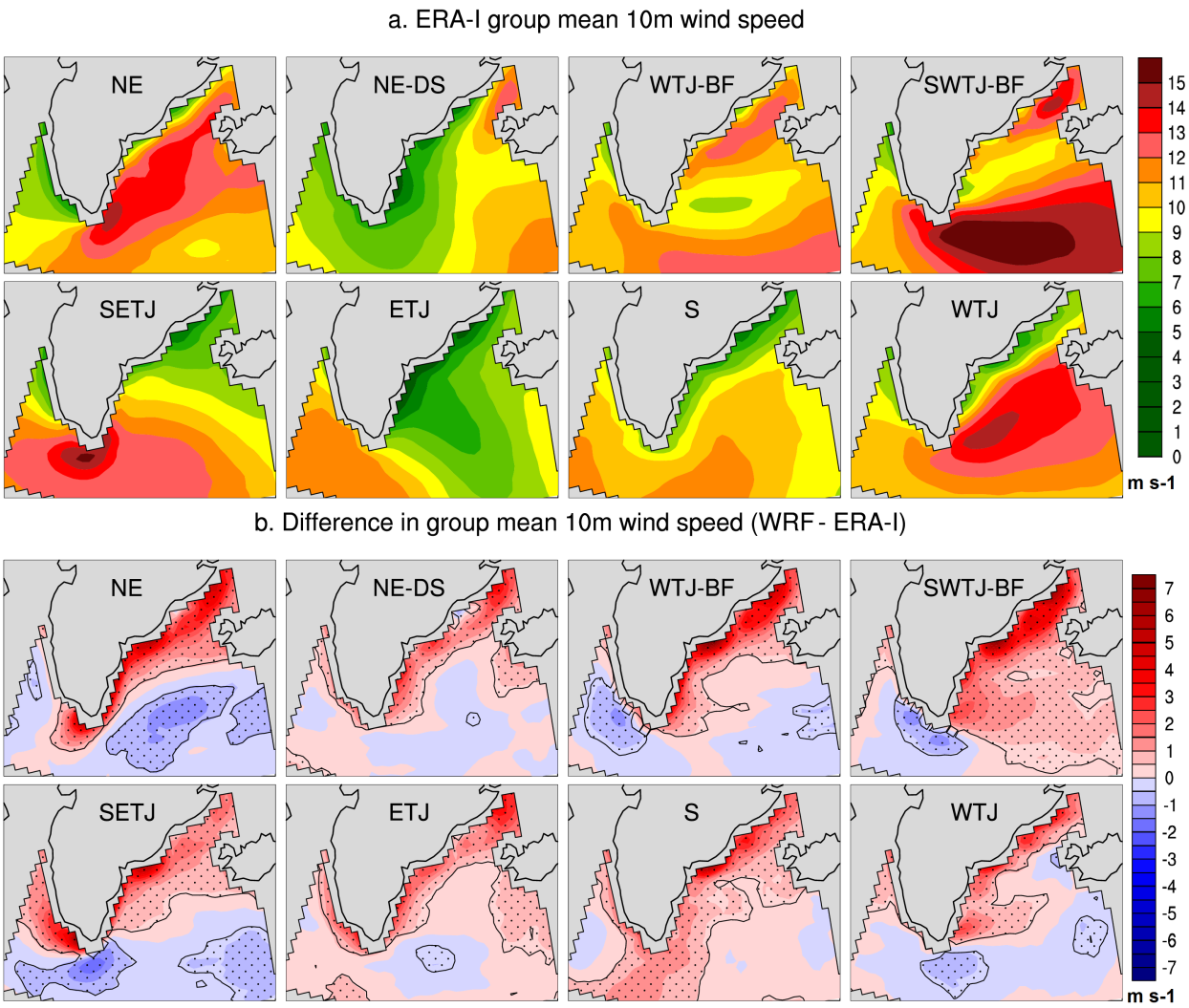

Figure 18: Mean 1997-2007 winter group wind speed (a) for ERA-I and (b) mean group wind speed difference (WRF-ERA). Stippling in Figure 18b indicates areas with statistically significant differences between the two datasets at the 95% confidence level.

For each SOM pattern, the percent contribution to the mean difference (Supplementary Figure 3) is equal to the sum of the frequency, intrapattern, and combined terms in Equation 7 for the points with mean wind speed difference that is both 95% significant and has a magnitude greater than 1 m s^{-1} (see Figure 16c). Positive percent contributions indicate that the SOM pattern contributes constructively to the mean difference while negative percent contributions indicate that the SOM pattern contributes destructively to the mean difference. The group percent

contribution to the mean difference, shown in Table 6, is the sum of the percent contributions for the patterns that map to each group, and most groups positively contribute to the mean difference. The NE, WTJ-BF, SWTJ-BF, and SETJ groups have the largest positive contributions to the mean difference, while the WTJ group has a negative contribution to the mean difference. Patterns along the edges of the SOM have the largest magnitude percent contributions to the mean difference while central, transitional patterns have a smaller impact.

	Group total term to mean difference	Group to total frequency term	Group to total intrapattern term	Group to total combined term
NE	24.2	198.6	8.8	5.8
NE-DS	0.9	-180.2	14.5	31.5
WTJ-BF	21.8	79.1	18.5	1.7
SWTJ-BF	28.0	198.5	16.5	-3.6
SETJ	31.6	277.8	10.9	-6.0
ETJ	2.0	-93.0	9.4	20.4
S	1.0	-122.7	11.5	8.7
WTJ	-9.4	-258.1	9.9	41.6

Table 6: SOM group percent (%) contributions to the mean wind speed difference (column 1), the total frequency term (column 2), the total intrapattern term (column 3), and the total combined term (column 4) The sum of the eight group percentages within a particular column is 100%.

The group total term (Figure 19a) is equal to the sum of the frequency, intrapattern, and combined terms (Equation 7) for the patterns in a particular group; the sum of the group total terms gives the mean difference shown in Figure 16c. Along the coast, the group total term is positive for NE, WTJ-BF, SWTJ-BF, and SETJ groups (Figure 19a), and these groups contribute the most to the mean difference (Table 6). Because the percent contribution is only calculated over points along the coast where the mean difference is both 95% significant and has a magnitude greater than 1 m s^{-1}, the coastal differences are reflected in these percent contributions but differences over the Irminger Sea are not.

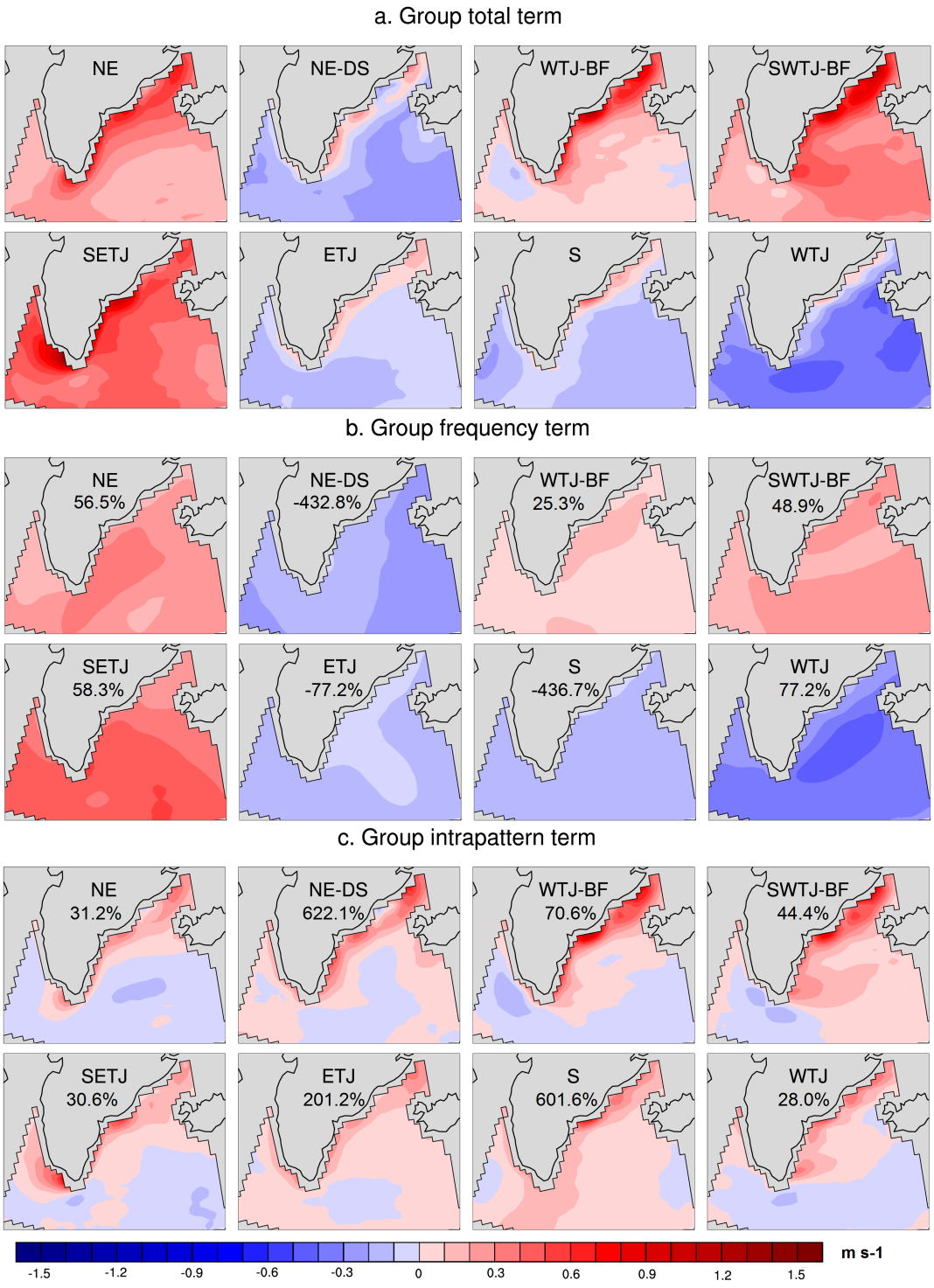

Figure 19: Group terms for wind speed difference calculation. The group total term (a) is a sum of the group frequency term (b), group intrapattern term (c), and group combined term (not shown). The percent (%) contribution of the group frequency term (b) and group intrapattern term (c) to the group total term (a) are listed below each group name. For a given group, the sum of the percent contribution from the group frequency (b), group intrapattern (c), and group combined percent contribution (not shown) is 100%.

To understand the importance of frequency and intrapattern differences for the groups, we compare the group frequency and intrapattern term (Figures 19b and 19c) and percent contributions to the group total terms; the combined term for each group is not shown because it is generally smaller than the frequency and intrapattern terms. The group frequency (intrapattern) term is the sum of the frequency (intrapattern) terms in Equation 7 over all patterns in the group. The group frequency terms are visually similar to the group total terms (Figures 19a and 19b), particularly over the Irminger Sea, while the intrapattern term contributes primarily to the group total term along the coast. Both the frequency and intrapattern differences are important for the individual group total terms, as can be seen by the frequency and intrapattern percent contributions to the group total term (percentages given on Figures 19b and 19c). However, the mean wind speed difference (Figure 16c) has the largest contribution from the total intrapattern term (85%) while the total frequency term contributes much less (12%) to the mean difference (Figure 16d).

If the frequency is important for explaining the differences in the group terms, why is it not important for the mean difference? The group frequency term sign is due to the group frequency difference (Figure 17a), and as a result, each group frequency term has either a large positive or negative percent contribution to the total frequency term (Table 6). While summing over the frequency terms to obtain the total frequency term, cancellation between patterns occurs and the resulting percent contribution of the total frequency term to the mean difference is relatively small. In contrast, the group intrapattern term reflects the stronger coastal winds in WRF across all wind patterns (Figure 18b), and each group has a positive percent contribution to the total intrapattern term (Table 6). Frequency differences are important for individual pattern or group contributions to the mean difference, but the coastal wind difference from all patterns

drives the mean difference. Therefore, the stronger WRF mean winds are due both to stronger coastal winds in each pattern and from patterns with strong coastal winds being simulated more frequently in WRF.

4. Discussion and Conclusions

This study uses the SOM training algorithm to investigate mesoscale wind patterns around the southeastern Greenland coast and variability between WRF and ERA-I over ten winters. The SOM analysis reveals the range in how these events are manifest. We find that the SOM results agree well with previous climatologies, but using a SOM also reveals that representations of similar patterns are not equally correlated with large-scale variability described by the sign of the NAO (Figure 17b). Therefore, using the NAO to predict ocean response to wind events may not be a robust indicator of air-sea interaction because the absence or presence of barrier flow is not well reflected in correlations with the NAO and the northerly barrier winds along the southeast Greenland coast may be important because the advection of cold, dry air in the northerly barrier wind may have an important impact on the ocean [*Våge et al.*, 2009; *Harden et al.*, 2011].

Additionally, this study finds that WRF has stronger winter mean coastal winds due to stronger coastal winds in each pattern (Figure 18b) and from patterns with strong coastal winds being simulated more frequently in WRF (Figure 17b). The mean difference is strongly impacted by a fundamental difference in how WRF and ERA-I simulate flow near topography, but over the Irminger Sea differences in wind speed between WRF and ERA-I varied for different types of patterns (Figure 18b).

The difference in horizontal resolution between ERA-I (150 km) and WRF (50 km) allows us to better understand how model resolution impacts mesoscale wind representation. In response to flow blocking, winds will adjust over the Rossby radius of deformation [*Holton*, 2004], which is ~750 km for barrier flow at 65°N that is approximately 1 km deep [*Petersen et al.*, 2009; *Renfrew et al.*, 2009b]. Based on their effective resolutions, WRF resolves features 350 km or larger [*Skamarock*, 2004] and ERA-I resolves features 600 km or larger [*Abdalla et al.*, 2013]. Therefore, while both datasets are able to resolve topographically driven wind features around southeastern Greenland, ERA-I is not likely able to resolve features smaller than the Rossby radius of deformation. The difference in effective resolution between WRF and ERA-I is likely responsible for WRF's stronger coastal winds for all types of wind events (Figure 18b) because WRF is able to better resolve small-scale modifications in pressure gradient that drive strong coastal barrier winds. The impact on wind speed due to model resolution is especially noticeable along the coast because the presence of sea ice means surface wind data from QuikSCAT are unavailable for ERA-I to assimilate. Over the Irminger Sea, where synoptic forcing dominates and ERA-I assimilates satellite wind data the WRF and ERA-I wind speeds are similar. While WRF is able to capture wind events along the coast, in areas like the Denmark Strait, which is constrained by steep terrain on two sides and is near the limit of features resolvable by WRF, using a higher resolution model with more realistic topography is expected to be important for resolving both strong barrier flow and weak winds in the lee of topography.

Because the SOM training algorithm uses the data from both datasets to determine the representative patterns, systematic differences between ERA-I and WRF are included in the SOM. If significant systematic differences exist that impact the low-level wind field, then ERA-I and WRF data would map to different patterns and occupy different portions of the SOM space.

Because data from both ERA-I and WRF mapped to all patterns in the SOM, this suggests that systematic differences between the models are small and the pattern differences in wind along the coast were the primary driver of differences between ERA-I and WRF. Systematic differences between the models are therefore expected to have minor impacts on the analysis, but differences in atmospheric boundary layer and surface layer parameterizations have been cited previously as a possible explanation for differences between reanalyses near-surface fields [*Renfrew et al.*, 2009a]. Because differences in wind speed are small over the open ocean away from the coast (Figure 16c), any systematic differences in surface layer parameterizations are likely related to treatment of sea ice roughness. However, because there are large differences in wind speed along the coast both over sea ice (Figure 16c, Denmark Strait) and regions without sea ice (Figure 17c, between Tasiilaq and Cape Farewell) it is likely that systematic differences in roughness are a small contributor to the difference in wind speed compared to the resolution and treatment of topography in each model. Data assimilation of satellite surface winds is another possible systematic difference in the models because ERA-I assimilates QuikSCAT wind speeds over the Irminger Sea. The assimilation of these winds could result in faster winds over the open ocean despite the smaller pressure gradient in ERA-I compared to WRF. However, along the coast where there is sea ice QuikSCAT data is unavailable, so the topographic influences on the pressure gradient and resulting wind speed are more important in this region. Using a reanalysis, even a modern one, does not guarantee good representation of coastal wind. Because the largest differences in wind speed occur along the coast and in regions where sea ice is likely to be present, correctly capturing winds and the corresponding atmospheric temperature and moisture properties is important for driving realistic air-sea fluxes in future reanalyses, coupled climate models, or stand-alone ice-ocean models.

5. Acknowledgments

This research was supported by the United States Department of Energy (DOE) grants DE-FG02-07ER64462 and DE-SC0006178, and a grant of computer time from the DOD High Performance Computing Modernization Program. Thanks to Mimi Hughes for managing the WRF simulations and providing helpful discussion for this paper. Thanks also to Melissa Nigro and Mark Seefeldt for their insight into SOMs and mesoscale winds that helped improve this analysis.

Chapter 4: Exploration of turbulent heat fluxes and wind stress curl in WRF and ERA-Interim during wintertime mesoscale wind events around southeastern Greenland

Abstract: The strong, mesoscale tip jets and barrier winds that occur off the coast of southeastern Greenland drive large surface turbulent heat fluxes that may impact deep ocean convection. The turbulent fluxes and wind stress curl associated with 10 m wind patterns identified using the self-organizing map (SOM) technique are investigated for ten winters (1997-2007, NDJFM) in the ECMWF Interim Reanalysis (ERA-I) and a regional simulation using the Weather Research and Forecasting (WRF) model at 50 km. Sensible heat flux differences between WRF and ERA-I are primarily due to differences in near-surface temperature, while latent heat flux differences are driven by both moisture and wind speed differences. The largest turbulent flux differences occur over the marginal ice zone where the fluxes in WRF are larger than in ERA-I due to specified sea ice thickness that influences the near-surface atmospheric temperature and moisture; WRF has larger magnitude wind stress curl over the Irminger Sea. Patterns of strong westerly tip jet with barrier flow are most likely to impact preconditioning and convection in the Irminger Sea compared to other manifestations of westerly tip jets, and easterly tip jets are expected to have localized ocean impacts south of Cape Farewell.

1. Introduction

Strong near-surface winds occur around the southeast Greenland coast and are co-located with a region where the downwelling component of the meridional overturning circulation occurs [*Bacon et al.*, 2003; *Pickart et al.*, 2003a; *Sproson et al.*, 2008; *Petersen and Renfrew*, 2009]. Open-ocean convection, or sinking of surface ocean water, is a localized process and only

occurs in a few locations worldwide where there is cyclonic ocean circulation [*Killworth*, 1983]. Cyclonic circulation preconditions the ocean by weakening vertical stability; subsequent heat loss or increase in salinity causes the water to become dense and sink [*Killworth*, 1983; *Marshall and Schott*, 1999]. The Irminger sea is a prime location for convection due to cyclonic circulation [*Pickart et al.*, 2003b; *Spall and Pickart*, 2003; *Våge et al.*, 2011b], and most years there is convection to 400 m depth and with particularly intense forcing convection can be deeper than 1 km [*Våge et al.*, 2008a, 2011b; *de Jong et al.*, 2012].

Mesoscale barrier winds, westerly tip jets, and easterly tip jets occur along the southeastern Greenland coast during winter. Three regions with wind maxima have been identified: the Denmark Strait, Tasiilaq, and Cape Farewell [*Moore*, 2003, 2012; *Moore and Renfrew*, 2005; *Harden et al.*, 2011]. During mesoscale wind events there are large vertical gradients in temperature and moisture between the cold, dry atmosphere and the comparatively warm ocean. As a result, large turbulent heat fluxes are possible during all types of wind events, and the large heat fluxes can cause surface water densification [*Renfrew et al.*, 2009a; *Harden et al.*, 2011; *Oltmanns et al.*, 2014]. Westerly tip jets were the initial focus for forcing ocean convection in the Irminger Sea [*Pickart et al.*, 2003a; *Våge et al.*, 2008a, 2008b, 2009], but other types of mesoscale winds may also be important for both preconditioning and convection in the Irminger Sea and southeast Labrador Sea [*Lavender et al.*, 2002; *Martin and Moore*, 2007; *Pickart et al.*, 2008; *Sproson et al.*, 2008; *Oltmanns et al.*, 2014]. Additional work can help uncover the potential effect of all types of wind events and to understand how short-lived mesoscale wind events impact the ocean on climatic time scales.

Because there are few atmospheric or oceanic data in the Arctic, models are an important tool for understanding air-sea interactions. However, many ice-ocean models have been designed

to use atmospheric forcing with low spatial and temporal resolution from global models or reanalyses [*Hunke and Holland*, 2007; *Lisæter et al.*, 2007; *Kwok et al.*, 2008; *Hunke*, 2010]. Low-resolution atmospheric models do not represent mesoscale winds around Greenland well, so we cannot be sure that the air-sea physical processes are represented correctly[*Kolstad*, 2008; *Haine et al.*, 2009; *Sproson et al.*, 2010; *DuVivier and Cassano*, 2013]. DuVivier and Cassano [2013] found that 10 km WRF simulations best capture the spatial and vertical structures observed during strong wind events around Greenland, but that 50 km was the minimum resolution for reasonably simulating strong wind events. Experiments with a 1D ocean model have shown that low-resolution atmospheric forcing requires a tip jet parameterization to replicate observed ocean mixed layer depths associated with convection [*Våge et al.*, 2008b], and a tip jet parameterization for ocean models has been developed [*Sproson et al.*, 2010]. However, explicitly representing the mesoscale winds with high-resolution models allows for distinguishing detailed differences between different types of wind events that are important for impacting physical air-sea processes.

In this study we examine differences in the surface turbulent heat fluxes and wind stress curl from two datasets during mesoscale wind events. A self-organizing map (SOM) was used to identify near-surface wind patterns around southeast Greenland from the ECMWF Interim Reanalysis (ERA-I) and a 50 km horizontal grid spacing simulation from the Weather Research and Forecasting (WRF) model. Identifying the differences in surface forcing by the various mesoscale wind events and from different datasets is important for understanding the modeled preconditioning and convection in the ocean. This paper will investigate how and why the surface turbulent fluxes differ between ERA-I and WRF for various manifestations of mesoscale wind patterns, and discussion of the mesoscale wind patterns in this manuscript is limited to

information relevant to surface fluxes, with a full exploration of the SOM wind patterns given in DuVivier and Cassano [2015]. In section 2, we explain the data and methods used in this study. The differences in atmospheric forcing between WRF and ERA-I are investigated in section 3. Section 4 explores which types of wind events are likely to have the largest oceanic impact and how these differ between WRF and ERA-I. Finally, section 5 discusses implications for the ocean from different wind patterns and differences in the datasets.

2. Data and Methods

a. WRF model simulations

This study uses the WRF model V3.2.1 [*Skamarock et al.*, 2008] at 50 km horizontal grid spacing for regional simulations over a pan-Arctic domain (Figure 20). The pan-Arctic domain was chosen so that multi-decadal atmospheric data can be used for forcing regional ice-ocean models that resolve the full circulation of the Arctic Ocean. For this study we will focus only on the wind patterns and surface fluxes located around the southeast Greenland coast.

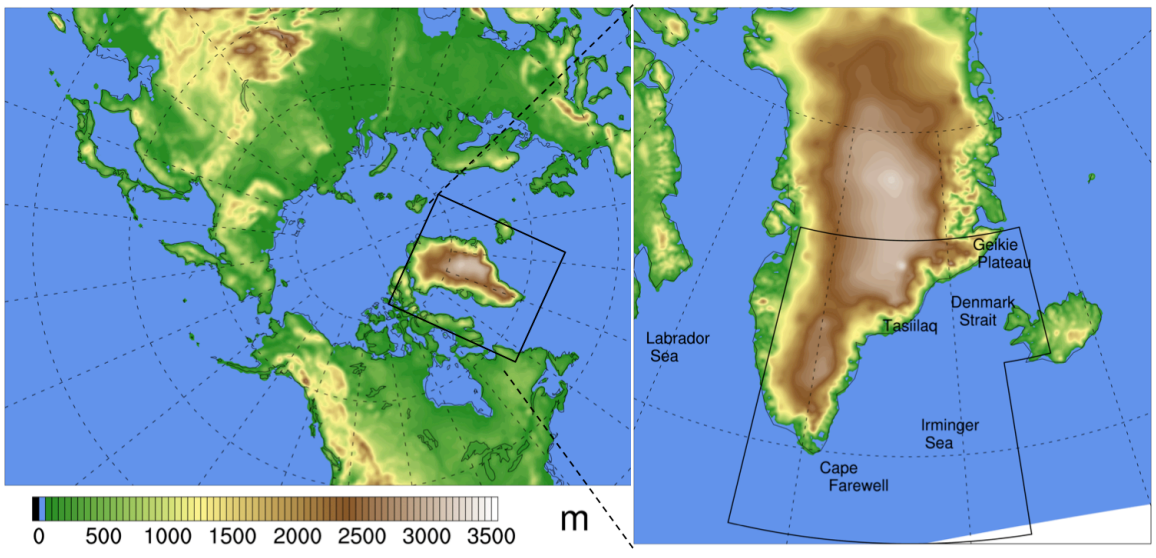

Figure 20: Map of pan-Arctic WRF domain showing the WRF terrain height (m), and inset of Greenland study region. The SOM training area is boxed in black.

The WRF simulation uses 40 vertical levels, and over the ocean there are 10 levels in the lowest 1 km. ERA-I provides the lateral and lower boundary conditions, and the sea ice fraction in WRF is specified from the National Snow and Ice Data Center (NSIDC) Bootstrap Sea Ice Concentration satellite product, which has a 0.25° x 0.25° resolution and daily temporal resolution [*Comiso*, 2008]. The physics parameterizations used are: the Goddard microphysics scheme [*Tao and Simpson*, 1993], the Grell 3D sub-grid scale convection scheme [*Grell and Dévényi*, 2002], CAM longwave and shortwave radiation [*Collins et al.*, 2004], Noah land surface model [*Chen and Dudhia*, 2001], and the YSU planetary boundary layer [*Hong et al.*, 2006] with MM5 similarity theory in the surface layer [*Dyer and Hicks*, 1970; *Paulson*, 1970; *Webb*, 1970].

WRF was run as a single continuous simulation from September 1, 1989 through January 1, 2008. To reduce synoptic scale biases in sea level pressure between WRF and ERA-I for the large domain and long simulation times, we spectrally nudged the top half of the WRF atmosphere towards ERA-I. Nudging constrains the upper-atmosphere, planetary wave scale features to be similar to ERA-I while also allowing the model to dynamically respond to changing surface conditions [*Cassano et al.*, 2011]. The difference in wintertime sea level pressure between ERA-I and WRF is small, and the mean sea level pressure field aligns well (not shown). Therefore, differences in the mesoscale wind representation and associated surface forcing are due not to differences in large-scale circulation but instead are due to differences in dataset physics, dynamics, or resolution.

b. ERA-Interim Reanalysis

ERA-I [*Dee et al.*, 2011] is a modern global reanalysis product that generally performs well in the Arctic. When compared with other reanalysis products, ERA-I best represents wind

events [*Lindsay et al.*, 2014], and it has been confirmed to reasonably represent strong wind events around Greenland observed during the Greenland Flow Distortion Experiment [*Renfrew et al.*, 2009a]. Because we are particularly interested in surface forcing during strong wind events, we have focused our analysis on ERA-I. ERA-I uses daily 0.5° x 0.5° sea ice data from NCEP and does not assimilate concentrations below 20% [*ECMWF*, 2007]. ERA-I data were interpolated from the 1.5° x 1.5° (150 km) resolution product to the WRF grid using the WRF pre-processing system so that direct comparisons could be made between datasets.

c. Wind pattern classification

This study uses a SOM of near-surface wind patterns around southeast Greenland and assesses the atmospheric state and surface fluxes associated with those wind patterns. The SOM training algorithm is an unsupervised, iterative process that identifies a user-specified number of patterns within a dataset [*Kohonen*, 2001; *Hewitson and Crane*, 2002; *Reusch et al.*, 2005]. Similar wind patterns are grouped together in a 2D spatial array, or map, of characteristic patterns, or nodes, that are determined objectively during training and comprise the SOM.

The SOM training algorithm uses wintertime (NDJFM) zonal and meridional near-surface wind data to correspond with months when strong mesoscale winds occur [*Moore*, 2003]. The winter training data for ERA-I and WRF data spanned ten winters (1997-2007); ERA-I analyses are available every 6 hours, and instantaneous WRF data are available every 3 hours, but only the 6 hourly data that correspond to the ERA-I data are used for analysis. In addition to the WRF and ERA-I data, two years of 10 km WRF data were used in the SOM training algorithm, but these will not be discussed in this paper to keep the focus of the comparison on ERA-I and WRF. SOM training used data at each time step, so both strong and weak wind patterns are considered when determining representative patterns. It is also necessary to use data

from all datasets of interest to train the SOM because then the full range of how wind patterns are represented is considered in the representative patterns. Focusing on ocean points along the southeastern Greenland coast allows the SOM to identify patterns based on mesoscale features over the ocean (Figure 20 inset, boxed region). During training, the grid must be identical for all data, so ERA-I and WRF data were interpolated to the 10 km WRF grid using a distance weighted average of the four nearest neighboring points. The SOM algorithm arranges similar patterns together into a two-dimensional array of the wind patterns present in the dataset, and it represents the total range and variability of winter wind patterns around Greenland (Figure 21).

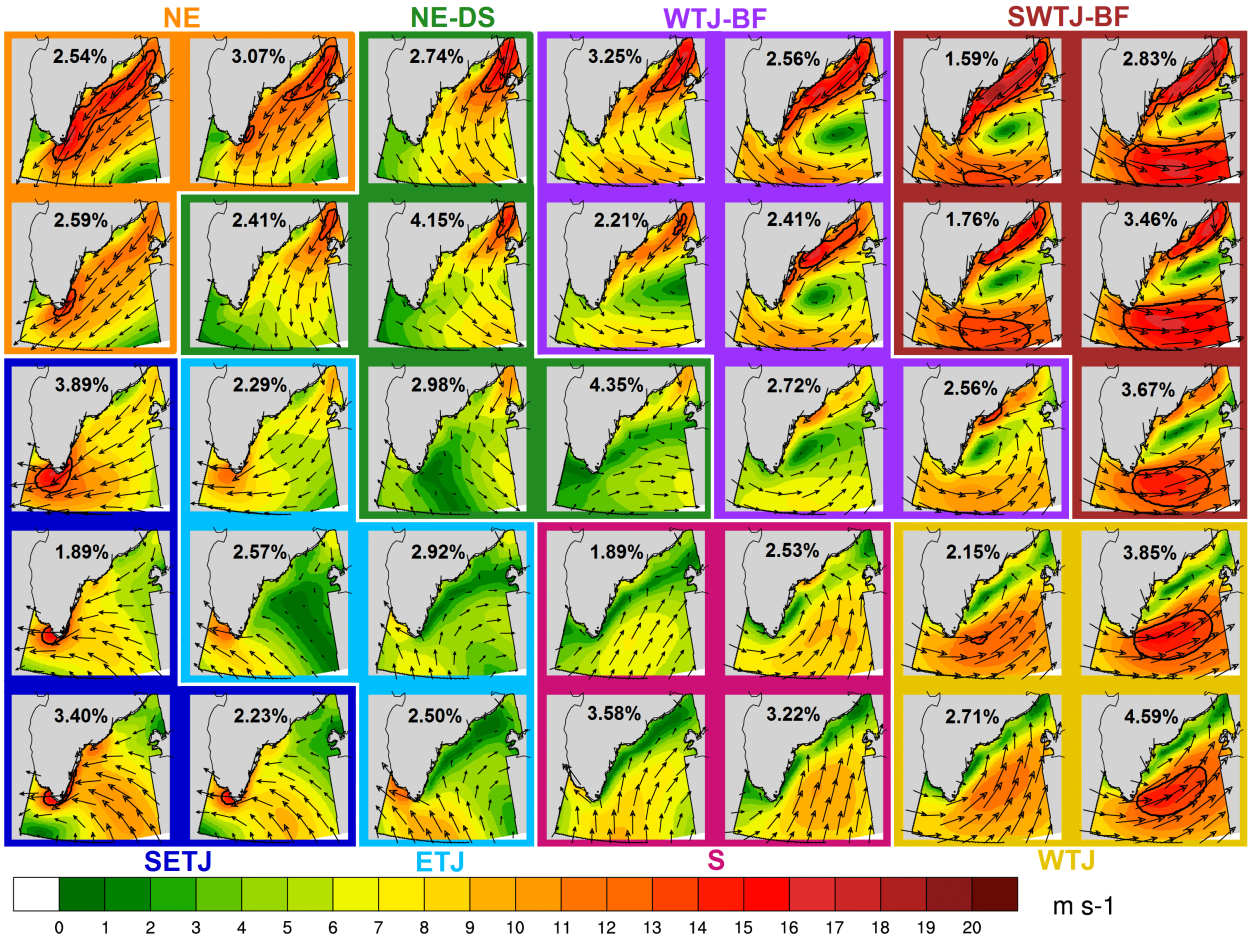

Figure 21: SOM of near-surface wind field with wind speed (m s^{-1}) shown by color shading. The dark black contour indicates "strong" winds that correspond to speeds greater than 13.8 m s^{-1}. The

colored lines around the patterns and labels at the top and bottom of the SOM indicate groupings described in the text The frequency of each pattern in the ERA-I data (1997-2007) is given as a percentage (%) and the percentage of each group is the sum of frequencies for all patterns in a particular group.

A number of SOM array sizes were investigated, and a 7x5 array was chosen because it represents the dominant wind patterns around southeast Greenland yet clearly exhibits variability between adjacent patterns. During SOM training, the ERA-I and WRF training dates are mapped to one of the 35 SOM patterns based on the minimum root mean square difference (RMSD) between that time's wind vectors and the wind vectors represented in the SOM patterns. The 7x5 SOM arrangement used for this work has an average RMSD of 2.61 m s^{-1} for all training samples.

In the SOM (Figure 21), patterns with barrier-parallel winds along the southeast coast are in the topmost rows of the SOM, and patterns with weak coastal winds are in the bottom rows. The left columns of the SOM have winds with an easterly component near Cape Farewell while the right columns have winds with a westerly component near Cape Farewell. The most extreme types of patterns are on the edges of the SOM while smoothed or transitional patterns are near the center. The four, objectively identified, corner patterns of the SOM correspond to the four sub-types of tip jets that were subjectively chosen in Moore [*Moore*, 2014] – northeasterly (SOM pattern 0,0), southeasterly (SOM pattern 0,4), northwesterly (SOM pattern 5,0), and southwesterly (SOM pattern 5,4) – but the SOM also shows a range in how these patterns are manifest.

To facilitate discussion of fluxes associated with particular types of wind patterns, we have subdivided the SOM into groups of similar patterns (colored outlines in Figure 21). These groupings were defined subjectively and are based on physical similarity of winds in adjacent patterns, RMSD of the wind vectors between adjacent patterns, and a threshold value for "strong"

winds of 13.8 m s^{-1} ("near gale" on the Beaufort Sea Scale) shown by the solid black contour in Figure 21. The patterns were grouped into the following categories and are identified by the colored outlines in Figure 21: northeasterly flow (NE, orange); northeasterly flow in the Denmark Strait (NE-DS, green); westerly tip jet with barrier flow (WTJ-BF, purple); strong westerly tip jet with barrier flow (SWTJ-BF, red); strong easterly tip jet (SETJ, dark blue); easterly tip jet (ETJ, light blue); southerly flow (S, magenta); westerly tip jet without barrier flow (WTJ, yellow). For the remainder of the paper we will reference these groups when comparing the surface fluxes and atmospheric state associated with particular types of wind patterns.

The pattern average value and standard deviation of atmospheric variables (i.e. wind speed, 2 m temperature, etc.) for a dataset is calculated using all the times from that dataset that map to a particular pattern. To determine if pattern averages from two datasets are statistically different at the 95% significance level, we use the student's t-test. The t-test is performed at each grid point and uses the average and variance calculated over all individual events. The frequency with which a pattern is simulated is found as the ratio of the number of times in a dataset that map to a particular pattern relative to the total number of time periods in that dataset. The ERA-I frequency for each pattern is shown on Figure 21, and a detailed discussion of pattern frequencies for both ERA-I and WRF can be found in DuVivier and Cassano [2015]. Group averages, standard deviations, and frequencies are found using the same methods as for the individual patterns, but use all times that map to patterns within a particular group.

For a given dataset, the winter mean for any atmospheric variable at each grid point can be calculated two equivalent ways. The first method uses each time over a period of interest and averages all the times from the dataset (ERA-I or WRF). The student's t-test is then used to determine which grid points in the two datasets have a statistically significant difference. The

second method for calculating a winter mean uses the pattern frequencies and pattern average variables that are results from the SOM training, and combines them using Equation 8:

$$X_{mean} = \sum_{n=1}^{N} f_n X_n \quad (8)$$

where n represents a single pattern in the SOM, f_n is that pattern's frequency, and X_n is that pattern's mean for variable X. The sum over all SOM patterns, 35 patterns for the SOM in this study, gives the mean of the variable of interest over all times of interest. This second method provides additional insight into the particular SOM pattern details that determine the overall mean state.

d. COARE flux algorithm

Forecast flux products are available for ERA-I and WRF but are not used in this study, and instead the temperature, moisture, pressure, and winds from the ERA-I analyses and WRF forecasts are used for offline turbulent flux calculations with a common algorithm. Using the same turbulent flux algorithm for all datasets ensures that differences in fluxes between the datasets is due only to differences in the atmospheric state and not to differences in the WRF and ERA-I surface flux parameterizations (such as stability calculations) and allows us to assess the relative importance of temperature, moisture, and wind speed on the surface fluxes. An atmospheric model boundary layer parameterization has internally consistent wind, temperature, and moisture values that are used for calculating fluxes. Using near-surface data calculated using one algorithm to calculate fluxes using another turbulent flux algorithm will not be fully consistent and will introduce some errors in the fluxes calculated. Unfortunately, because of the non-linearity of bulk flux algorithms, there is not a good way to estimate the error associated with calculating fluxes using near-surface data that were not produced within the same boundary

layer parameterization as the near surface variables. However, ocean-ice models calculate turbulent fluxes using an internal surface parameterization that uses near-surface atmospheric state information, sometimes from multiple sources [*Large and Yeager*, 2009]. Therefore, it is scientifically relevant to understand how hybrid surface input into a flux algorithm impact the turbulent surface fluxes.

We use COARE V3.0 [*Fairall et al.*, 1996, 2003] to calculate fluxes because its turbulent sensible and latent heat fluxes and wind stress compare better with observations than other flux parameterizations [*Brunke et al.*, 2003]. COARE performs well at high wind speeds, though it has not been tested for the stronger wind speeds observed around southeastern Greenland. The COARE algorithm uses the 10 m wind speed, surface pressure, 2 m temperature (T2m), 2 m mixing ratio (q2m), and sea surface temperature (SST) for latent and sensible heat flux and wind stress calculations. ERA-I provides lower boundary conditions for WRF, so the SST is identical in both datasets, and for grid cells with partial sea ice coverage we use an SST no colder than -1.8°C, the freezing point of salt water. Because we are interested in forcing related to ocean convection and preconditioning, COARE fluxes are applied only to the fraction of a grid cell with open water in the marginal ice zone (MIZ), which is defined to have sea ice concentrations between 15% and 80% [*Strong and Rigor*, 2013]; open ocean refers to any grid point with sea ice concentrations less than 15%. In figures, cells with ice concentration greater than 80% have been masked and there is a bold contour indicating 15% sea ice concentration; therefore, the MIZ is the region located between this bold contour and the coastline. It is important to consider both sensible and latent heat fluxes because each influences the ocean differently: the latent heat flux represents not only oceanic energy loss, but also an increase in salinity associated with evaporation of fresh water.

We found that COARE fluxes calculated with ERA-I data were larger than the ERA-I forecast fluxes (not shown). The magnitude of WRF fluxes calculated using COARE was smaller than those calculated using the internal WRF YSU surface parameterization (not shown). Compared to aircraft based turbulent flux observations during case study events, DuVivier and Cassano [2013] found that the WRF-calculated turbulent heat fluxes are too high in this region, so the smaller magnitude of the WRF COARE fluxes is more comparable with observations. We calculate the wind stress curl using four-point centered finite differences in the wind stress zonal and meridional components at each time. Evaluating the wind stress curl is important because positive wind stress curl drives upwelling that shoals the thermocline and preconditions the surface ocean water for convection [*Marshall and Schott*, 1999; *Pickart et al.*, 2008], and negative wind stress curl is important north of Iceland for separation of the East Greenland Current [*Våge et al.*, 2013].

We found that for both WRF and ERA-I the magnitude of radiative forcing is smaller than turbulent heat forcing at the ocean's surface, and this agrees with previous studies that have shown that the shortwave and longwave contributions to the total surface forcing are much smaller than turbulent forcing [*Marshall and Schott*, 1999; *Petersen and Renfrew*, 2009]. To perform a complete surface energy budget these terms would be important, particularly for spring and fall seasons when the shortwave component increases in magnitude. However, this paper will focus on differences in the turbulent heat fluxes and future work will address the impact of all fluxes in fully coupled simulations.

3. Mean atmospheric surface forcing

a. Comparison of turbulent fluxes and wind stress curl

The mean WRF and ERA-I turbulent heat fluxes and wind stress curl are shown in Figure 22. The total turbulent heat flux is the sum of the latent and sensible heat fluxes. In WRF and ERA-I, over most the open ocean, the atmosphere gains more than 100 W m^{-2} due to turbulent heat fluxes (Figures 22a and 22b). Over the Irminger Sea WRF has smaller total fluxes than ERA-I by 30-50 W m^{-2} (Figure 22c), but the largest differences occur over the MIZ where WRF fluxes are 300 W m^{-2} greater than those in ERA-I. The differences in total turbulent heat fluxes over the open ocean and MIZ are a result of differences in the sensible and latent heat fluxes in each of these regions.

The WRF mean sensible heat flux is much larger over the MIZ than the Irminger Sea (Figure 22d), but ERA-I has similar sensible heat fluxes across the whole domain (Figure 22e). However, the WRF mean latent heat flux is similar in the MIZ and Irminger Sea (Figure 22g), while ERA-I has larger latent heat fluxes over the open ocean when compared to the MIZ (Figure 22h). Along the southeastern coast and over the MIZ, the difference in total flux is driven primarily by larger WRF sensible heat fluxes (more than 200 W m^{-2} greater than ERA-I, Figure 22f) and secondarily by larger WRF latent heat fluxes (70 W m^{-2}, Figure 22i). However, over the open ocean the latent heat flux is the dominant contribution to the total turbulent flux for both ERA-I and WRF, but larger ERA-I sensible heat fluxes (20 W m^{-2}, Figure 22f) and latent heat fluxes (20 W m^{-2}, Figure 22i) contribute similarly to the difference in total turbulent heat flux.

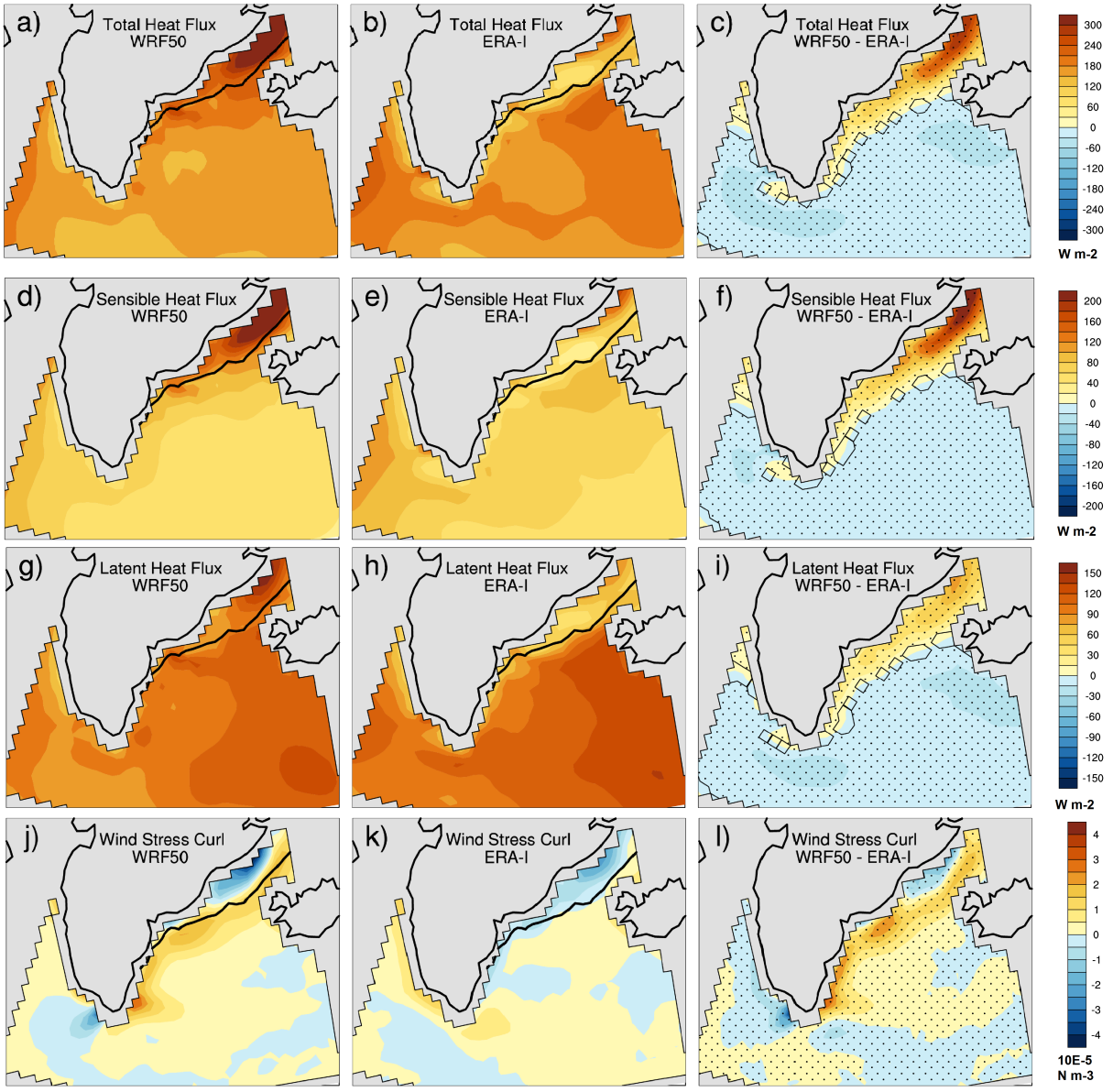

Figure 22: Mean 1997-2007 (a) WRF and (b) ERA-I winter total turbulent heat flux (W m^{-2}) and (c) difference with ERA-I. Mean (d) WRF and (e) ERA-I sensible heat flux (W m^{-2}) and (f) difference with ERA-I. Mean (g) WRF and (h) ERA-I latent heat flux (W m^{-2}) and (j) difference with ERA-I. Mean (j) WRF and (k) ERA-I wind stress curl (10^{-5} N m^{-3}) and (l) difference with ERA-I. The dark black contour on the mean figures is the 15% sea ice concentration line. Stippling on the difference figures indicates areas with statistically significant difference between the two datasets at the 95% confidence level.

Positive wind stress curl over the Irminger Sea contributes to the cyclonic ocean circulation that preconditions the ocean for convection. The mean WRF wind stress curl is positive over most the Irminger Sea (Figure 22j), and while the ERA-I spatial pattern of wind stress curl is similar to WRF (Figure 22k), the magnitude is 2-3 times larger for WRF (Figure 22l). The reasons for the differences in turbulent fluxes and wind stress curl between WRF and ERA-I will be explored in sections 3b and 3c.

b. Impact of surface state on representative turbulent fluxes

Winter mean fluxes are calculated using Equation 8, but two methods can be used to calculate pattern mean fluxes. The first method averages the COARE flux values for each time period that map to a specific pattern; fluxes calculated using this method are referred to as mean fluxes. The second method uses the pattern average atmospheric state as input to the COARE flux algorithm to calculate fluxes for a particular pattern; the fluxes calculated using this method are called representative fluxes in this paper. Using representative fluxes allows us to untangle how variations in the atmospheric state between the datasets impact turbulent fluxes. By exchanging pattern average variables – temperature, moisture, or wind speed – from ERA-I when calculating WRF fluxes, we can evaluate which atmospheric variables contribute the most to the difference in representative fluxes between datasets. Because the patterns from two datasets on the same day do not necessarily map to the same SOM pattern, exchanging the variables at each time would not ensure that we are examining differences in how the atmospheric state associated with particular patterns impacts the difference in fluxes. Therefore, using a representative flux is necessary for this analysis because it ensures that we are comparing the atmospheric state between datasets for the same type of pattern.

As described in section 2c, using near-surface data from different datasets will introduce errors in the fluxes calculated. However, the recommended forcing data for ice-ocean models uses hybrid near-surface forcing from multiple datasets [*Large and Yeager*, 2009; *Griffies et al.*, 2012], so it is important to understand how differences in the atmospheric state impact the turbulent fluxes. We compare the mean and representative winter fluxes for each dataset to understand how the method of flux calculation impacts the winter fluxes. The difference between the mean fluxes and representative fluxes for both WRF and ERA-I is small (less than 20 W m^{-2} - not shown) relative to the total sensible and latent heat flux magnitudes in this region. The representative flux has a comparable spatial pattern to the mean flux with maxima and minima occurring in the same locations with similar magnitude. Because the mean and representative fluxes are similar, the difference in the mean flux for two datasets is similar to the difference in representative flux for those datasets. The difference in WRF and ERA-I mean sensible (Figure 22f) and latent (Figure 22i) heat flux is similar to the difference in the representative sensible (Figure 23a) and latent (Figure 23d) heat flux. In each case, the same pattern of differences in the datasets exists over the MIZ and Irminger Sea, and the magnitude of the differences is similar. The largest difference in WRF and ERA-I mean sensible (Figure 23a) and latent (Figure 23d) heat fluxes are in the MIZ where WRF has larger fluxes than ERA-I, and in both cases WRF has smaller fluxes southwest of Iceland. Therefore, the effect of temperature, moisture, and wind speed on the representative fluxes is expected to mirror the impact on the mean fluxes, and thus only the representative fluxes will be discussed further in section 3b.

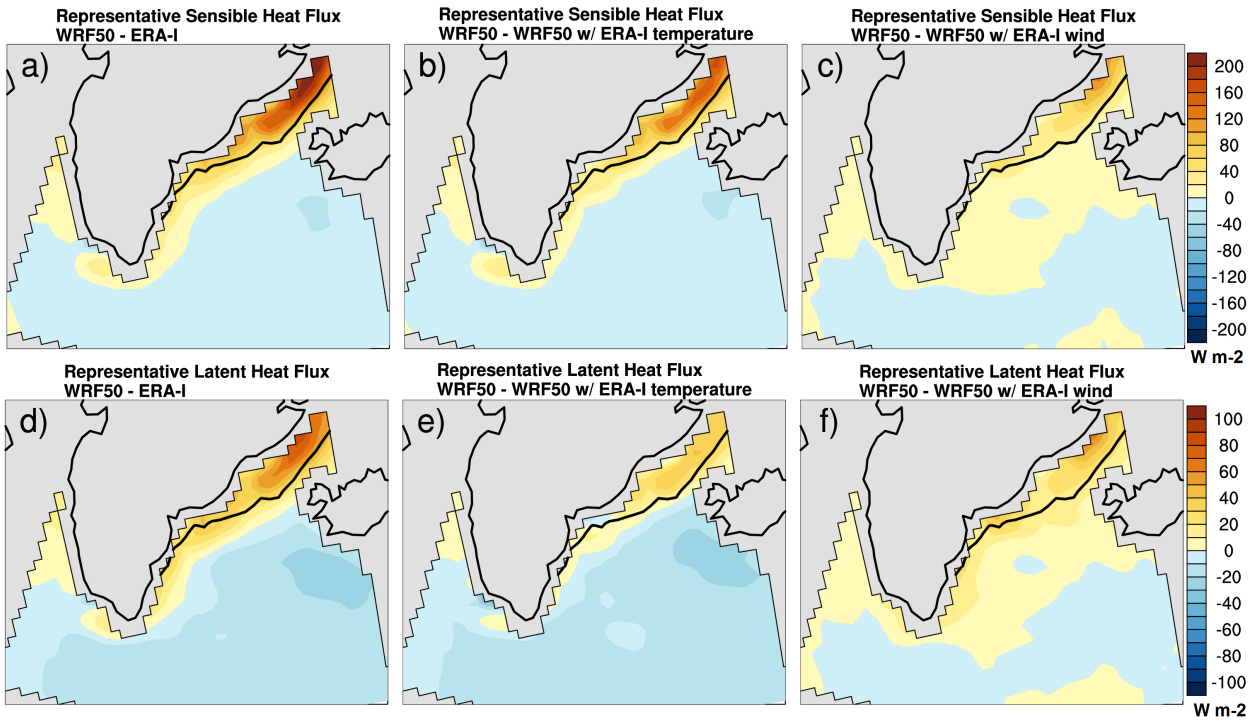

Figure 23: Difference in winter mean sensible heat flux (W m^{-2}) between (a) WRF and ERA-I, (b) WRF and sensible heat flux calculated with WRF inputs but using ERA-I temperature, and (c) WRF and sensible heat flux calculated with WRF inputs but using ERA-I wind speed. Difference in mean latent heat flux (W m^{-2}) between (d) WRF and ERA-I, (e) WRF and latent heat flux calculated with WRF inputs but using ERA-I mixing ratio, and (f) WRF and latent heat flux calculated with WRF inputs but using ERA-I wind speed. The dark black contour on the mean figures is the 15% sea ice concentration line.

Exchanging data from two datasets works in the following manner: to determine the impact of differences in temperature on the difference in sensible heat flux for WRF and ERA-I, we use ERA-I pattern average temperature instead of WRF pattern average temperature in the COARE algorithm while the other flux inputs (wind speed, etc.) from WRF are unchanged. Then by comparing the representative sensible heat flux difference between WRF and ERA-I (Figure 23a) and the representative sensible heat flux difference between WRF and WRF using ERA-I temperatures (Figure 23b) we can ascertain how much of the representative flux difference between WRF and ERA-I is due to the difference in temperature between the two datasets. A

similar procedure can be done to evaluate the impact of wind speed and moisture differences on the difference in representative fluxes for the two datasets.

For sensible heat flux, calculating fluxes with the WRF temperatures instead of ERA-I temperatures results in larger fluxes in the MIZ (Figure 23b), and using WRF wind speed instead of ERA-I wind speed also results in larger fluxes in the MIZ (Figure 23c). The magnitudes of the difference in flux due to temperature are larger than the differences due to wind speed, so sensible heat flux differences are primarily driven by the difference in temperature and wind speed differences contribute constructively along the coast. In the Irminger Sea the temperature differences drive the flux differences between WRF and ERA-I.

For latent heat flux, using the WRF mixing ratio instead of the ERA-I mixing ratio produces larger fluxes in the MIZ and smaller fluxes southwest of Iceland (23e); using WRF wind speeds instead of ERA-I wind speeds results in larger fluxes, particularly along the coast (Figure 23f). Along the coast the difference in fluxes (Figure 23d) is due to a comparable, and constructive, combination of mixing ratio and wind speed differences. However, over the Irminger Sea the difference in flux due to differences in mixing ratio dominates the flux difference between WRF and ERA-I.

c. Mean atmospheric state differences

Because the sensible and latent heat flux and wind stress curl vary due to differences in near surface atmospheric state between WRF and ERA-I, it is necessary to explore the reason for differences in the datasets. The strongest mean winds in WRF occur as barrier flow along the coast (Figure 24a) while the fastest ERA-I winds occur over the southern Irminger Sea (Figure 24b), and WRF barrier flow is faster than ERA-I by up to 5 m s^{-1} (Figure 24c). The difference in

wind speed is due to WRF better resolving Greenland's topography and the resulting mesoscale barrier winds [*DuVivier and Cassano*, 2015]. The stronger WRF wind speeds drive both stronger mean sensible and latent heat fluxes (Figures 23c and 23f), and this effect is largest along the coast where the wind speeds vary most between the datasets; in the open ocean where differences in speed are small there is little impact on the fluxes. Additionally, the stronger WRF winds result in larger magnitude curl, both positive and negative, when compared to ERA-I (Figure 22l). The larger magnitude positive wind stress curl indicates that an ocean model forced with WRF may lead to more oceanic preconditioning in the Irminger Sea [*Marshall and Schott*, 1999; *Pickart et al.*, 2008], while the larger magnitude negative wind stress curl north of Iceland would have a larger impact on the separation of the East Greenland Current [*Våge et al.*, 2013].

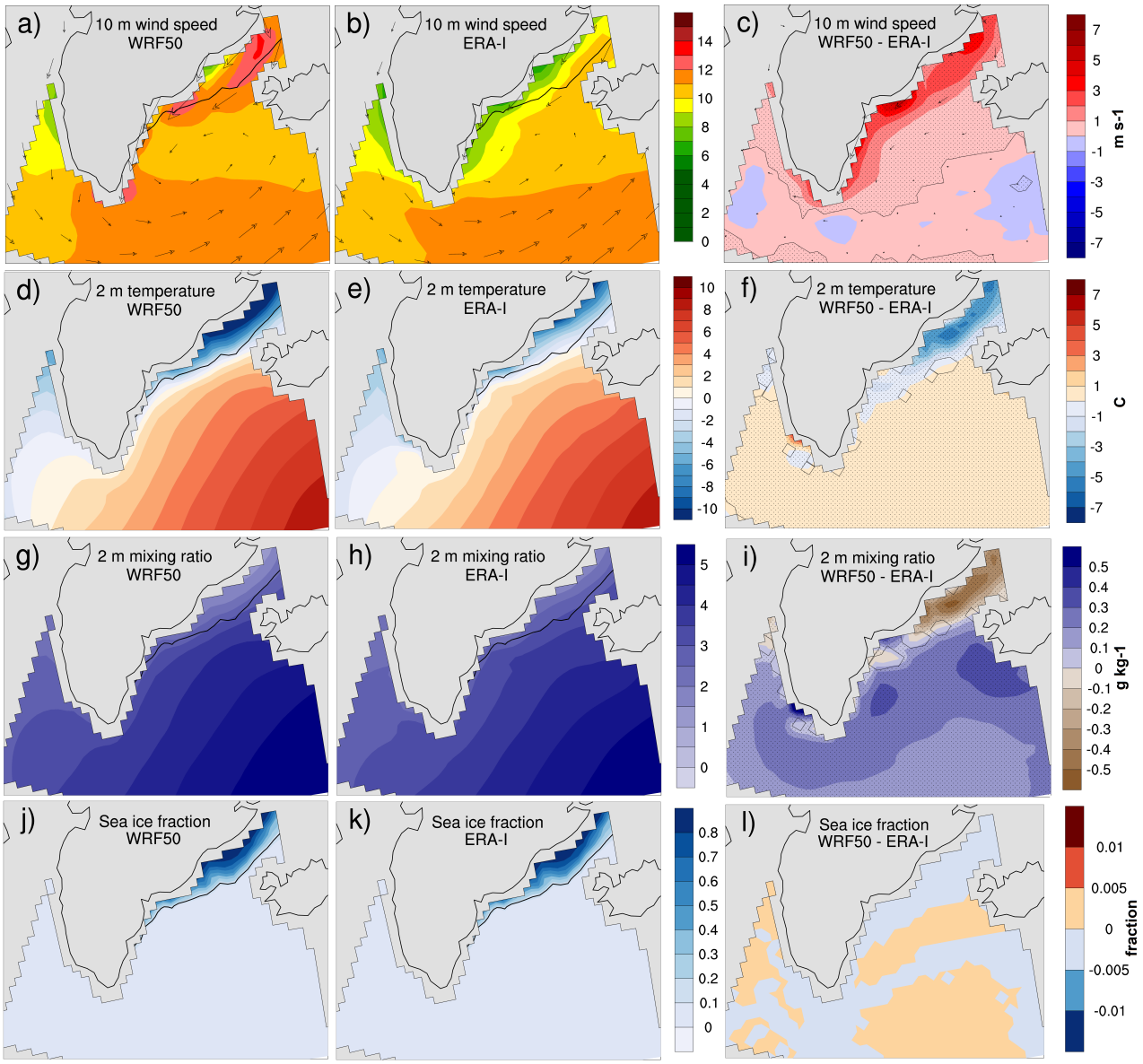

Figure 24: Mean 1997-2007 winter wind speed (m s^{-1}) with vectors to indicate the wind circulation for (a) WRF and (b) ERA-I and difference in wind speed and wind vectors for (c) WRF and ERA-I. Mean 2 m temperature (°C) for (d) WRF and (e) ERA-I and difference for (f) WRF and ERA-I. Mean 2 m mixing ratio (g kg^{-1}) for (g) WRF and (h) ERA-I and difference for (i) WRF and ERA-I. Mean sea ice concentration (%) for (j) WRF and (k) ERA-I and difference for (l) WRF and ERA-I. The dark black contour on the mean figures is the 15% sea ice concentration line. Stippling on the difference figures indicates areas with statistically significant difference between the two datasets at the 95% confidence level.

Both along the coast and in the open ocean, the difference in near-surface temperature and mixing ratio are important drivers for the difference in mean fluxes. T2m is less than SST everywhere, which results in an upward sensible heat flux, and because the SST is identical for WRF and ERA-I (not shown) it is differences in T2m and q2m that drive sensible and latent heat flux differences. The coldest T2m are adjacent to the Greenland coast, and temperatures increase to the southeast of Greenland where the northern branch of the Gulf Stream would be located (Figure 24d and 24e). The driest air is co-located with the coldest air while moister air is located in the southeast portion of the domain (Figures 24g and 24h).

WRF has colder T2m than ERA-I by up to 5°C in the MIZ, but over the open ocean WRF is up to 1°C warmer than ERA-I (Figure 24f). Because the surface temperatures are the same, the colder WRF T2m values over the MIZ lead to a larger vertical temperature gradient that drives larger sensible heat fluxes in WRF; the opposite situation occurs over the Irminger Sea where the warmer WRF T2m results in a smaller gradient and smaller sensible heat fluxes. Where WRF is colder than ERA-I it is also drier by up to 1 g kg^{-1}, and where WRF is warmer than ERA-I it is around 0.3 g kg^{-1} moister (Figure 24i). Therefore, in the MIZ WRF has a larger vertical moisture gradient due to the drier q2m and the result is larger latent heat fluxes; the reverse is true over the Irminger Sea.

The large differences in near-surface atmospheric state over in the MIZ are likely related to differences in the model's treatment of sea ice. NSIDC provides the WRF sea ice fraction (Figure 24j), but the difference in sea ice fraction between WRF and ERA-I is small (less than 0.001, Figure 24l). Therefore, the large difference in T2m over the MIZ is likely due to differences in the specified sea ice thickness used in WRF and ERA-I. WRF specifies 3 m thick sea ice [*Hines et al.*, 2015] while ERA-I specifies 1.5 m thick sea ice [*ECMWF*, 2007]. Even

though the sea ice fraction is the same, WRF has colder T2m because the thicker WRF sea ice does not allow as much upward energy from the ocean to heat the atmosphere. WRF also has colder T2m over most the Greenland Ice Sheet compared to ERA-I (not shown), so differences in radiation parameterization and the surface energy budget may also cause WRF to be colder than ERA-I over the MIZ. However, the temperature difference over the ice sheet is much smaller than over sea ice (not shown), so any radiative effects on near surface temperatures are likely secondary to the effect of sea ice thickness.

Even though the SST is identical (not shown), in open ocean conditions WRF has warmer T2m than ERA-I (Figure 24f). Operational ECMWF analyses in the Labrador Sea, which has similar conditions to the Irminger Sea, are known to have a near surface cold bias [*Renfrew et al.*, 2002] and this tendency may be present in the ERA-I data. Differences in T2m between WRF and ERA-I over the open ocean may be related to differences in boundary layer depth and mixing. For a given upward energy flux, boundary layer parameterizations will calculate near-surface temperature based on how the incoming energy is distributed across the depth of the boundary layer. Small differences in boundary layer mixing or depth will impact the resulting T2m. Unfortunately boundary layer depth is not well observed and not easily comparable between the datasets, but these differences are likely the source of the differences in T2m between the WRF and ERA-I datasets.

4. Group Surface Forcing

The mean surface turbulent heat fluxes and wind stress curl (Figure 22) indicate how the datasets differ over an entire winter, but differences in surface forcing for particular wind patterns are not discernable. To understand how and why particular wind patterns can influence

the ocean we examine the group mean turbulent heat fluxes and wind stress curl using the SOM groups shown in Figure 21.

a. Patterns with strongest forcing

The total turbulent heat flux and wind stress curl for each group can be used to determine the potential each type of pattern has for forcing the ocean. Westerly tip jets (Figure 25a- WTJ-BF, SWTJ-BF, and WTJ) have previously been identified as the most likely driver of ocean convection in the Irminger Sea [*Pickart et al.*, 2003a; *Våge et al.*, 2008a, 2008b, 2009]. Of all groups, SWTJ-BF has the largest total turbulent heat fluxes (greater than 400 W m^{-2} both in the MIZ and over the Irminger Sea) and they occur over the largest spatial area (Figure 25b). However, WTJ-BF have large turbulent fluxes in the MIZ while WTJ have large turbulent fluxes over the Irminger Sea, and the difference in the location of flux maxima is the result of the presence or absence of barrier flow. Both WTJ-BF and SWTJ-BF have large positive wind stress curl along the ice edge and over the Irminger Sea, but WTJ have positive wind stress curl only in the vicinity of the jet but negative wind stress curl just outside of the MIZ (Figure 25c).

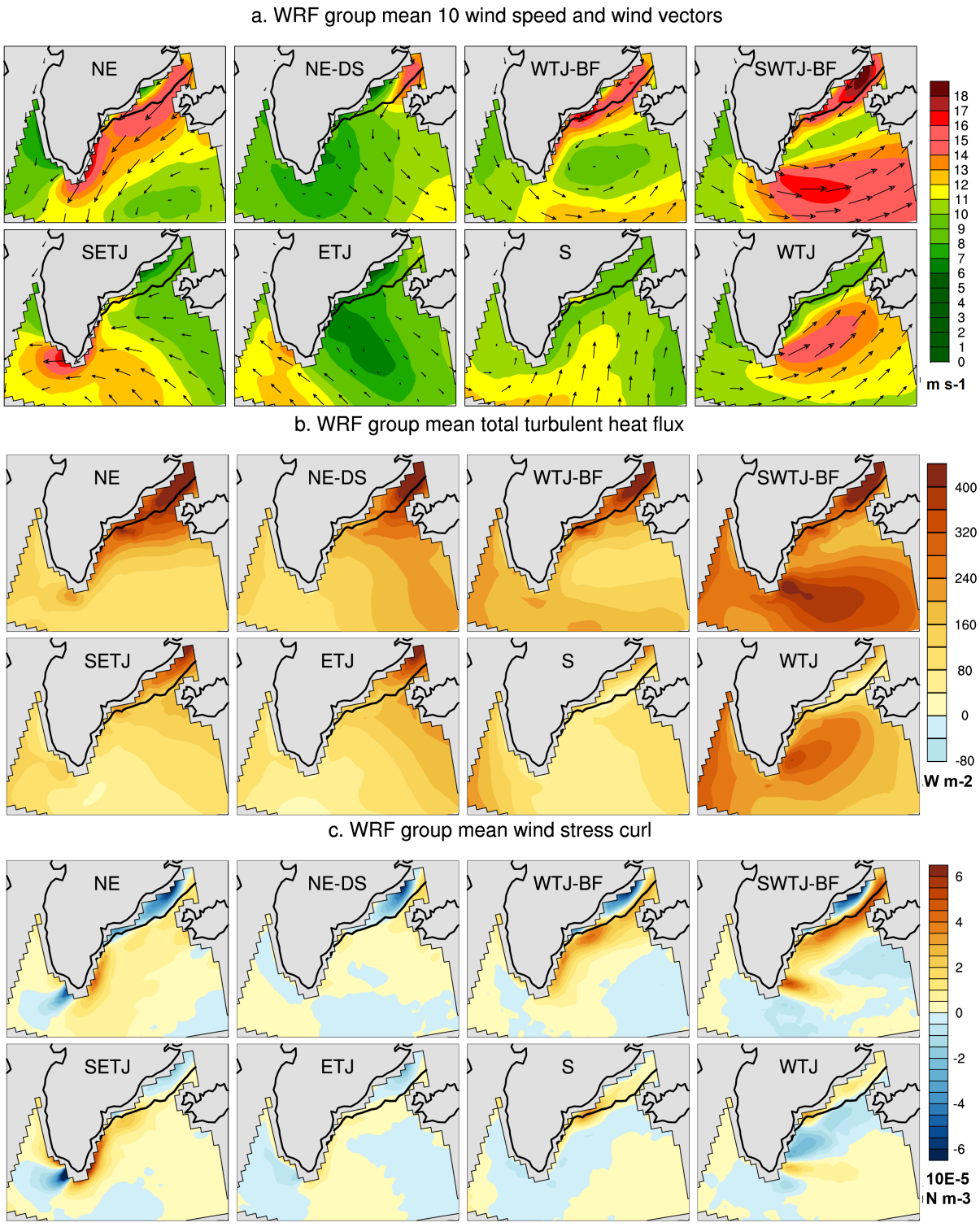

Figure 25: WRF 1997-2007 group average (a) 10 m wind speed (m s^{-1}) with vectors to indicate the wind circulation for each group, (b) total turbulent heat flux (W m^{-2}), and (c) wind stress curl (10^{-5} N m^{-3}). The dark black contour on the mean figures is the 15% sea ice concentration line.

The influence of easterly tip jets on convection, particularly in the southeast Labrador Sea, is not yet well known [*Martin and Moore*, 2007; *Pickart et al.*, 2008; *Sproson et al.*, 2008]. SETJ have a local flux maxima to the west of Cape Farewell, but the wind stress curl in this region is negative (Figures 25b and 25c). However, the NE pattern has both elevated turbulent heat fluxes along the coast and south of Cape Farewell where there is positive wind stress curl.

The Irminger Sea and the sea southwest of Cape Farewell are regions that have been identified previously as locations where convection has been observed or is likely to occur [*Pickart et al.*, 2003b; *Våge et al.*, 2008a; *de Jong et al.*, 2012], and these locations are impacted by westerly and easterly tip jets. Because similar wind patterns have different surface forcing and the atmospheric forcing is one component of the complex process of open-ocean convection, we cannot generalize from the atmosphere alone whether or not convection or preconditioning for convection will occur for a particular type of wind pattern. While this study addresses the relative surface forcing due to turbulent fluxes and wind stress curl, it is impossible to fully unravel the relative forcing from each wind pattern on ocean preconditioning and convection without an ice-ocean model. However, by examining turbulent surface fluxes and wind stress curl, the patterns that may have the largest impacts become clearer.

Overall, SWTJ-BF have the greatest potential for causing ocean convection or preconditioning over much of the Irminger Sea due to large turbulent heat fluxes and positive wind stress curl, but impacts from WTJ-BF and WTJ will vary based on local turbulent flux maxima. Localized convection south of Cape Farewell may be possible depending on the precise location of the maximum fluxes due to SETJ, but NE patterns may have a larger impact on the ocean off the east coast of far southern Greenland because there is strong, northerly barrier-parallel flow that drives large turbulent heat fluxes. In order to focus on the patterns identified as

having the greatest surface forcing, the following sections will explore the differences between WRF and ERA-I for: NE, WTJ-BF, SWTJ-BF, SETJ, and WTJ. Comparisons between WRF and ERA-I for all eight patterns can be found in Supplementary Figures 4, 5, and 6.

b. Wind stress curl

NE and SETJ patterns have strong positive (negative) wind stress curl on the eastern (western) side of Cape that is driven by the strong northeasterly jet at Cape Farewell. SWTJ-BF and WTJ-BF have the greatest positive wind stress curl that occur over the largest area (Figures 25c and 26a), while WTJ have much weaker positive wind stress curl over the ocean and it occurs over a smaller spatial area. WRF has stronger wind stress curl than ERA-I along the ice edge for all groups (Figure 26b), which is likely due to WRF's stronger barrier winds which have larger wind speed gradients over the width of the jet (Figure 26c). For NE and SETJ, WRF also has greater magnitude wind stress curl than ERA-I in the vicinity of Cape Farewell, so the ocean response to wind events in this region may be different if forced by WRF or ERA-I.

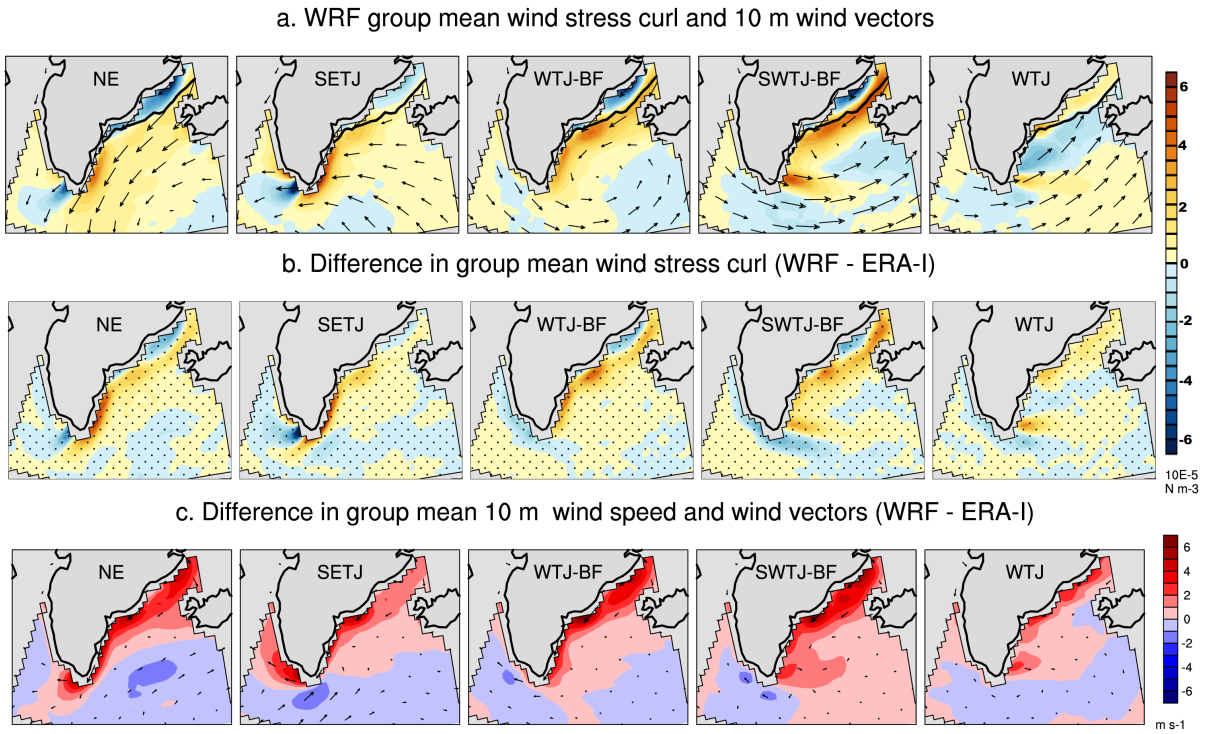

Figure 26: Group (a) WRF wind stress curl (10^{-5} N m^{-3}) with vectors to indicate the wind circulation for each group, (b) difference in WRF and ERA-I wind stress curl, and (c) WRF and ERA-I 10 m wind speed (m s^{-1}) and wind vector difference. The dark black contour on the mean figures is the 15% sea ice concentration line. Stippling on the difference figures indicates areas with statistically significant difference between the two datasets at the 95% confidence level.

c. Sensible heat flux

There are elevated upward sensible heat fluxes in the MIZ for all groups except SETJ and WTJ, and this reflects the lack of barrier flow in these patterns (Figure 27a). The presence of large sensible heat fluxes over the open ocean varies by group; SWTJ-BF has the largest fluxes over the Irminger Sea that are co-located with the westerly tip jet, while NE has the largest fluxes parallel to the sea ice edge and also co-located with the barrier flow. In the MIZ WRF has larger sensible heat fluxes than ERA-I by 200 W m^{-2} for all groups (Figure 27b), but in the Irminger Sea WRF has smaller fluxes than ERA-I.

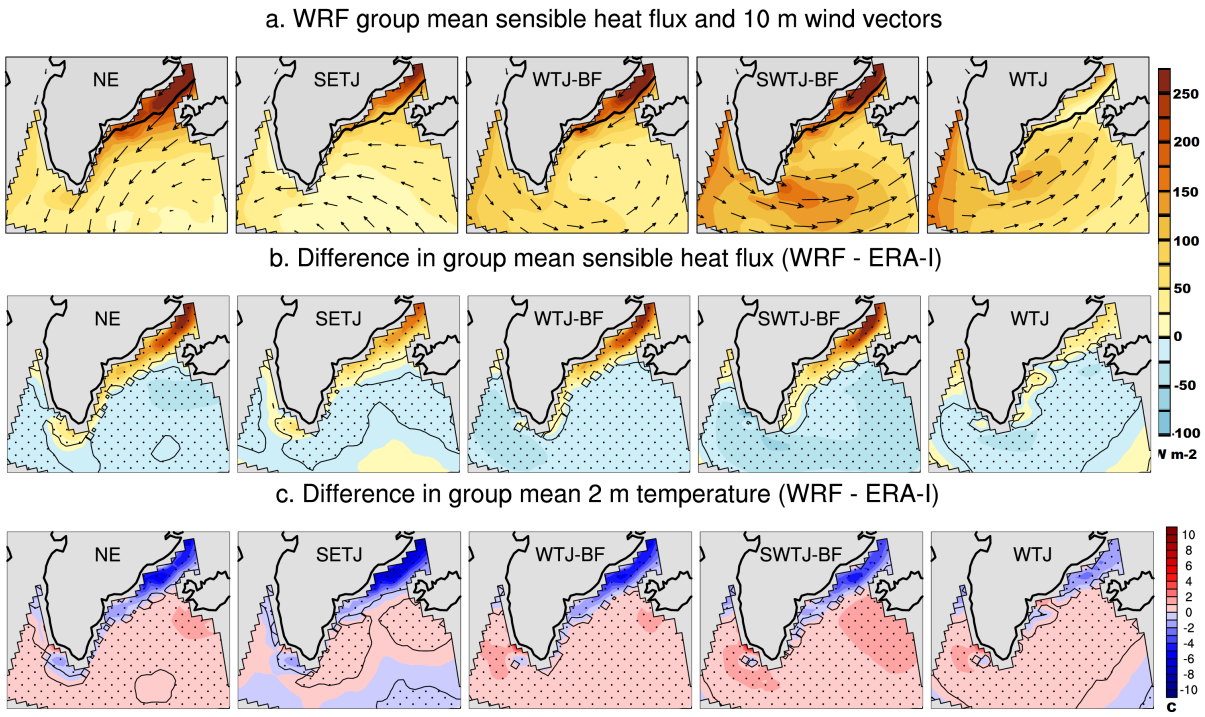

Figure 27: Group (a) WRF sensible heat flux (W m^{-2}) with vectors to indicate the wind circulation for each group, (b) difference in WRF and ERA-I sensible heat flux, and (c) WRF and ERA-I 2 m temperature difference (°C). The dark black contour on the mean figures is the 15% sea ice concentration line. Stippling on the difference figures indicates areas with statistically significant difference between the two datasets at the 95% confidence level.

The group average SST and sea ice concentrations are nearly identical between groups (not shown), but over the MIZ WRF has colder T2m than ERA-I (Figure 27c). As discussed previously, the difference in T2m is due primarily to thicker sea ice in WRF. Over the open ocean WRF is 1-2 K warmer southwest of Iceland for all groups. The spatial pattern of sensible heat flux difference (Figure 27b) mirrors the T2m group differences (Figure 27c) more than the group wind speed difference (Figure 26c). This suggests that the T2m differences between WRF and ERA-I dominate the group differences in sensible heat flux, and wind differences (Figure 26c) add constructively to the principal impact from T2m differences.

d. Latent heat flux

The largest NE latent heat fluxes co-located with barrier flow and parallel to the MIZ, while SWTJ-BF and WTJ have elevated fluxes in the Irminger Sea in the vicinity of the strongest westerly tip jet winds (Figure 28a). When compared to ERA-I, WRF tends to have larger latent heat fluxes in the MIZ and smaller latent heat fluxes over the open ocean (Figure 28b). However, SWTJ-BF and WTJ have larger WRF latent heat fluxes over the Irminger Sea as well as the MIZ. The sensible heat flux group differences are primarily driven by T2m group differences, but the spatial pattern of latent heat flux differences (Figure 28b) is a combination of the mixing ratio difference (Figure 28c) and wind speed difference (Figure 26c). In particular, the wind speed difference tends to be important around Cape Farewell for determining the spatial differences in latent heat flux, and this is particularly noticeable for SWTJ-BF and WTJ.

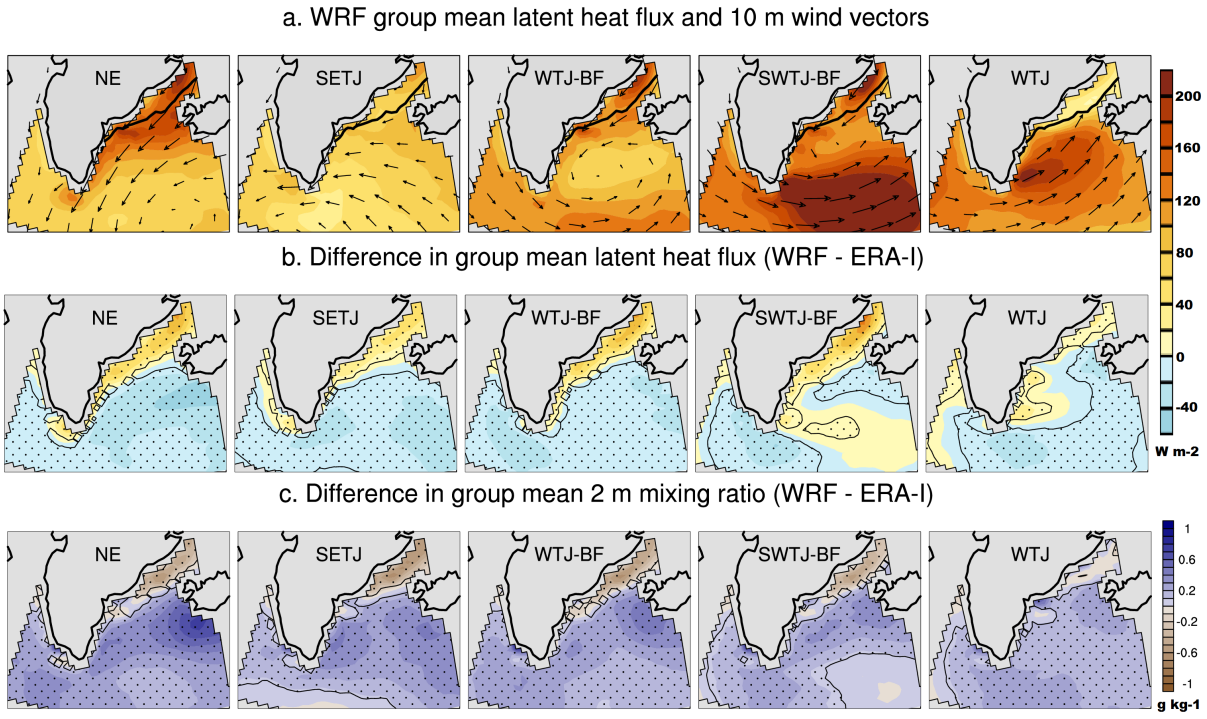

Figure 28: Group (a) WRF latent heat flux (W m^{-2}) with vectors to indicate the wind circulation for each group, (b) difference in WRF and ERA-I latent heat flux, and (c) WRF and ERA-I 2 m mixing ratio difference (g kg^{-1}). The dark black contour on the mean figures is the 15% sea ice concentration line. Stippling on the difference figures indicates areas with statistically significant difference between the two datasets at the 95% confidence level.

5. Discussion and Conclusions

On average, throughout the winter the ocean loses around 150 W m^{-2} due to turbulent heat fluxes over the Irminger Sea (Figures 22a and 22b), but differences between ERA-I and WRF in the total turbulent flux are largest in the MIZ (Figure 22c). Because large gradients in temperature and moisture between the atmosphere and ocean exist in the MIZ, the large, localized transfer of energy from the ocean to the atmosphere is an important influence on the near-surface atmospheric state, and could be important to the development of passing cyclones. Additionally, the MIZ is a dynamically active region for sea ice, so it is important to accurately represent ice transport by jets [*Heorton et al.*, 2014] and energy transfer that can impact sea ice growth or melt. While open-ocean convection does not occur in the MIZ, the processes and energy transfer in this region may be important for preconditioning the ocean or modifying the ocean surface salinity or temperature in ways that would impact the density, and therefore convection. Compared to ERA-I, WRF has larger sensible and latent heat fluxes in the MIZ, but over the open ocean the differences are relatively small and WRF has smaller turbulent fluxes (Figures 22d and 22f). Differences in sensible heat flux (Figure 22f) are primarily driven by the difference in T2m, while the differences in latent heat flux (Figure 22i) are the result of a combination of q2m and wind speed differences. The WRF near-surface air is particularly cold and dry over the MIZ, so for regions of open ocean within the MIZ there are large temperature and moisture gradients between the cold, dry air and the comparatively warm surface water that result in large sensible and latent heat fluxes.

Previous work reinforces that near-surface temperature and mixing ratio, particularly near the ice edge where large fluxes occur, are important for driving fluxes [*Marshall and Schott*, 1999; *Petersen and Renfrew*, 2009; *Renfrew et al.*, 2009a; *Harden et al.*, 2011; *DuVivier and*

Cassano, 2013]. We find that the near-surface atmospheric state strongly depends on the specification of sea ice thickness. Observations along the southeast Greenland coast indicate that sea ice is less than 1 m thick [*Bourke and Garrett*, 1987], but WRF specifies 3 m thick sea ice [*Hines et al.*, 2015] while ERA-I specifies 1.5 m thick sea ice [*ECMWF*, 2007], neither of which is reasonable for this region.

Models using a constant ice thickness based off of observations taken before the 2000's may not be appropriate for accurate turbulent fluxes over sea ice in the MIZ, and possibly in the central Arctic because the Arctic ice regime has shifted toward younger, thinner ice dominating the basin [*Serreze et al.*, 2007; *Haas et al.*, 2008; *Zhang et al.*, 2008; *Stroeve et al.*, 2011]. This is a consideration that should be taken into account when evaluating energy exchange in regional climate models or reanalyses data (such as ERA-I or the newer Arctic System Reanalysis) that use specified sea ice thickness. New versions of WRF will address the concerns with constant sea ice thickness by using multiple thickness categories [*Hines et al.*, 2015], but coupled models with active atmosphere-ice-ocean are best suited for modeling turbulent exchanges in a region of dynamic sea ice.

Additionally, this work identifies which wind patterns are most likely to strongly impact the ocean. SWTJ-BF are the most likely type of wind pattern to impact open-ocean convection because this pattern has the largest turbulent heat fluxes that are co-located with strong positive wind stress curl (Figure 25). WTJ-BF and WTJ are less likely to influence open-ocean convection due to less favorable magnitudes and location of fluxes with respect to the largest positive wind stress curl. In particular, WTJ have weak wind stress curl due to the lack of barrier flow, and therefore may have smaller impact on preconditioning the ocean than other types of westerly tip jets. NE is most likely to impact open-ocean convection near Cape Farewell than

SETJ or ETJ. While the exact forcing from easterly tip jets on the ocean remains unknown, ocean response would be localized and dependent on the details of each specific wind event. Using an ice-ocean model with atmospheric forcing from different types of wind events would help unravel details of how the ocean responds to different wind events and the relative importance of preconditioning by the different events, but the use of a fully coupled atmosphere – ice – ocean model would provide the most rigorous way to assess the atmosphere – ocean coupling discussed in this paper.

6. Acknowledgements

This research was supported by the United States Department of Energy (DOE) grants DE-FG02-07ER64462 and DE-SC0006178, and a grant of computer time from the DOD High Performance Computing Modernization Program. Thanks also to Mimi Hughes for managing the WRF simulations, and to both Mimi and Melissa Nigro for their discussion of fluxes, SOMs, and mesoscale winds that helped improve this analysis. Three anonymous reviewers' comments have also helped improve this manuscript. Data are available free of charge from the authors and can be obtained by contacting the corresponding author: alice.duvivier@colorado.edu.

Chapter 5: Atmospheric forcing and oceanic response during strong wind events around southeastern Greenland as modeled over 20 winters in the Regional Arctic System Model (RASM)

Abstract: Strong, mesoscale tip jets and barrier winds that occur along the southeast Greenland coast have the potential for impacting deep convection in the Irminger Sea. The self-organizing map (SOM) training algorithm was used to identify 12 wind patterns that represent the range of wind regimes present during twenty winters (1990-2010, NDJFM) in the fully coupled Regional Arctic System Model (RASM). For all wind patterns the ocean loses buoyancy, primarily through the turbulent sensible and latent heat flux thermal terms; haline contributions to buoyancy loss were found to be insignificant compared to the thermal contributions. Patterns with westerly winds at Cape Farewell had the largest buoyancy loss over the Irminger and Labrador Seas due to large turbulent fluxes from strong winds and the advection of anomalously cold, dry air over the warmer ocean. Patterns with easterly flow at Cape Farewell have large buoyancy loss along the sea ice edge in the Denmark Strait and a secondary, local maximum immediately west of Cape Farewell. The ocean mixed layer is anomalously deep for with wind patterns that have northerly flow with either easterly or westerly winds at Cape Farewell; mixed layer deepening is positively correlated to the frequency of those patterns and of greater magnitude for longer duration events.

1. Introduction

Wintertime synoptic storms interact with the steep topography along Greenland's southeast coast and generate mesoscale tip jets [*Doyle and Shapiro*, 1999; *Moore*, 2003, 2012, 2014; *Våge et al.*, 2009] and barrier winds [*Moore and Renfrew*, 2005; *Harden et al.*, 2011].

During these strong wind events, the combination of fast winds and large temperature and moisture gradients between the cold, dry air and the relatively warmer ocean surface drive oceanic energy and buoyancy loss [*Petersen and Renfrew*, 2009; *Renfrew et al.*, 2009a; *Harden et al.*, 2011; *DuVivier and Cassano*, 2013; *Oltmanns et al.*, 2014]. Open-ocean convection, or sinking of surface ocean water, is a localized process and only occurs in a few locations worldwide where there is cyclonic ocean circulation [*Killworth*, 1983]. Cyclonic circulation preconditions the ocean by weakening vertical stability; subsequent heat loss or increase in salinity causes the water to become dense and sink [*Killworth*, 1983; *Marshall and Schott*, 1999].

The Labrador Sea has cyclonic circulation and is a well-known area of convection and deep water formation [*Clarke and Gascard*, 1983; *Gascard and Clarke*, 1983; *Marshall and Schott*, 1999], but convection in the Irminger Sea is being actively investigated. The Irminger Sea has cyclonic circulation driven by positive wind stress curl from the strong mesoscale wind events that take place there over the winter [*Pickart et al.*, 2003a; *Spall and Pickart*, 2003; *Våge et al.*, 2011a], and convection has been observed to depths of 400-1000 m [*Bacon et al.*, 2003; *Våge et al.*, 2008a, 2011a; *de Jong et al.*, 2012]. Due to the strong positive wind stress curl associated with westerly tip jets, these types of mesoscale features have been a focus of investigation for forcing ocean convection [*Pickart et al.*, 2003a; *Spall and Pickart*, 2003; *Våge et al.*, 2008b, 2009, 2011a]. However, other types of mesoscale winds may also be important for both preconditioning and convection in the Irminger Sea and southeast Labrador Sea [*Lavender et al.*, 2002; *Martin and Moore*, 2007; *Pickart et al.*, 2008; *Sproson et al.*, 2008; *Oltmanns et al.*, 2014].

To date, ocean model studies of convection in the seas around Greenland have used simplified models, been of short duration, and limited in geographical domain. An idealized

regional ocean model study shows convection is possible during westerly tip jets [*Pickart et al.*, 2003a], and a simple 1D ocean model requires a tip jet parameterization to replicate observed ocean mixed layer depths [*Våge et al.*, 2008b]. A one-month case study shows the modeled ocean response to barrier wind events depends on the resolution of atmospheric forcing data [*Haine et al.*, 2009], and using high resolution atmospheric forcing can increase the Atlantic meridional overturning circulation [*Jung et al.*, 2014]. These results suggest that mesoscale wind events are crucial for forcing modeled ocean convection, but mesoscale winds around Greenland are not accurately represented in global scale atmospheric models [*Kolstad*, 2008; *Sproson et al.*, 2010]. As a result, parameterizations of strong mesoscale winds have been developed for use with low resolution atmospheric forcing [*Våge et al.*, 2008b; *Sproson et al.*, 2010; *Condron and Renfrew*, 2013]. However, explicit representation of mesoscale winds is required for realistic physical processes and air-sea interactions during a strong wind event. Explicitly simulating mesoscale winds requires high-resolution regional atmospheric models [*DuVivier and Cassano*, 2013; *Shkolnik and Efimov*, 2013; *Tilinina et al.*, 2014] with 50 km resolution or higher to capture the steep terrain gradients necessary to realistically block air flow and drive strong wind events [*DuVivier and Cassano*, 2013].

In this study, we use the method of self-organizing maps (SOM) to identify 12 near-surface wind patterns around southeast Greenland that represent the range of wind regimes present during twenty winters (NDJFM, 1990-2010) simulated by the fully coupled Regional Arctic System Model (RASM). By using a high-resolution, fully coupled model in which the atmosphere, ice, and ocean evolve together with realistic air-sea interactions, we can explore the ocean response to a large number of different wind events. We examine the thermodynamic ocean buoyancy forcing and response of the ocean mixed layer depth (MLD) for the 12 wind

patterns. The paper is organized as follows: the RASM data, SOM pattern classification method, and buoyancy flux calculation are explained in section 2. In section 3, we explore the contributions to the buoyancy flux for each wind pattern, and in section 4 we address the ocean MLD response to wind patterns and address the importance of wind event duration for changes in the MLD. Section 5 discusses implications of this study and future directions for exploration.

2. Data and Methods

a. RASM

RASM is a fully coupled atmosphere-ocean-ice-land limited area model designed for use on a pan-Arctic domain (Figure 29a). This description of the RASM configuration will cover only details relevant to this study, and additional details can be found in Roberts and Coauthors (2015). RASM is comprised of the Weather Research and Forecasting (WRF) model, Los Alamos National Laboratory Parallel Ocean Program (POP) and Sea Ice Model (CICE), Variable Infiltration Capacity (VIC) land hydrology model, and exchanges surface fluxes every 20 minutes using the same flux coupler as the Community Earth System Model (CESM) Version 1.1 [*Craig et al.*, 2012] with modifications in RASM for improved ice-ocean dynamics [*Roberts et al.*, 2015]. The pan-Arctic domain encompasses the Arctic System, as defined by Roberts et al. [2010], and extends to the North Pacific and North Atlantic oceans to account for passage of cyclones into the Arctic. WRF and VIC share a 50 km polar stereographic grid, while POP and CICE share a 1/12° (~9 km) rotated sphere grid with the equator passing through the North Pole.

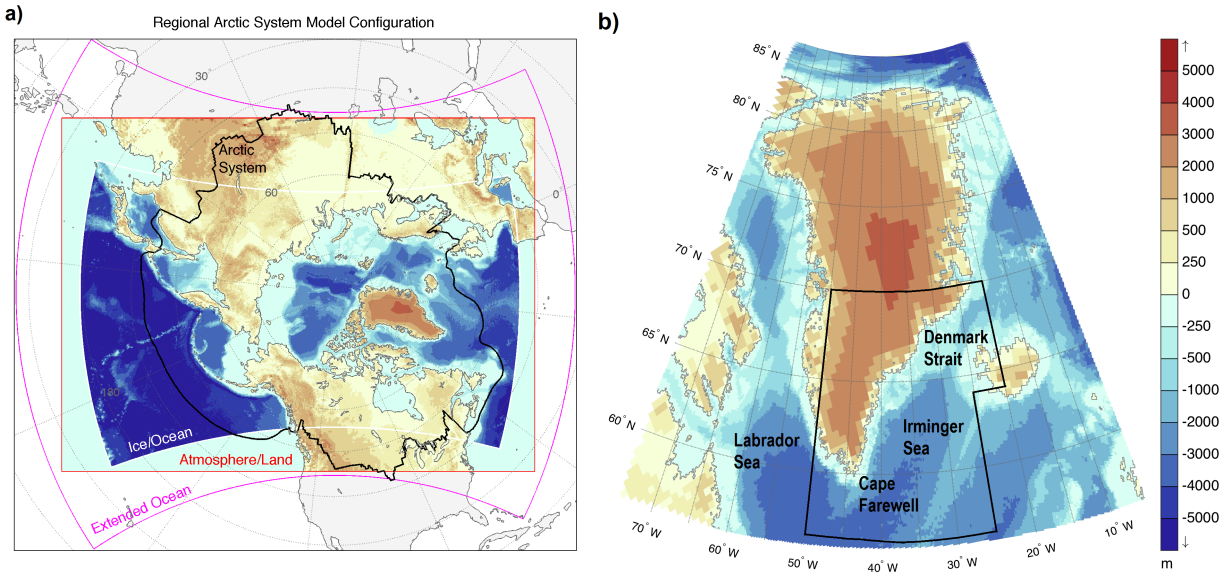

Figure 29: (a) Map of terrain height and bathymetry (m) for the pan-Arctic RASM domain with boundaries of the 50 km atmosphere/land domain (red), boundaries of the ~9 km ice/ocean domain (dark blue and bathymetry), boundaries of the ~9 km extended ocean domain (magenta), and boundaries of the Arctic System as defined in Roberts et al. (2010) (black). (b) Terrain height and bathymetry (m) for the Greenland focus region with the SOM training area is boxed in black.

RASM uses a modified version of WRF V3.2.1 [*Skamarock et al.*, 2008] that allows for coupling to the surface models. The MM5 Similarity Theory surface layer scheme [*Dyer and Hicks*, 1970; *Paulson*, 1970; *Webb*, 1970] has been modified to use surface roughness, friction velocity, latent heat flux, and sensible heat flux passed from the coupler; surface stability is determined by inverting the surface fluxes and using the roughness length and this, along with the turbulent fluxes is then passed to the WRF boundary layer parameterization (YSU PBL parameterization, [*Hong et al.*, 2006]). RASM uses RRTMG longwave and shortwave radiation [*Iacono et al.*, 2008] that has been modified to use spectral albedos and upward longwave radiation passed from the coupler. Morrison two-moment microphysics has been coupled to the RRTMG radiation through predicted ice and water droplet sizes [*Morrison et al.*, 2009].

Convective clouds are represented by the Grell-Devenyi cumulus scheme [*Grell and Dévényi*, 2002].

WRF in this configuration of RASM uses 2.5 minute timesteps and is coupled every 20 minutes. WRF has 40 vertical levels, with the lowest model level at ~12 m and 10 levels in the lowest 1 km over the ocean, and a 10 hPa model top. This configuration of WRF and RASM is sufficiently computationally inexpensive, when run on a large supercomputer, to allow for multi-decadal simulations with adequate resolution for simulating mesoscale wind features [*DuVivier and Cassano*, 2013].

Lateral and upper boundary conditions for this study are provided by the ERA-Interim reanalysis [*Dee et al.*, 2011]; lower boundary conditions and sea ice conditions are not needed in RASM as the surface conditions and ice thickness are determined by and passed to WRF from the land, ocean, and ice models. To constrain the large-scale circulation but still allow for free evolution of the boundary layer system [*Cassano et al.*, 2011], planetary scale temperature and wind fields are spectrally nudged beginning at eta level 20 (~500 hPa) with a strength of zero that is linearly ramped up to 0.0003 sec^{-1} at the top of the atmosphere (for details see Skamarock et al.[*Skamarock et al.*, 2008]).

RASM uses a version of POP that has been modified to run regionally and is eddy-permitting. POP has 45 vertical levels, with 7 levels in the upper 42 m and 19 levels in the upper 500 m. Surface fresh water runoff from land surfaces, including Greenland, is provided to POP by VIC. POP uses K-profile parameterization for vertical mixing [*Large et al.*, 1994], and the POP model's MLD output (HMXL) is used for analysis in this study. The sea-ice model is CICE version 4 [*Hunke and Lipscomb*, 2010] on the same domain as POP and with four predictive sea

ice thickness categories. Details specific to the modifications of POP and CICE within RASM can be found in Roberts et al. [2015]. In order to analyze a time period for which the ice-ocean system has adjusted to the atmospheric forcing within RASM, we have omitted a spin up period from September 1, 1979 until October 31, 1990 from this study.

This study uses daily average WRF, POP, and CICE output for 20 winter seasons (NDJFM) from 1990-2010; the 20 winter seasons capture interannual variability in the large-scale atmospheric circulation and resulting ocean forcing. In this study we will focus only on the wind patterns and surface fluxes around southern Greenland and that occur over the Irminger Sea, Labrador Sea, and Denmark Strait (Figure 29b). The satellite observed sea ice edge is consistent with the ice edge modeled in RASM as defined by the 15% sea ice concentration and mean ice thickness greater than 10 cm (not shown), however to keep the focus of this paper on the air-sea interactions over the open ocean we have masked out sea ice concentrations greater than 15% in our analysis.

b. Wind pattern classification

This study uses the self-organizing map (SOM) neural network algorithm to identify near-surface wind patterns around southeast Greenland and assess the ocean response to each type of pattern. The SOM training algorithm is an unsupervised, iterative process that identifies a user-specified number of representative patterns within a dataset [*Kohonen*, 2001; *Hewitson and Crane*, 2002; *Cassano et al.*, 2007], and arranges similar patterns (or nodes) together into a two-dimensional array, or SOM, where the linear distance between patterns signifies the similarity between representative patterns. The user specifies the number of patterns to be included in the two-dimensional SOM, and the training algorithm objectively determines the representative

patterns. The SOM method has been shown to be a robust method to identify dominant weather patterns across a dataset [*Reusch et al.*, 2005; *Liu et al.*, 2006; *Sheridan and Lee*, 2011].

Because the strongest mesoscale winds occur in the winter from November through March [*Moore*, 2003] and the largest deepening in oceanic mixed layer takes place over this same time period, this project uses wintertime (NDJFM) winds in the SOM training algorithm. The training data used are the 1990-2010 winter daily average (3020 days total) zonal and meridional wind components from the lowest WRF model level (~12 m). Additionally, only data from grid cells that occur over the ocean near the southeastern Greenland coast (boxed region on Figure 29b) were used so that the SOM algorithm identifies patterns based on the speed and direction of mesoscale wind features that directly influence the ocean. A number of SOM sizes (4x2, 4x3, 5x4, 6x4, 6x5, 7x5, 8x6) and training parameters were investigated [*Hewitson and Crane*, 2002; *Cassano et al.*, 2015], and the SOM for each size was chosen to minimize the root mean squared difference (RMSD) between the patterns identified and the data used in the training algorithm.

A 4x3 SOM was chosen because it captures the main types of wind patterns present around Greenland that impact the ocean surface. The data from each of the 3020 days used in the training algorithm was then mapped to one of the 12 representative patterns based on the minimum RMSD between that day's average wind vectors and the representative wind vectors in the SOM; the average RMSD for the 4x3 SOM is 2.7 m s^{-1}. A composite of atmospheric or oceanic variables (i.e. wind speed, 2 m temperature, sea surface temperature, etc.) is calculated by averaging all events that map to a particular pattern; the pattern frequency is the ratio of the number of days that map to a particular pattern relative to the 3020 days used for training the SOM.

The composite zonal and meridional wind components and wind speed for the SOM and pattern frequencies are shown in Figure 30. The SOM is arranged such that patterns with northerly, barrier-parallel winds from the Denmark Strait to Cape Farewell are in the top row, while patterns with southerly or weak coastal winds are in the bottom row. The left columns show easterly flow at Cape Farewell, while the right columns show westerly flow at Cape Farewell. The patterns with the largest differences from one another map to the corners of the SOM and tend to be the most extreme, while transitional patterns occur near the center of the SOM. The patterns in the four corners of the SOM, which were objectively identified during SOM training, correspond to the four sub-types of tip jets chosen subjectively in Moore [2014] – northeasterly, southeasterly, northwesterly, and southwesterly.

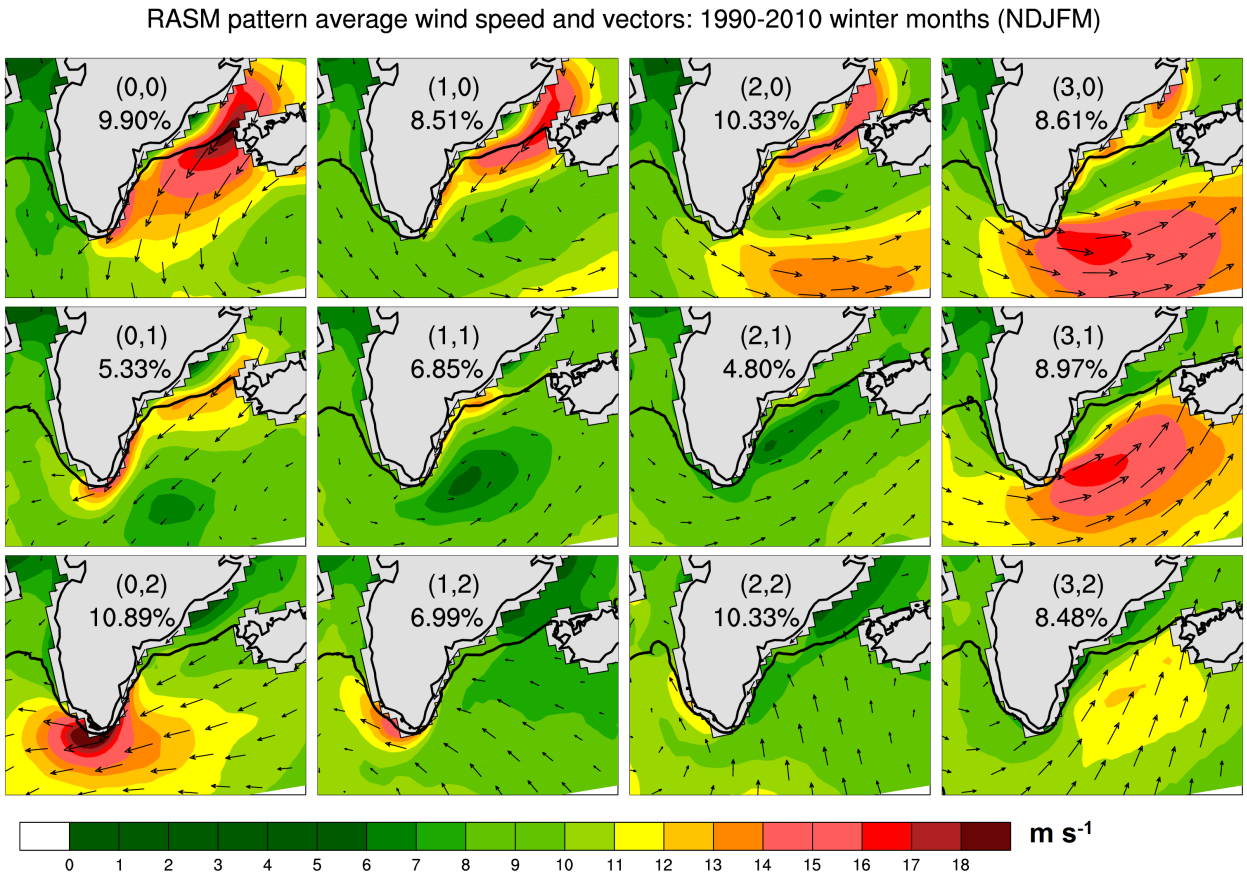

Figure 30: Composite wind speed (m s^{-1}) and wind vectors for each of the 12 representative wintertime wind patterns identified by the SOM. The frequency of occurrence of each pattern is indicated by the percentage below the pattern number. The dark black contour represents the average 15% sea ice contour predicted by CICE in RASM for each pattern.

c. Buoyancy flux

To understand how the atmosphere impacts the surface ocean buoyancy, we use Equation 9, which gives the surface buoyancy flux out of the ocean ([*Marshall and Plumb*, 2007]: equation 11-4):

$$B = \frac{g}{\rho_{ref}}\left[\left(\frac{\alpha_T}{c_w}\left(Q_{Lat}+Q_{Sen}+Q_{LW}+Q_{SW}\right)\right)+\left(\rho_{ref}\beta_s S\left(E-P\right)\right)\right] \quad \frac{m^2}{s^3} \tag{9}$$

A positive buoyancy flux indicates a decrease in buoyancy for surface ocean waters, and thus favors sinking motion. Q_{Lat} is the latent heat flux at the ocean's surface, and Q_{Sen} is the sensible heat flux at the ocean's surface; both turbulent fluxes depend on the scalar wind speed at the lowest WRF model level and the moisture and temperature gradient between the lowest WRF model level and the ocean surface [*DuVivier and Cassano*, 2013]. Q_{LW} is the net longwave flux at the ocean's surface, Q_{SW} is the net shortwave flux at the ocean's surface. For all thermal term components, positive values indicate buoyancy loss from the ocean and gain by the atmosphere. S is the surface salinity, E is the evaporation, and P is the precipitation. A positive value of evaporation indicates buoyancy loss from the ocean, and the negative value of precipitation indicates buoyancy gain by the ocean. The following constants for the seawater equations of state were used as representative for the oceans around Greenland ([*Marshall and Plumb*, 2007]: Table 9.4): the thermal expansion coefficient $\alpha_T = 1\times10^{-4}\,^{\circ}C^{-1}$ and saline contraction coefficient $\beta_S = 7.8\times10^{-4}\,kg\,g^{-1}$. Additionally, the following constants are used: the gravitational constant $g = 9.81\,ms^{-1}$; the density of fresh water $\rho_{ref} = 1000\,kg\,m^{-3}$; the specific heat of fresh water $c_w = 4.18\times10^{3}\,J\,kg^{-1}\,^{\circ}C^{-1}$. A positive buoyancy flux is defined as buoyancy being added to the atmosphere and lost from the ocean, resulting in an increased density of the surface water. The thermal component of the buoyancy flux consists of the net radiative fluxes and the turbulent heat fluxes; the haline term depends on the difference in evaporation and precipitation.

d. Anomaly calculation

In order to remove the seasonal signal from changes in the ocean or atmosphere, atmospheric and oceanic anomaly fields were calculated on each day using the 20-year daily mean values.

2. Buoyancy forcing from atmosphere

a. Net Buoyancy Flux

For all winter wind patterns there is a net loss of buoyancy out of the ocean (Figure 31). The buoyancy loss field from the ocean spatially resembles the maximum wind speed for each pattern (Figure 30), which indicates that the oceanic buoyancy loss is strongly related to the wind speed. This is likely due to the fact that the turbulent fluxes are controlled, in part, by wind speed, as will be shown below. Patterns with northerly, barrier flow (Figure 31, top row) have the maximum buoyancy loss along the ice edge where there are strong winds and cold, dry air first encounters the relatively warmer ocean surface; the magnitude of buoyancy loss decreases with distance from the ice edge. Patterns with southerly flow (Figure 31, patterns on the right side of the bottom row) also remove buoyancy from the ocean, but the magnitude of buoyancy loss is smaller than for patterns with northerly flow. Additionally, easterly tip jet patterns (Figure 31, left column) have a local maximum of buoyancy loss just west of Cape Farewell. Westerly tip jets (Figure 31, right columns) have similar magnitude buoyancy loss along the ice edge and in the core of the atmospheric jet that occurs over the ocean east of Cape Farewell; westerly tip jets also have large buoyancy loss in the Labrador Sea.

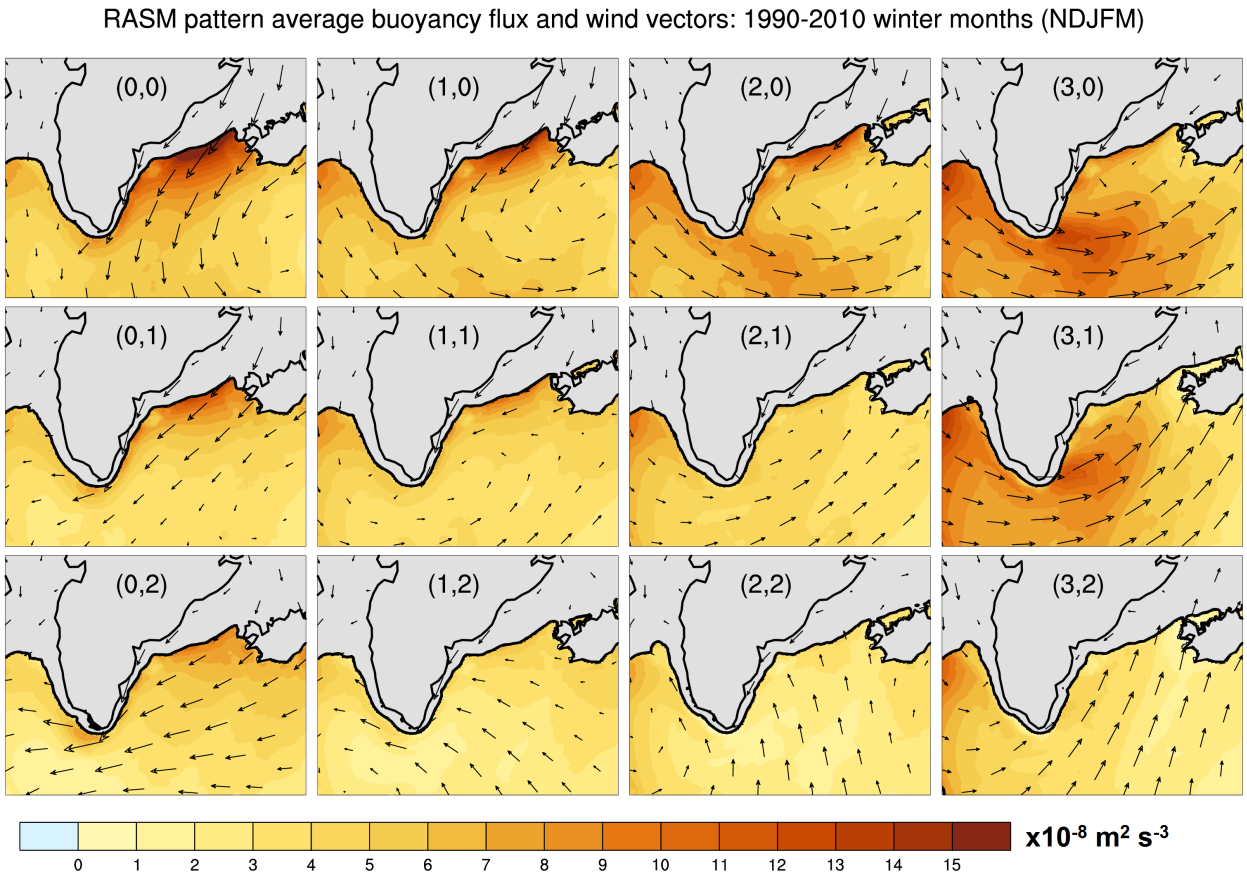

Figure 31: Composite buoyancy flux ($m^2 s^{-3}$) for each of the 12 representative wintertime wind patterns identified by the SOM. The wind vectors are included to remind readers of the representative wind field, and the dark black contour represents the average 15% sea ice contour predicted by CICE in RASM for each pattern.

The percent contribution of the thermal and haline terms to the total buoyancy flux was calculated at each grid point and then averaged across all ocean points with sea ice concentration less than 15%. The same method was used to find the percent contribution of the latent heat flux, sensible heat flux, net longwave, and net shortwave terms to the thermal term, and for the percent contributions of the evaporation and precipitation terms to the haline term. The percent contribution of the thermal and haline terms to the total buoyancy flux are shown in Table 7 as well as the percent contribution of the latent heat flux, sensible heat flux, net longwave, and net shortwave terms to the thermal term and the evaporation and precipitation terms to the haline

term. The thermal term dominates the net buoyancy loss because it is three orders of magnitude larger than the haline term for all wind patterns.

Node	Thermal term	Latent heat flux term	Sensible heat flux term	Net Longwave term	Net Shortwave term	Haline term	Evaporation term	Precipitation term
0,0	100%	47.3%	39.2%	26.9%	-13.4%	0%	613.8%	-513.8%
1,0	100%	46.8%	40.6%	26.5%	-13.9%	0%	653.9%	-553.9%
2,0	100%	46.5%	40.3%	26.2%	-13.0%	0%	112.8%	-12.8%
3,0	100%	45.9%	39.3%	25.5%	-10.7%	0%	344.4%	-244.4%
0,1	100%	51.4%	40.9%	34.2%	-26.5%	0%	-155.3%	255.3%
1,1	100%	47.1%	40.1%	30.1%	-17.3%	0%	-292.0%	392.0%
2,1	100%	46.9%	30.1%	30.3%	-17.2%	0%	-149.6%	249.6%
3,1	100%	47.5%	37.9%	29.3%	-14.8%	0%	-852.8%	952.8%
0,2	100%	51.9%	37.9%	32.9%	-22.7%	0%	61.8%	38.2%
1,2	100%	49.9%	37.4%	34.8%	-22.2%	0%	68.7%	31.3%
2,2	100%	46.4%	37.4%	34.5%	-18.2%	0%	144.5%	-44.5%
3,2	100%	46.6%	39.0%	34.3%	-19.9%	0%	243.3%	-143.3%

Table 7: Grey columns indicate the percent contribution of the thermal and haline terms to the net buoyancy flux for each SOM pattern; the haline term has a 0% contribution because it is three orders of magnitude smaller than the thermal term. The percent contributions of the latent heat flux, sensible heat flux, net longwave, and net shortwave terms to the thermal term are shown to the right of the thermal term column. The percent contributions of the evaporation and precipitation terms to the haline term are shown to the right of the haline term column. Double bars in the table represent the row divisions for the SOM.

The co-location of buoyancy flux maxima with the wind speed maxima (Figures 30 and 31) suggests that the turbulent heat fluxes may be strong drivers of the overall buoyancy loss, and the percent contribution of the two turbulent flux terms to the thermal term confirm that turbulent fluxes dominate the overall buoyancy loss. The two turbulent flux terms are responsible for 65 to 75% of the total buoyancy flux. The percent contribution of the latent heat flux term is similar (46 to 52%) for all patterns and makes a larger contribution to the buoyancy flux than the sensible heat flux term. The sensible heat flux contributes most for patterns with northerly, barrier flow (39 to 40%) and is slightly lower for patterns with weak barrier flow or southerly

flow (33 to 35%). Like the turbulent terms, the net longwave term also removes buoyancy for the ocean for all patterns, and it is somewhat more important, in a relative sense, for patterns with weak barrier flow or southerly flow (33 to 35%) than for patterns with northerly flow (26 to 27%). For all patterns the net shortwave term adds buoyancy to the ocean (-27 to -11%), but is unsurprisingly small given the decrease in daylight hours during the winter.

Unlike the thermal term, the percent contributions of the precipitation and evaporation to the haline term vary for the different patterns. This indicates that the specifics of local buoyancy gain through precipitation and buoyancy loss from evaporation for each wind pattern are important for the overall sign and pattern of the haline term. However, because the haline term and its components are all three orders of magnitude smaller than the thermal term and its components it is relatively unimportant for the ocean response to atmospheric forcing.

b. Spatial patterns of buoyancy flux

In this section we will investigate the spatial buoyancy flux field for the wind patterns at the four corners of the SOM (Figure 30) in order to understand how the individual terms contribute to the net buoyancy loss. We have chosen to analyze the four corner patterns because they are the most different from one another and provide a sense of how the ocean responds to these very different wind events. The four corner patterns represent strong easterly (bottom left) and westerly (top right) tip jets, strong barrier flow (top left and top right), and predominantly southerly flow (bottom right). We focus our discussion on the thermal, sensible heat flux, latent heat flux, and longwave terms because they are the largest contributors to the net buoyancy flux (Table 7), but we also include a brief discussion of the haline term. In order to keep the focus on the four edge patterns and the dominant terms of the buoyancy flux, Figure 32 shows composites of the fluxes and factors that contribute to those fluxes for the four corner patterns only; figures

showing the contributions for each pattern in the 12 member SOM can be found in the supplementary material for the following terms: thermal term (Supplementary Figure 7), latent (Supplementary Figure 8) and sensible (Supplementary Figure 9) heat fluxes, net longwave (Supplementary Figure 10) and shortwave (Supplementary Figure 11) terms, haline term (Supplementary Figure 12), evaporation (Supplementary Figure 13), and precipitation (Supplementary Figure 14). Additionally, the atmospheric temperature (Supplementary Figure 15) and moisture (Supplementary Figure 16) anomalies for each of the 12 patterns can be found in the supplementary material.

The composite wind speed for the four patterns is shown in Figure 32a, and these four corner patterns have also been identified in Moore [2014] as subgroups of tip jets. Pattern (0,0) represents a northeasterly tip jet with barrier flow (NETJ) where the maximum wind speed occurs along the ice edge in the Denmark Strait. Pattern (0,2) represents an easterly tip jet with weaker barrier flow (ETJ) and maximum wind speed west of Cape Farewell. Pattern (3,0) is a northwesterly tip jet with barrier flow (NWTJ) and maximum wind speed over the Irminger Sea to the east of Cape Farewell. Pattern (3,2) has a southwesterly tip jet (SWTJ) with maximum speeds over the Irminger Sea northeast of Cape Farewell, but with a smaller magnitude maximum than the other corner patterns.

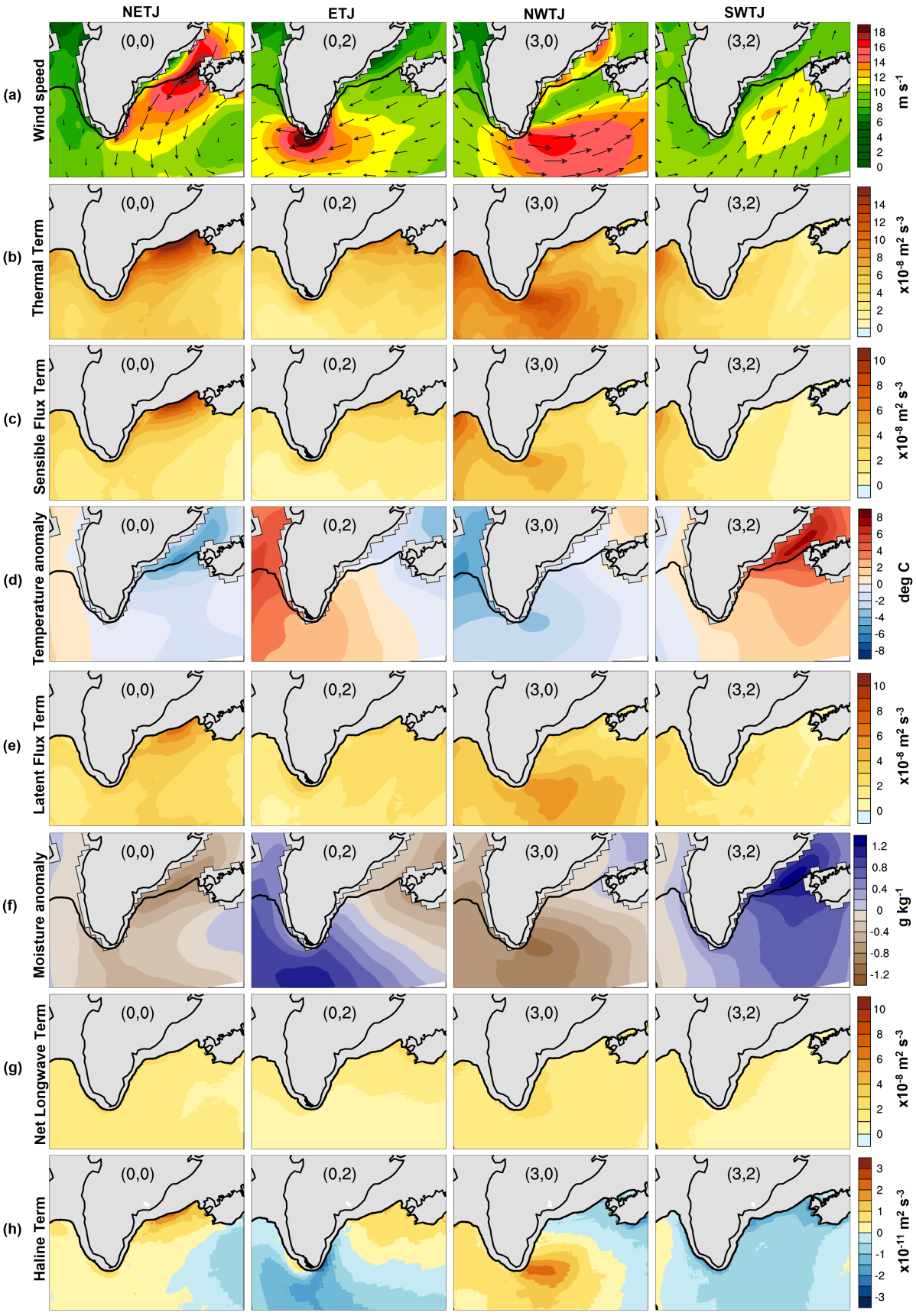
NETJ
ETJ
NWTJ
SWTJ
(a)
Wind speed
m s-1
(b)
Thermal Term
x10-8 m2 s-3
(c)
Sensible Flux Term
x10-8 m2 s-3
(d)
Temperature anomaly
deg C
(e)
Latent Flux Term
x10-8 m2 s-3
(f)
Moisture anomaly
g kg-1
(g)
Net Longwave Term
x10-8 m2 s-3
(h)
Haline Term
x10-11 m2 s-3
(0,0)
(0,2)
(3,0)
(3,2)

Figure 32: (a) Composite wind speed (m s^{-1}) and wind direction for the corner patterns – Northeasterly Tip Jet (NETJ – 0,0), Easterly Tip Jet (ETJ – 0,2), Northwesterly Tip Jet (NWTJ – 3,0), Southwesterly tip jet (SWTJ – 3,4). Composite (b) thermal buoyancy term (m^2 s^{-3}), (c) sensible heat flux buoyancy term (m^2 s^{-3}), (d) near-surface atmospheric temperature anomaly (°C), (e) latent heat flux buoyancy term (m^2 s^{-3}), (f) near-surface atmospheric moisture anomaly (g kg^{-1}), (g) net longwave buoyancy term (m^2 s^{-3}), and (h) haline buoyancy term (m^2 s^{-3}). On all panels, the dark black contour represents the average 15% sea ice contour predicted by CICE in RASM for each pattern.

The thermal term (Figure 32b) spatially resembles the wind speed (Figure 32a) for patterns with northerly flow (NETJ and NWTJ) but not for patterns with a southerly component to the flow (ETJ and SWTJ). For the NETJ, the maximum thermal buoyancy loss occurs along the sea ice edge in the Denmark Strait and decreases with distance from the ice edge. There is a secondary maximum along the coast and to the northeast of Cape Farewell, and both of these flux maxima coincide with wind speed maxima. Both the NETJ and ETJ have a local maximum for the thermal term just west of Cape Farewell, but only the ETJ has a maximum in wind speed co-located with this region of enhanced buoyancy flux. Like the NETJ, the ETJ has enhanced buoyancy loss along the Denmark Strait ice edge but the ETJ has relatively weak winds in this location. The NWTJ has a local maximum in the thermal term over the Irminger Sea, where the largest wind speeds occur, but there is also a local maximum over the Labrador Sea where weaker winds are present. The buoyancy loss for the SWTJ is generally smaller than for the other patterns, other than in the Labrador Sea, and for this pattern the largest buoyancy loss is not co-located with the largest wind speeds. Because the turbulent flux terms are the largest contributors to buoyancy loss (Table 7, 65 to 75%) and the turbulent fluxes depend directly on wind speed the similarity between the wind speed and flux field is not surprising. However, because each pattern has regions of elevated buoyancy loss where there are weak winds, it is necessary to examine other influences on the buoyancy flux.

The sensible heat flux term (Figure 32c) for all patterns is elevated along the sea ice edge –in the Denmark Strait for NETJ and ETJ and in the Labrador Sea for the NWTJ and SWTJ – where anomalously cold atmospheric temperatures (Figure 32d) first encounter the relatively warm ocean waters. The magnitude of buoyancy loss decreases with distance from the ice edge as the cold atmospheric temperature anomaly decreases as the atmosphere adjusts to the flux of heat from the ocean. For both the NETJ and ETJ elevated sensible fluxes in the Denmark Strait decrease to the south as the cold temperature anomaly becomes weaker, but for the NETJ the decrease in fluxes corresponds to a decrease in wind speed while the ETJ decrease in fluxes corresponds to an increase in wind speed. Both the NWTJ and SWTJ have local maximum in sensible heat flux terms in the Labrador Sea where relatively weak westerly atmospheric flow brings cold air off the North American continent or sea ice further to the north and over the open ocean [*Renfrew and Moore*, 1999]. For the NWTJ there is also elevated buoyancy loss due to the sensible term immediately east of Cape Farewell where there is both a maximum in wind speed and a minimum in temperature anomaly due to either air descending the terrain [*Doyle and Shapiro*, 1999] or continental air that is accelerated around Cape Farewell [*Våge et al.*, 2009]. In all patterns the largest sensible fluxes occur where there are anomalously cold atmospheric temperatures, so changes in the temperature anomaly drive changes in sensible term while changes in wind speed are secondarily important.

The latent heat flux term (Figure 32e) depends on both the atmospheric moisture anomaly (Figure 32f) and the wind speeds (Figure 32a). For NETJ the largest latent heat term is along the sea ice edge where the driest northerly flow encounters the ocean surface and there is also a wind speed maximum; along the coast to the northeast of Cape Farewell there are elevated wind speeds but not an significantly elevated latent term because the air is less anomalously dry. The

ETJ has anomalously moist conditions in the vicinity of maximum wind speeds southwest of Cape Farewell, so the latent heat flux for this pattern is relatively weak compared to the NETJ and the spatial pattern of latent heat term is dominated by the moisture anomalies, not the winds. The maximum latent heat term for the NWTJ occurs where there is both a maximum in wind speed and anomalously dry air, southeast of Cape Farewell. The latent term is not elevated in the Labrador Sea where there are weak winds co-located with anomalously dry conditions, which indicates wind speed is important for determining the location of maximum fluxes. The SWTJ has anomalously moist conditions and lower wind speeds over much of the study domain that leads to a smaller latent heat term than for any other pattern. For the four wind patterns reviewed above, having anomalously dry air and strong winds is important to drive a large latent heat term. Where there is dry air but weak winds, such as over the Labrador Sea for NWTJ, there are small latent heat terms, and where there are strong winds but moist air, such as west of Cape Farewell for ETJ, there are also small latent heat terms.

Near the sea ice edge the buoyancy loss from the sensible term is largest, but over the ocean the magnitude of buoyancy loss from sensible and latent terms are similar. For all patterns the ocean loses buoyancy from the sensible (latent) heat terms over the entire domain because the temperature (moisture) gradient is such that the atmosphere is colder (drier) than the ocean surface (not shown). The temporal and spatial evolution of the magnitude of the temperature (moisture) gradient is driven primarily by the atmospheric temperature (moisture) anomaly rather than the sea surface conditions, which have much smaller relative changes in magnitude than the atmospheric state. Therefore, the NETJ and NWTJ patterns with northerly barrier flow are anomalously cold and dry due to northerly winds and cold air advection, while the ETJ and SWTJ patterns with a southerly component are anomalously warm and moist and result in less

buoyancy loss. The combination of wind speed maxima and anomalously cold and dry conditions leads to the largest turbulent flux terms and buoyancy loss from the ocean.

The net longwave term (Figure 32g) is smaller in magnitude than the turbulent terms, and it is fairly constant over the whole domain indicating that the impact of wind patterns on cloud cover and the resulting longwave buoyancy loss is small. Slightly elevated buoyancy loss can be seen for NWTJ to the east of Cape Farewell where dry, off-continent flow would likely lead to clearer skies and more longwave loss from the ocean. The shortwave term (Supplementary Figure 11) is fairly constant over the whole domain as well, though in areas with clear sky, like that for the NWTJ, the oceanic buoyancy gain is slightly larger.

Unlike the thermal buoyancy term (Figure 32b), the haline buoyancy term (Figure 32h) sometimes removes buoyancy from the ocean, reinforcing the thermal buoyancy loss, and sometimes adds buoyancy to the ocean. (Note: the color bar for the haline buoyancy term in 32h is 3 orders of magnitude smaller than for the thermal buoyancy term in 32b). The evaporation term (Supplementary Figure 13) follows the latent heat flux term, so the haline term tends to remove ocean buoyancy in locations where there is a large latent heat flux due to the evaporation. This can be seen in NETJ and the NWTJ where the haline term is positive, indicating ocean buoyancy loss, where there are elevated latent heat fluxes (Figure 32e). However, for patterns such as the ETJ and SWTJ where there is upslope atmospheric flow onto the Greenland continent, localized precipitation can lead to oceanic buoyancy gain (Supplementary Figure 14). However, the haline contributions only add small constructive or destructive signals to the thermal term because the magnitude is so much lower than the thermal terms.

4. Ocean response

a. Mixed layer depth changes

The oceanic buoyancy loss that occurs for all wind patterns (Figure 31) indicates that the surface waters are becoming denser and may sink. From November 1 to March 31, over the winter season, the MLD increases in the Irminger Sea and Labrador Seas (Supplementary Figure 17). The deepest MLDs are in the Labrador Sea, but the Irminger Sea has mixed layers deeper than 500 m.

To understand how the buoyancy forcing from the 12 representative wind patterns impact the ocean MLD, we examine the composite MLD anomaly as a percent of the mean MLD (Figure 33). Patterns with northerly barrier flow (top row and left two patterns in center row of Figure 33) tend to have the largest buoyancy loss from the ocean, particularly along the sea ice edge in the Denmark Strait. For the patterns with northerly flow, except pattern (3,0), anomalously deep MLD in the Denmark Strait along the ice edge are co-located with the region of maximum buoyancy loss (top row and left two patterns in center row of Figures 31 and 33). For pattern (3,0) maximum buoyancy loss in the Denmark Strait is co-located with anomalously shallow MLD, which indicates buoyancy forcing is not the primary driver of MLD in this region for this wind pattern and that other factors are contributing to a shoaling of the mixed layer in this region despite the large buoyancy loss. For patterns with northerly flow over the Labrador Sea and westerly winds at Cape Farewell – patterns (2,0), (3,0), (2,1), and (3,1) – the MLD is anomalously deep in both the Labrador and Irminger Seas (Figure 33). However, for these wind patterns the anomalously deep MLD are not exactly co-located with the regions of maximum buoyancy flux (Figure 31): in the Labrador Sea the deepest MLD are to the southeast of the maximum buoyancy flux and in the Irminger Sea the MLD anomaly is fairly uniform over the region of the wind jet and is not especially deep in regions of largest buoyancy loss. Therefore,

while the MLD anomaly is coherent with the buoyancy forcing, there is likely additional forcing that is not being considered and is modulating the MLD anomaly for patterns with northwesterly tip jets. Patterns with southerly flow have relatively small buoyancy loss throughout the domain (Figure 31, bottom row) and the resulting MLD tends to be anomalously shallow (Figure 33, bottom row), though pattern (0,2) has both elevated buoyancy fluxes and anomalously deep MLD in the Denmark Strait associated with northeasterly flow in this region. In general these MLD anomalies make sense: where there is cold, dry northerly flow that drives elevated buoyancy flux, there tend to be anomalously deep MLD in the Irminger Sea due to surface water densification and sinking.

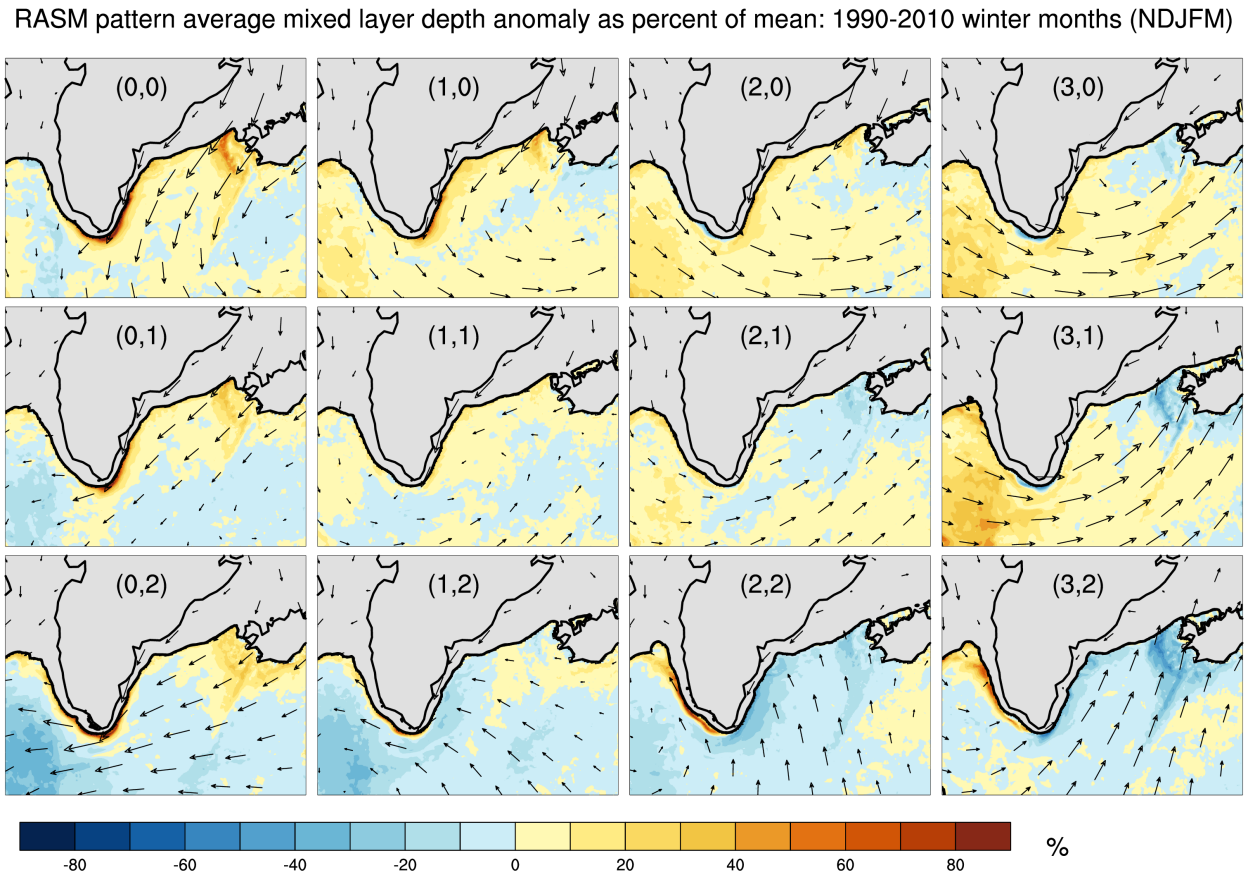

Figure 33: Composite MLD anomaly as a percent of the mean ocean MLD (%) for each of the 12 representative wintertime wind patterns identified by the SOM. The wind vectors are included to remind readers of the representative wind field, and the dark black contour represents the average 15% sea ice contour predicted by CICE in RASM for each pattern.

However, along the coast there are noticeable responses in MLD anomaly to mechanical Ekman forcing. In the northern hemisphere, when wind blows parallel to a coastline if the coast is located to the right of the main wind direction, as is the case in pattern (0,0) Ekman transport will force water toward the coastline and cause downwelling [*Cushman-Roisin and Beckers*, 2011]. The opposite response, upwelling, occurs for flow with the coast located to the left of the wind vector. For easterly tip jets and patterns with strong winds parallel to the coast northeast of Cape Farewell – patterns (0,0), (1,0), (0,1), and (0,2) – there is a narrow band of strong deepening along the coast just north of Cape Farewell where there are winds parallel to the coastline and mechanical Ekman transport would force downwelling (Figure 33). For patterns

with southerly flow along the coast west of Cape Farewell – patterns (0,2), (1,2) and (2,2) – deepening of the MLD in this region is related to Ekman transport into the coastline as well.

Given the coherent relationship between MLD anomaly and the various wind patterns discussed in the previous paragraphs it is useful to explore how interannual variability in the different wind pattern frequencies impacts the total winter change in MLD (March 31 – November 1). We have correlated the yearly frequency of each atmospheric pattern with the seasonal change in MLD at each point. Correlations are assumed to be linear with no lag, and significance was calculated using the r-test. The correlation coefficient between pattern frequency and seasonal mixed layer deepening is shown in Figure 34, and we will focus our discussion on patterns with large regions of significant correlation. Patterns with westerly flow at Cape Farewell – patterns (2,0) and (3,0) –have large areas of positive correlation between pattern frequency and mixed layer deepening in the Irminger and/or the Labrador Sea (Figure 34). The positive correlation indicates that when those patterns occur more frequently there is a larger magnitude seasonal deepening of the mixed layer in the Irminger and Labrador Seas. For these patterns, particularly pattern (3,0), the MLD deepening occurs where there are large buoyancy fluxes in the Irminger and Labrador Seas (Figure 31). We also see that for patterns (0,0) there are positive correlations between this pattern frequency and MLD deepening in the central Irminger Sea (Figure 34), where there are anomalously deep MLD (Figure 33) and large buoyancy fluxes (Figure 31). There is also a positive correlation between the frequency of pattern (0,2) and seasonal MLD deepening along the Greenland coast in the Labrador Sea (Figure 34). This region west of Cape Farewell is also where there are large buoyancy fluxes during an easterly tip jet (Figure 31). Patterns (1,2) and (3,2) with southerly flow are negatively correlated to seasonal MLD deepening in the Labrador and Irminger Seas, respectively (Figure 34), and the areas of

negative correlation correspond to low buoyancy fluxes (Figure 31). The negative correlation indicates that when those patterns occur more frequently the seasonal deepening of the mixed layer is smaller.

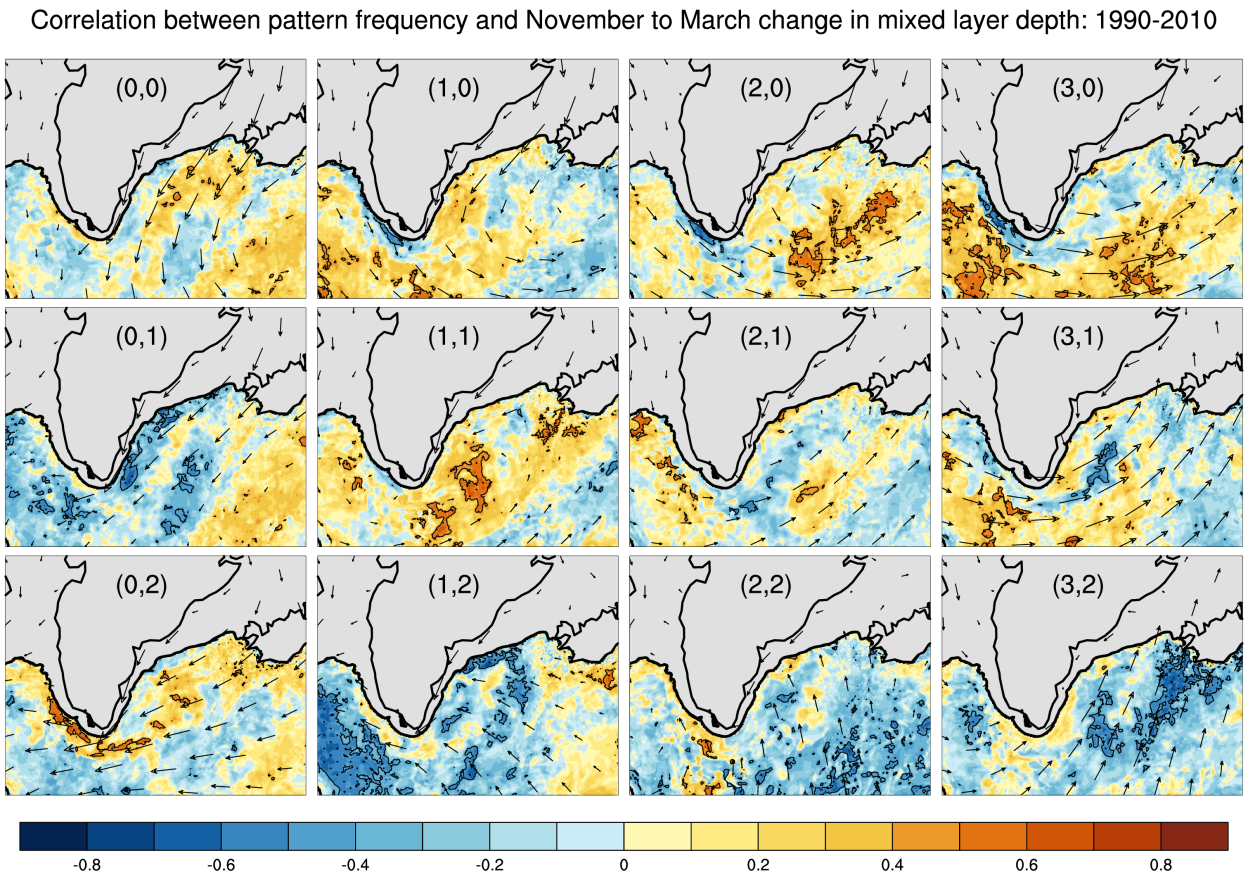

Figure 34: Correlation between pattern frequency and MLD change November 1 to March 31 over 20 winter seasons for each of the 12 representative wintertime wind patterns identified by the SOM. Correlations that are significant at the 95% level are stippled, wind vectors are included to remind readers of the representative wind field, and the dark black contour represents the average 15% sea ice contour predicted by CICE in RASM for each pattern.

c. Long vs. short duration events

Because the ocean has a relatively long memory compared to the atmosphere, longer duration strong wind events are expected to impact the ocean more than short duration events. We define an "event" as beginning if the previous day mapped to a different wind pattern in the SOM; the duration for an event is the number of sequential days that map to the same wind

pattern. Table 8 gives the percent of time that each wind pattern lasts for one day, two days, and three or more days. For all patterns, most events last a single day (on average ~71%) while a smaller percentage last three or more days (on average ~10%). We define "short" events as those that last one day only, and "long" events as those that last three or more days. For this discussion we will focus on the NETJ and NWTJ patterns, (0,0) and (3,0) respectively, since we have shown that these patterns have the largest buoyancy forcing due to the cold, dry northerly flow and a strong relationship to MLD. Other patterns have weaker buoyancy forcing, so the relationship between MLD response to buoyancy forcing from long and short duration events is less clear and will not be discussed here.

Node	1 day	2 days	3+ days
0,0	52.2%	27.3%	19.4%
1,0	69.2%	21.4%	9.3%
2,0	74.3%	17.4%	8.3%
3,0	69.8%	22.0%	8.2%
0,1	79.8%	15.5%	4.7%
1,1	86.6%	12.3%	1.1%
2,1	86.6%	12.6%	0.8%
3,1	59.8%	30.5%	9.8%
0,2	52.8%	19.0%	28.2%
1,2	80.0%	16.5%	3.5%
2,2	70.1%	19.4%	10.4%
3,2	69.4%	17.9%	12.7%

Table 8: Frequency of events of different duration for each SOM pattern. An event is defined as beginning when the previous day's pattern did not map to the same pattern. The duration is the number of sequential days that map to the same pattern. Double bars in the table represent the row divisions for the SOM.

Figures 35a and 35b show the wind speed and total buoyancy flux for the first day of the average short and long duration NETJ and NWTJ event, and the corresponding change in oceanic MLD over that first day. For both types of wind patterns, on the first day of a new event

there are faster wind speeds and larger buoyancy fluxes out of the ocean for the long duration events compared to the short duration events, which suggests that long events have stronger background forcing than short events. In the Irminger Sea a long duration NETJ results in deepening over a larger area than a short duration NETJ, but the magnitude of deepening is similar for both the long and short duration events. In the Irminger Sea the spatial pattern and magnitude of MLD change is similar for both the short and long duration NWTJ events. The relatively similar MLD response in the Irminger Sea to the differing strength of buoyancy forcing for long and short duration events indicates that after one day the ocean has not yet begun to respond to and reflect the stronger forcing associated with long duration events. In the Labrador Sea, the long duration NWTJ results in more deepening compared to the short duration NWTJ, which is consistent with the larger buoyancy flux in this region associated with the long duration NWTJ.

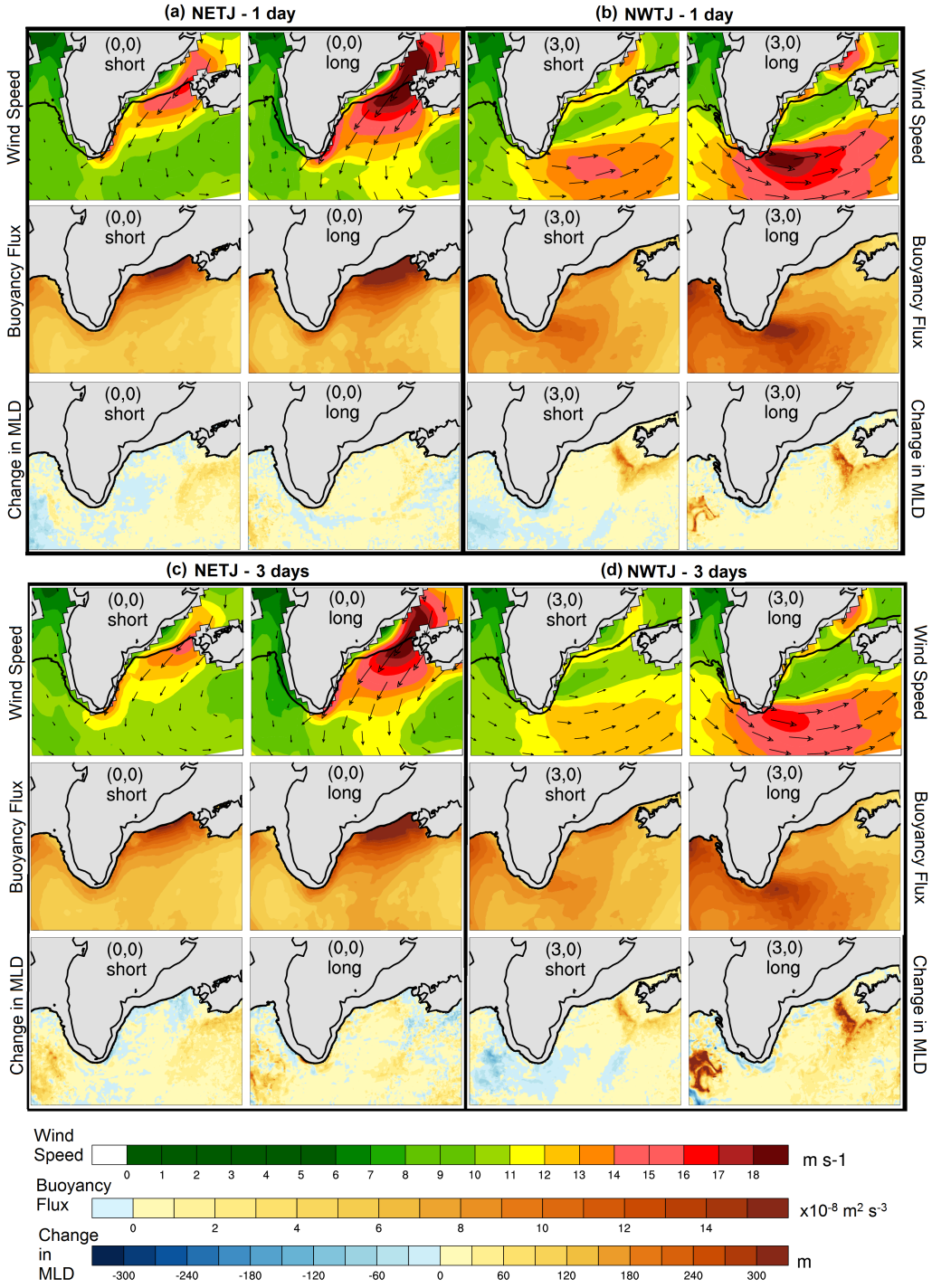

Figure 35: Composite of short (left column of each panel) and long (right column of each panel) duration Northeasterly Tip Jet (NETJ – 0,0) (panels a and c) and Northwesterly Tip Jet (NWTJ – 3,0) (panels b and d) events. Composite wind speed (m s^{-1}) (top row of each panel), net buoyancy flux (m^2 s^{-3}) (middle row of each panel), and change in MLD (m) (bottom row of each panel) over the first day of an event (panels a and b) or over the first three days of an event (panels c and d). The dark black contour represents the average 15% sea ice contour predicted by CICE in RASM for each pattern.

The difference in ocean response to short and long events and the importance of the long ocean memory is more apparent when we investigate several days after the start of an event. Three days after an event begins the short duration events will have transitioned to a different wind pattern and buoyancy forcing two days prior, while a long event with consistent wind and buoyancy forcing is just ending. For both short and long NETJ and NWTJ events, after three days the average wind speeds (figures 35c and 35d) are weaker than on the first day of an event (Figures 35a and 35b), but for long events the memory of the original wind pattern is stronger due to the repetition of the wind field over all three days included in the composite. For short events, however, the original wind pattern only lasts one day, so several days after the start of an event the average wind field weakly resembles the pattern from the original event.

Buoyancy fluxes are primarily driven by sensible and latent heat flux terms, and these depend on wind speed. Thus, the three day average buoyancy flux for long events (Figures 35c and 35d) is similar to the buoyancy flux on day one of long events (Figure 35a and 35b), with only a slightly reduced magnitude. However, for short events the average buoyancy flux over three days has diminished because the wind pattern has transitioned elsewhere and the original buoyancy signal is washed out by the buoyancy flux patterns associated with the new wind patterns. The MLD response three days after an event begins also differs as a result of the different buoyancy forcing for short and long events. For long duration NETJ events compared to short events, there is a larger area of MLD deepening along the Denmark Strait ice edge and the southeast coast just north of Cape Farewell, and these areas are co-located with large buoyancy fluxes (Figure 35c). In the Labrador Sea, however, there are relatively small buoyancy fluxes for short and long duration NETJ and the MLD response is similar for both short and long events. For long duration NWTJ there is greater magnitude MLD deepening, particularly in the

Labrador Sea where there is a large buoyancy flux for long events (Figure 35d). There is also more MLD deepening over a larger area of the Irminger Sea for long duration events compared to short events that also corresponds to regions of large buoyancy flux (Figure 35d).

5. Discussion and Conclusions

The ocean loses buoyancy and becomes denser during all types of wintertime wind patterns that occur around southeastern Greenland (Figure 31), and this buoyancy loss is primarily driven by the thermal term while the haline contribution to the buoyancy flux is negligible (Table 7). The longwave radiative contribution to buoyancy loss is less than the turbulent heat flux terms, though still contributes 25-35% of the buoyancy loss. Conversely, net shortwave radiation adds a small amount of buoyancy to the surface waters that acts to inhibit ocean convection. The turbulent flux contributions to the buoyancy loss tend to have similar patterns to the wind field and atmospheric temperature and moisture anomalies, while the radiation contributions are relatively uniform throughout the domain and do not differ considerably for the different wind patterns.

Patterns with the largest buoyancy fluxes are those with northerly flow that brings cold, dry air over the ocean, while patterns with southerly flow tend to have warmer, moister air that does not drive as large of buoyancy loss (Figures 31 and 32). There is the most buoyancy loss from the sensible heat term along the ice edge where cold air encounters the relatively warmer ocean (Figures 32c and 32d). In this region, cold atmospheric temperature anomalies (Figure 32d) primarily drive large sensible heat flux buoyancy loss. When fast winds are co-located with the cold temperature anomalies the strong winds enhance the buoyancy loss (Figure 32a). For the latent heat flux term, however, the combination of dry atmospheric conditions (Figure 32f) and fast winds (Figure 32a) are important to drive the largest latent heat fluxes (Figure 32e). The

latent flux term is small where there are dry conditions but weak winds, such as over the Labrador Sea for NWTJ, and where there are strong winds but moist air, such as west of Cape Farewell for ETJ. Instead, there must be both strong winds and dry conditions to drive the largest latent heat terms, such as along the Denmark Strait ice edge for the NETJ or in the core of the jet for NWTJ.

The MLD anomaly (Figure 33) associated with each pattern can be related to a combination of the buoyancy forcing (Figure 31) and mechanical Ekman forcing associated with each pattern. As an example, NETJ patterns have anomalously deep MLD just south of the Denmark Strait where there are large buoyancy fluxes out of the ocean, and anomalously deep MLD along the southeast coast of Greenland where Ekman transport forces mechanical downwelling. Because northerly flow drives the largest fluxes, patterns with northerly flow tend to have anomalously deep MLD (Figure 33, top row), and those patterns' frequency is positively correlated with MLD deepening in the Irminger and Labrador seas over the winter (Figure 34, top row). Additionally, longer duration NETJ and NWTJ are shown to drive MLD deepening over a larger spatial area and with greater magnitude in regions of large buoyancy loss (Figures 35c and 35d) indicating that persistent atmospheric forcing enhances the ocean response.

By using 20 winters of model output from a fully coupled, dynamically complex ocean model driven by a high-resolution atmosphere model that explicitly represents mesoscale winds, we have shown that the ocean responds to mesoscale wind events and the response differs for the different types of mesoscale wind patterns that exist around Greenland. Patterns with northerly flow drive MLD deepening in the Irminger Sea regardless of the wind direction at Cape Farewell and the resulting type of tip jet. However, the locations of MLD deepening differ for NETJ and NWTJ based on the location of the maximum buoyancy loss. Additionally, patterns with

westerly flow at Cape Farewell impact the Labrador Sea as well as the Irminger Sea and deepen the mixed layer in both locations. There is a local maximum in buoyancy loss to the west of Cape Farewell for ETJ that is relatively weak compared to the NETJ or NWTJ buoyancy forcing because the ETJ has a component of southerly flow. However, there is moderate MLD deepening to the west of Cape Farewell for an ETJ, but because of the weaker forcing the degree of preconditioning or eddy activity may be important in this location for the response of the MLD.

While this study has addressed many questions regarding the thermodynamic impact of different mesoscale winds on the ocean, questions still remain. This study uses an atmosphere model at 50 km when previous case studies show that using an atmospheric resolution of 10 km is ideal for representing mesoscale wind patterns [*DuVivier and Cassano*, 2013]. The ocean response may be enhanced or more distinct for particular wind patterns when forced with a higher resolution atmosphere that has a more detailed wind field with faster winds [*Hughes and Cassano*, 2015]. Additionally, this study has not addressed the impact of ocean eddies on convective processes or other mechanical influences on the MLD such as Ekman pumping or suction due to wind stress curl or bathymetric effects. Additionally, we have not considered how particular wind patterns or transitions between wind patterns may impact ocean preconditioning and how the ocean responds to a particular type of wind event or sequence of wind events. We also have not considered how the ocean would respond to different types of mesoscale winds given a particular preconditioning state. Future work will more thoroughly address the oceanic impact by mechanical processes and subtle connections between different types of wind patterns.

6. Acknowledgements

This research was supported by the United States Department of Energy (DOE) grants DE-FG02-07ER64462 and DE-SC0006178 and NSF grant PLR 1107788. Data are available from the authors upon request.

Chapter 6: Conclusion

The work presented in this dissertation used regional atmospheric models, reanalysis data, and a fully coupled Arctic system model to evaluate how modeled mesoscale wind events drive air-sea interactions and the ocean response to the surface forcing in the seas around southeastern Greenland. The Irminger and Labrador Seas are one of the few regions in the world where downwelling occurs as part of the global ocean circulation, so it is important to investigate the possible impact of mesoscale wind events on this convection. Because obtaining in-situ observations in this region prone to hurricane force winds is difficult, numerical models are an essential tool for understanding the connections between the short-lived wind events and the longer-term oceanic response. Simulations of observed easterly tip jet and barrier wind events were run at various resolutions to establish how differing resolutions represent mesoscale wind events. By comparing Weather Research and Forecasting (WRF) model output at 10 km, 25 km, 50 km, and 100 km and ECMWF Interim (ERA-I) reanalysis at ~150 km with QuikSCAT satellite observations and Greenland Flow Distortion Experiment (GFDex) dropsonde observations, it was determined that all model resolutions captured the synoptic features present during these events but that the 10 km simulation best represented the mesoscale features of the observed winds, and that 50 km was the minimum grid spacing required to simulate the mesoscale wind events.

Without fine enough horizontal grid spacing WRF did not have steep enough terrain gradients to effectively modify the local pressure gradient and drive strong wind features. A 10 km grid spacing was needed to capture the vertical and horizontal wind structure observed by aircraft and satellite. The 10 km simulation represented the vertical structure of atmospheric

boundary layer and the fine detail of the wind speed gradient, as seen through the relative vorticity and wind stress curl fields while the lower resolution WRF simulation and ERA-I had smoothed features without the fine level of detail present in observations.

The mean turbulent fluxes, which depend directly on wind speed, are similar when averaged over the Irminger Sea for WRF at 10 km, 25 km, and 50 km but differed locally at these different resolutions. The 10 km WRF simulation drove the largest magnitude turbulent heat fluxes (up to 29% larger than 25 km WRF and 60% larger than 50 km WRF) that were concentrated in areas co-located with the mesoscale wind jet. These larger fluxes are driven by the combination of faster winds and larger air-sea vertical temperature and moisture gradients. As a result of the higher fluxes, an ocean model driven with high resolution atmospheric data will lose more energy through turbulent fluxes than if it was driven with lower resolution atmospheric data. Because the high-resolution model concentrates the highest fluxes over a small area there is likely to be a larger impact on the small-scale processes involved in ocean convection. While the spatial co-location of high fluxes with the mesoscale jets makes physical sense, we found that the WRF model has a high bias for turbulent fluxes when compared to GFDex near surface observations. This high flux bias compared to observations is likely related to the WRF surface layer parameterizations, which may not treat the friction velocity, roughness length, and stability correctly for the extreme conditions associated with mesoscale wind events.

While case studies are useful for validating modeled wind events with observations, the ocean has a long memory and ice-ocean models require multidecadal atmospheric forcing data, so it is important to understand the variability in the types of wind events around Greenland and differences between atmospheric datasets over longer time periods. A self-organizing map (SOM) was used to investigate the range of wind patterns around southeastern Greenland and to

understand differences between wind patterns from WRF at 50 km and the ERA-I reanalysis data over 10 winters. The SOM algorithm objectively determined 35 wind patterns that occur around southeastern Greenland during the winter months of NDJFM. Of the 35 patterns, ~42% of the patterns had a westerly tip jet at Cape Farewell and ~30% of the patterns had an easterly tip jet at Cape Farewell. However, there was a range in wind speeds over the manifestations of each type of tip jet, and both easterly and westerly winds can occur either with or without barrier winds. The type of tip jet present at Cape Farewell is well correlated with the sign of the NAO, but the absence or presence of barrier winds is not well correlated with the NAO. Because northerly barrier flow is important for determining the near-surface atmospheric state that drives air-sea turbulent fluxes, using the sign of the NAO is not necessarily a good predictor of air-sea fluxes, which depend on the near-surface state.

The WRF and ERA-I mean wind fields for all 10 winters are similar over the Irminger Sea where synoptic forcing dominates, but along the coast WRF has faster winds than ERA-I. The faster coastal wind speeds are due to WRF simulating both faster barrier winds for each type of wind pattern and patterns with barrier flow occurring more frequently in WRF. Because WRF has higher resolution than ERA it is better able to simulate the terrain gradients required for blocking synoptic flow and driving mesoscale winds, but 50 km is still not sufficiently high resolution to capture detailed terrain influences. This is particularly relevant for areas like the Denmark Strait where steep terrain constrains the flow on two sides and high resolution is important for capturing both peak wind speeds and low speeds in the lee of the terrain.

While winds have an important impact on turbulent fluxes, the near-surface atmospheric state (temperature and humidity) associated with the different wind patterns also impacts the fluxes for each pattern. Ice-ocean models are designed to use near-surface atmospheric state data,

sometimes from multiple sources, to calculate turbulent fluxes. In order to follow the flux calculation method used by ice-ocean models, for this analysis the COARE bulk flux algorithm was used with the WRF and ERA-I near surface data to compute turbulent fluxes for each dataset, and then composited for each wind pattern. COARE has been shown to be the best performing surface parameterization in high wind conditions. The COARE turbulent fluxes are largest in magnitude and cover the largest area for wind patterns with westerly tip jets with barrier flow, and the wind stress curl is positive over the largest area for these same patterns. Patterns with easterly winds at Cape Farewell tend to have smaller fluxes in the Irminger Sea, but have a localized region of elevated fluxes just west of Cape Farewell in the Labrador Sea.

On average, over the open ocean the COARE turbulent fluxes calculated with either the WF or ERA-I atmospheric state data remove ~150 W m^{-2} from the ocean during the winter months. However, over the marginal ice zone (MIZ) the turbulent fluxes from WRF are much larger than from ERA-I. In the MIZ, the difference in sensible heat flux calculated with the WRF and ERA-I data is driven primarily by differences in the 2 m temperature between WRF and ERA-I, while differences in latent heat flux calculated with the WRF and ERA-I data are due to differences in both 2 m moisture and 10 m wind speed in WRF and ERA-I. Over the MIZ, WRF is particularly cold and dry at 2m when compared with ERA-I. The colder, drier air causes larger vertical temperature and moisture gradients, which then drive larger turbulent fluxes. Because WRF and ERA-I have the same surface conditions (sea surface temperature and sea ice fraction) and the differences in near-surface atmospheric state are largest over the MIZ, they are likely related to the differing treatment of sea ice thickness in each model. Both models assume constant sea ice thicknesses that are not appropriate for the southeast Greenland coast – WRF has 3 m ice and ERA-I has 1.5 m ice. WRF is colder and drier because when it calculates the near

surface atmospheric state the thick sea ice results in reduced energy input into the atmosphere. The resulting cold, dry biases highlight the importance of using an active sea ice model that predicts sea ice thickness and is able to calculate appropriate fluxes of energy to the atmosphere for varying sea ice thickness.

Therefore, the final chapter of this dissertation uses the fully coupled RASM model to address how the ocean mixed layer depth responds to different wind events when the atmosphere, ocean, and sea ice evolve together in a physically consistent manner. Using 20 winters of atmospheric data, the SOM algorithm was used to objectively identify 12 dominant wind patterns around southeastern Greenland. The oceanic buoyancy flux associated with each pattern was calculated, and each wind pattern was found to have buoyancy loss over all ocean grid points. The buoyancy loss is dominated by thermal terms, and haline contributions are several orders of magnitude smaller than thermal contributions. Of the thermal terms, the turbulent heat flux components have the largest contribution to buoyancy loss and spatially resemble the driving wind patterns. Radiative contributions to the thermal term, however, are relatively uniform for all wind patterns and smaller in magnitude than the turbulent contributions to the thermal term. The sensible heat flux is particularly important along the sea ice edge, while over the open ocean the sensible heat flux and latent heat fluxes are of similar magnitude. The largest sensible heat buoyancy loss is driven primarily by the near surface temperature anomaly, and strong winds then enhance the energy flux. The largest latent heat buoyancy loss occurs where both anomalously dry conditions and strong winds are co-located.

Patterns with northerly barrier flow have the largest buoyancy fluxes due to anomalously cold and dry air being advected over the open ocean. As a result, the ocean mixed layer depth (MLD) is anomalously deep for these patterns, and on interannual time scales MLD deepening is

positively correlated with these patterns' frequency. Westerly tip jets with barrier flow drive the largest buoyancy loss in both the Irminger and Labrador Seas, while easterly tip jets with barrier flow drive large buoyancy loss along the sea ice edge. All types of easterly tip jets drive local buoyancy loss west of Cape Farewell that may be important for convection if the ocean conditions are favorable. Additionally, because of the ocean's long memory the duration of events is important and events lasting 3 or more days cause larger magnitude MLD deepening.

While this dissertation has made important progress in determining how modeled wind events drive air-sea fluxes and are associated with deepening of the ocean MLD, there are still questions that remain to be answered. The mechanical effects of mesoscale winds on the deepening of the MLD have not been evaluated in detail, nor have subsurface ocean current influences on changes in MLD. In the future, ocean data from RASM will be compared to observations of the MLD in the Irminger and Labrador Seas to see how realistically RASM simulates the ocean behavior over the winter season.

Another outstanding question is how the state of ocean preconditioning impacts the ocean response to particular wind events. This question could be addressed by using RASM from a given spun up state and then simulating two parallel simulations that are forced by two different types of wind event for several days in a row. This experiment would help show the difference in how the ocean responds to different wind events, all else being equal. Additionally, exploring the transitions between different types of wind patterns could help to determine if a particular sequence of wind events leads to an especially large influence on the ocean response.

The first chapter of this dissertation showed that using atmospheric models with resolution of 10 km or higher is necessary to best simulate observed mesoscale wind events, but

subsequent chapters have used an atmospheric resolution of 50 km because it is the lowest resolution that can explicitly represent mesoscale winds and is computationally practical for multidecadal simulations. As computers become more powerful, upgrading RASM to use a 10 km atmosphere will be important to evaluate the ocean response to more realistic mesoscale winds. At 10 km it is possible to represent local sheltering effects from topography, katabatic wind drainage through glacial valleys, and higher wind speed maxima. Resolving the details of this region, which has land, ocean, and sea ice within such close proximity, is key to understanding the physical processes and exchanges between components of the Arctic system.

References

Abdalla, S., L. Isaksen, P. A. E. . Janssen, and N. Wedi (2013), Effective spectral resolution of ECMWF atmospheric forecast models, *ECMWF Newsl.*, *137*.

Ágústsson, H., and H. Ólafsson (2007), Simulating a severe windstorm in complex terrain, *Meteorol. Z.*, *16*(1), 111–122, doi:10.1127/0941-2948/2007/0169.

Bacon, S., W. J. Gould, and Y. Jia (2003), Open-ocean convection in the Irminger Sea, *Geophys. Res. Lett.*, *30*, 4 PP., doi:10.1029/2002GL016271.

Bakalian, F., S. Hameed, and R. S. Pickart (2007), Influence of the Icelandic Low latitude on the frequency of Greenland tip jet events: Implications for Irminger Sea convection, *J. Geophys. Res. Atmospheres*, *112*, doi:10.1029/2006JC003807.

Barstad, I., and S. Grønås (2005), Southwesterly flows over southern Norway—mesoscale sensitivity to large-scale wind direction and speed, *Tellus A*, *57*(2), 136–152, doi:10.1111/j.1600-0870.2005.00112.x.

Bourke, R. H., and R. P. Garrett (1987), Sea ice thickness distribution in the Arctic Ocean, *Cold Reg. Sci. Technol.*, *13*(3), 259–280, doi:10.1016/0165-232X(87)90007-3.

Broeke, V. D., M. R, and H. Gallée (2006), Observation and simulation of barrier winds at the western margin of the Greenland ice sheet, *Q. J. R. Meteorol. Soc.*, *122*(534), 1365–1383, doi:10.1002/qj.49712253407.

Bromwich, D., Y.-H. Kuo, M. Serreze, J. Walsh, L.-S. Bai, M. Barlage, K. Hines, and A. Slater (2010), Arctic System Reanalysis: Call for Community Involvement, *Eos Trans. Am. Geophys. Union*, *91*(2), 13–14, doi:10.1029/2010EO020001.

Bromwich, D. H., K. M. Hines, and L.-S. Bai (2009), Development and testing of Polar Weather Research and Forecasting model: 2. Arctic Ocean, *J. Geophys. Res.*, *114*, 22 PP., doi:200910.1029/2008JD010300.

Brunke, M. A., C. W. Fairall, X. Zeng, L. Eymard, and J. A. Curry (2003), Which Bulk Aerodynamic Algorithms are Least Problematic in Computing Ocean Surface Turbulent Fluxes?, *J. Clim.*, *16*(4), 619–635, doi:10.1175/1520-0442(2003)016<0619:WBAAAL>2.0.CO;2.

Cassano, E. N., J. M. Glisan, J. J. Cassano, W. J. G. Jr, and M. W. Seefeldt (2015), Self-organizing map analysis of widespread temperature extremes in Alaska and Canada, *Clim. Res.*, *62*(3), 199–218, doi:10.3354/cr01274.

Cassano, J. J., P. Uotila, A. H. Lynch, and E. N. Cassano (2007), Predicted changes in synoptic forcing of net precipitation in large Arctic river basins during the 21st century, *J. Geophys. Res. Biogeosciences*, *112*(G4), doi:10.1029/2006JG000332.

Cassano, J. J., M. Higgins, and M. Seefeldt (2011), Performance of the Weather Research and Forecasting (WRF) Model for Month-long pan-Arctic Simulations, *Mon. Weather Rev.*, doi:10.1175/MWR-D-10-05065.1.

Charnock, H. (1955), Wind stress on a water surface, *Q. J. R. Meteorol. Soc.*, *81*(350), 639–640, doi:10.1002/qj.49708135027.

Chen, F., and J. Dudhia (2001), Coupling an Advanced Land Surface–Hydrology Model with the Penn State–NCAR MM5 Modeling System. Part I: Model Implementation and Sensitivity, *Mon. Weather Rev.*, *129*(4), 569–585, doi:10.1175/1520-0493(2001)129<0569:CAALSH>2.0.CO;2.

Clarke, R. A., and J.-C. Gascard (1983), The Formation of Labrador Sea Water. Part I: Large-Scale Processes, *J. Phys. Oceanogr.*, *13*(10), 1764–1778, doi:10.1175/1520-0485(1983)013<1764:TFOLSW>2.0.CO;2.

Colle, B. A., K. A. Loescher, G. S. Young, and N. S. Winstead (2006), Climatology of Barrier Jets along the Alaskan Coast. Part II: Large-Scale and Sounding Composites, *Mon. Weather Rev.*, *134*(2), 454–477, doi:10.1175/MWR3038.1.

Collins, W. D., P. J. Rasch, B. A. Boville, J. J. Hack, J. R. McCaa, D. L. Williamson, J. T. Kiehl, B. Briegleb, C. Bitz, and S. J. Lin (2004), Description of the NCAR community atmosphere model (CAM 3.0), *NCAR Tech Note NCARTN-464 STR*, 226.

Comiso, J. (2008), Bootstrap Sea Ice Concentrations from Nimbus-7 SMMR and DMSP SSM/I, [Jan-Mar 2007],

Condron, A., and I. A. Renfrew (2013), The impact of polar mesoscale storms on northeast Atlantic Ocean circulation, *Nat. Geosci.*, *6*(1), 34–37, doi:10.1038/ngeo1661.

Craig, A. P., M. Vertenstein, and R. Jacob (2012), A new flexible coupler for earth system modeling developed for CCSM4 and CESM1, *Int. J. High Perform. Comput. Appl.*, *26*(1), 31–42, doi:10.1177/1094342011428141.

Cushman-Roisin, B., and J.-M. Beckers (2011), *Introduction to Geophysical Fluid Dynamics: Physical and Numerical Aspects*, Academic Press.

Dee, D. P. et al. (2011), The ERA-Interim reanalysis: configuration and performance of the data assimilation system, *Q. J. R. Meteorol. Soc.*, *137*(656), 553–597, doi:10.1002/qj.828.

Doyle, J. D., and M. A. Shapiro (1999), Flow response to large-scale topography: the Greenland tip jet, *Tellus A*, *51*(5), 728–748.

Dudhia, J. (2010), WRF Physics Options, WRF tutorial. Boulder, CO.

Dunbar, R. S., and K. L. Perry (2001), SeaWinds on QuikSCAT Level 3 Daily, Gridded Ocean Wind Vectors (JPL SeaWinds Project) Version 1.1, *JPL Doc. -20335 Jet Propuls. Lab. Pasadena CA*.

DuVivier, A. K., and J. J. Cassano (2013), Evaluation of WRF Model Resolution on Simulated Mesoscale Winds and Surface Fluxes near Greenland, *Mon. Weather Rev.*, *141*(3), 941–963, doi:10.1175/MWR-D-12-00091.1.

DuVivier, A. K., and J. J. Cassano (2014), Exploration of turbulent heat fluxes and wind stress curl in WRF and ERA-Interim during wintertime mesoscale wind events around southeastern Greenland, *J. Geophys. Res.-Atmospheres - Accepted.*

DuVivier, A. K., and J. J. Cassano (2015), Comparison of wintertime mesoscale winds over the ocean around southeastern Greenland in WRF and ERA-Interim, *Clim. Dyn. - Submitt.*

Dyer, A. J., and B. B. Hicks (1970), Flux-gradient relationships in the constant flux layer, *Q. J. R. Meteorol. Soc.*, *96*(410), 715–721, doi:10.1002/qj.49709641012.

ECMWF (2007), *IFS documentation CY31r1*, European Centre for Medium-Range Weather Forecasts, Shinfield Park, Reading, England.

Fairall, C. W., A. A. Grachev, A. J. Bedard, and R. T. Nishiyama (1996), *Wind, Wave, Stress, and Surface Roughness Relationships from Turbulence Measurements Mad on R/P Flip in the SCOPE Experiment*, NOAA Technical Memorandum ERL, Environmental Technology Laboratory, Boulder, CO.

Fairall, C. W., E. F. Bradley, J. E. Hare, A. A. Grachev, and J. B. Edson (2003), Bulk Parameterization of Air–Sea Fluxes: Updates and Verification for the COARE Algorithm, *J. Clim.*, *16*, 571–591, doi:10.1175/1520-0442(2003)016<0571:BPOASF>2.0.CO;2.

Gascard, J.-C., and R. A. Clarke (1983), The formation of Labrador Sea water. II: Mesoscale and smaller-scale processes, *J. Phys. Oceanogr.*, *13*(10), 1779–1797, doi:10.1175/1520-0485(1983)013<1779:TFOLSW>2.0.CO;2.

Grell, G. A., and D. Dévényi (2002), A generalized approach to parameterizing convection combining ensemble and data assimilation techniques, *Geophys. Res. Lett.*, *29*(14), 38–1, doi:10.1029/2002GL015311.

Griffies, S. M., M. Winton, B. Samuels, G. Danabasoglu, S. Yeager, S. Marsland, H. Drange, and M. Bentsen (2012), *Datasets and protocol for the CLIVAR WGOMD Coordinated Ocean-sea ice Reference Experiments (COREs)*, WCRP Report.

Haas, C., A. Pfaffling, S. Hendricks, L. Rabenstein, J.-L. Etienne, and I. Rigor (2008), Reduced ice thickness in Arctic Transpolar Drift favors rapid ice retreat, *Geophys. Res. Lett.*, *35*(17), L17501, doi:10.1029/2008GL034457.

Haine, T. W. N., S. Zhang, G. W. K. Moore, and I. A. Renfrew (2009), On the impact of high-resolution, high-frequency meteorological forcing on Denmark Strait ocean circulation, *Q. J. R. Meteorol. Soc.*, *135*, 2067–2085, doi:10.1002/qj.505.

Harden, B. E., and I. A. Renfrew (2012), On the spatial distribution of high winds off southeast Greenland, *Geophys. Res. Lett.*, *39*(14), L14806, doi:10.1029/2012GL052245.

Harden, B. E., I. A. Renfrew, and G. N. Petersen (2011), A Climatology of Wintertime Barrier Winds off Southeast Greenland, *J. Clim.*, *24*, 4701–4717, doi:10.1175/2011JCLI4113.1.

Heorton, H. D. B. S., D. L. Feltham, and J. C. R. Hunt (2014), The Response of the Sea Ice Edge to Atmospheric and Oceanic Jet Formation, *J. Phys. Oceanogr.*, *44*(9), 2292–2316, doi:10.1175/JPO-D-13-0184.1.

Hewitson, B. C., and R. G. Crane (2002), Self-organizing maps: applications to synoptic climatology, *Clim. Res.*, *22*(1), 13–26, doi:10.3354/cr022013.

Higgins, M. E., and J. J. Cassano (2009), Impacts of reduced sea ice on winter Arctic atmospheric circulation, precipitation, and temperature, *J. Geophys. Res. Atmospheres*, *114*(D16), doi:10.1029/2009JD011884.

Hines, K. M., D. H. Bromwich, L. Bai, C. M. Bitz, J. G. Powers, and K. W. Manning (2015), Sea Ice Enhancements to Polar WRF, *Mon. Weather Rev.*, doi:10.1175/MWR-D-14-00344.1.

Holton, J. R. (2004), *An introduction to dynamic meteorology*, 4th Edition., Elsevier Academic Press, Burlington, MA.

Hong, S.-Y., Y. Noh, and J. Dudhia (2006), A New Vertical Diffusion Package with an Explicit Treatment of Entrainment Processes, *Mon. Weather Rev.*, *134*(9), 2318–2341, doi:10.1175/MWR3199.1.

Hughes, M., and J. J. Cassano (2015), The climatological distribution of extreme Arctic winds, and implications for ocean and sea ice processes, *J. Geophys. Res.-Atmospheres - Submitt.*

Hunke, E. C. (2010), Thickness sensitivities in the CICE sea ice model, *Ocean Model.*, *34*(3–4), 137–149, doi:10.1016/j.ocemod.2010.05.004.

Hunke, E. C., and M. M. Holland (2007), Global atmospheric forcing data for Arctic ice-ocean modeling, *J. Geophys. Res.*, *112*(C4), C04S14, doi:10.1029/2006JC003640.

Hunke, E. C., and W. H. Lipscomb (2010), CICE: the Los Alamos Sea Ice Model Documentation and Software User's Manual Version 5.0 LA-CC-06-012, *Los Alamos Natl. Lab. Los Alamos NM*, *87545*, 115.

Iacono, M. J., J. S. Delamere, E. J. Mlawer, M. W. Shephard, S. A. Clough, and W. D. Collins (2008), Radiative forcing by long-lived greenhouse gases: Calculations with the AER radiative transfer models, *J. Geophys. Res.*, *113*(D13), doi:10.1029/2008JD009944.

De Jong, M. F., H. M. van Aken, K. Våge, and R. S. Pickart (2012), Convective mixing in the central Irminger Sea: 2002–2010, *Deep Sea Res. Part Oceanogr. Res. Pap.*, *63*, 36–51, doi:10.1016/j.dsr.2012.01.003.

Jung, T., S. Serrar, and Q. Wang (2014), The oceanic response to mesoscale atmospheric forcing, *Geophys. Res. Lett.*, 1–6, doi:10.1002/2013GL059040.

Killworth, P. D. (1983), Deep convection in the World Ocean, *Rev. Geophys.*, *21*(1), 1–26, doi:10.1029/RG021i001p00001.

Kilpeläinen, T., T. Vihma, and H. Ólafsson (2011), Modelling of spatial variability and topographic effects over Arctic fjords in Svalbard, *Tellus A*, *63*(2), 223–237, doi:10.1111/j.1600-0870.2010.00481.x.

Kohonen, T. (2001), *Self-Organizing Maps*, 3rd ed., Springer, New York.

Kolstad, E. (2008), A QuikSCAT climatology of ocean surface winds in the Nordic seas: Identification of features and comparison with the NCEP/NCAR reanalysis, *J Geophys Res*, *113*, D11106, doi:10.1029/2007JD008918.

Kwok, R., E. C. Hunke, W. Maslowski, D. Menemenlis, and J. Zhang (2008), Variability of sea ice simulations assessed with RGPS kinematics, *J. Geophys. Res.*, *113*(C11), C11012, doi:10.1029/2008JC004783.

Large, W. G., and S. G. Yeager (2009), The global climatology of an interannually varying air–sea flux data set, *Clim. Dyn.*, *33*(2-3), 341–364, doi:10.1007/s00382-008-0441-3.

Large, W. G., J. C. McWilliams, and S. C. Doney (1994), Oceanic vertical mixing: A review and a model with a nonlocal boundary layer parameterization, *Rev. Geophys.*, *32*(4), 363–403, doi:10.1029/94RG01872.

Lavender, K. L., R. E. Davis, and W. B. Owens (2002), Observations of Open-Ocean Deep Convection in the Labrador Sea from Subsurface Floats*, *J. Phys. Oceanogr.*, *32*(2), 511–526, doi:10.1175/1520-0485(2002)032<0511:OOOODC>2.0.CO;2.

Lindsay, R., M. Wensnahan, A. Schweiger, and J. Zhang (2014), Evaluation of Seven Different Atmospheric Reanalysis Products in the Arctic*, *J. Clim.*, *27*(7), 2588–2606, doi:10.1175/JCLI-D-13-00014.1.

Lisæter, K. A., G. Evensen, and S. Laxon (2007), Assimilating synthetic CryoSat sea ice thickness in a coupled ice-ocean model, *J. Geophys. Res. Oceans*, *112*(C7), doi:10.1029/2006JC003786.

Liu, Y., R. H. Weisberg, and R. He (2006), Sea Surface Temperature Patterns on the West Florida Shelf Using Growing Hierarchical Self-Organizing Maps, *J. Atmospheric Ocean. Technol.*, *23*(2), 325–338, doi:10.1175/JTECH1848.1.

Loescher, K. A., G. S. Young, B. A. Colle, and N. S. Winstead (2006), Climatology of Barrier Jets along the Alaskan Coast. Part I: Spatial and Temporal Distributions, *Mon. Weather Rev.*, *134*(2), 437–453, doi:10.1175/MWR3037.1.

Marshall, J., and A. Plumb (2007), *Atmosphere, Ocean and Climate Dynamics: An Introductory Text: 93*, 1 edition., Academic Press.

Marshall, J., and F. Schott (1999), Open-ocean convection: Observations, theory, and models, *Rev. Geophys.*, *37*(1), 1–64, doi:10.1029/98RG02739.

Martin, R., and G. W. K. Moore (2007), Air-sea interaction associated with a Greenland reverse tip jet, *Geophys. Res. Lett.*, *34*, 5 PP., doi:10.1029/2007GL031093.

Moore, G., and I. Renfrew (2005), Tip jets and barrier winds: A QuikSCAT climatology of high wind speed events around Greenland, *J. Clim.*, *18*(18), 3713–3725, doi:10.1175/JCLI3455.1.

Moore, G. W. K. (2003), Gale force winds over the Irminger Sea to the east of Cape Farewell, Greenland, *Geophys. Res. Lett.*, *30*, 4 PP., doi:10.1029/2003GL018012.

Moore, G. W. K. (2012), A new look at Greenland flow distortion and its impact on barrier flow, tip jets and coastal oceanography, *Geophys. Res. Lett.*, *39*(22), L22806, doi:10.1029/2012GL054017.

Moore, G. W. K. (2014), Mesoscale Structure of Cape Farewell Tip Jets, *J. Clim.*, *27*(23), 8956–8965, doi:10.1175/JCLI-D-14-00299.1.

Moore, G. W. K., and I. A. Renfrew (2014), A new look at Southeast Greenland barrier winds and katabatic flow, *US CLIVAR Var.*, *12*(2).

Moore, G. W. K., R. S. Pickart, and I. A. Renfrew (2008), Buoy observations from the windiest location in the world ocean, Cape Farewell, Greenland, *Geophys. Res. Lett.*, *35*, doi:10.1029/2008GL034845.

Moore, G. W. K., R. S. Pickart, and I. A. Renfrew (2011), Complexities in the climate of the subpolar North Atlantic: a case study from the winter of 2007, *Q. J. R. Meteorol. Soc.*, *137*(656), 757–767, doi:10.1002/qj.778.

Morrison, H., G. Thompson, and V. Tatarskii (2009), Impact of Cloud Microphysics on the Development of Trailing Stratiform Precipitation in a Simulated Squall Line: Comparison of One- and Two-Moment Schemes, *Mon. Weather Rev.*, *137*(3), 991–1007, doi:10.1175/2008MWR2556.1.

Nigro, M. A., J. J. Cassano, M. A. Lazzara, and L. M. Keller (2012), Case Study of a Barrier Wind Corner Jet off the Coast of the Prince Olav Mountains, Antarctica, *Mon. Weather Rev.*, *140*(7), 2044–2063, doi:10.1175/MWR-D-11-00261.1.

Ólafsson, H., and H. Ágústsson (2009), Gravity wave breaking in easterly flow over Greenland and associated low level barrier- and reverse tip-jets, *Meteorol. Atmospheric Phys.*, *104*, 191–197, doi:10.1007/s00703-009-0024-9.

Oltmanns, M., F. Straneo, G. W. K. Moore, and S. H. Mernild (2014), Strong Downslope Wind Events in Ammassalik, Southeast Greenland, *J. Clim.*, *27*(3), 977–993, doi:10.1175/JCLI-D-13-00067.1.

Outten, S. D., I. A. Renfrew, and G. N. Petersen (2009), An easterly tip jet off Cape Farewell, Greenland. II: Simulations and dynamics, *Q. J. R. Meteorol. Soc.*, *135*, 1934–1949, doi:10.1002/qj.531.

Parish, T. R. (1982), Barrier Winds Along the Sierra Nevada Mountains, *J. Appl. Meteorol.*, *21*, 925–930, doi:10.1175/1520-0450(1982)021<0925:BWATSN>2.0.CO;2.

Parish, T. R. (n.d.), The Influence of the Antarctic Peninsula on the Wind Field Over the Western Weddell Sea, *J. Geophys. Res.*, *88*(C4), PP. 2684–2692, doi:198310.1029/JC088iC04p02684.

Paulson, C. A. (1970), The Mathematical Representation of Wind Speed and Temperature Profiles in the Unstable Atmospheric Surface Layer, *J. Appl. Meteorol.*, *9*(6), 857–861, doi:10.1175/1520-0450(1970)009<0857:TMROWS>2.0.CO;2.

Petersen, G. N., and I. A. Renfrew (2009), Aircraft-based observations of air-sea fluxes over Denmark Strait and the Irminger Sea during high wind speed conditions, *Q. J. R. Meteorol. Soc.*, *135*, 2030–2045, doi:10.1002/qj.355.

Petersen, G. N., J. E. Kristjánsson, and H. Ólafsson (2004), Numerical simulations of Greenland's impact on the Northern Hemisphere winter circulation, *Tellus A*, *56*(2), 102–111, doi:10.1111/j.1600-0870.2004.00047.x.

Petersen, G. N., I. A. Renfrew, and G. W. K. Moore (2009), An overview of barrier winds off southeastern Greenland during the Greenland Flow Distortion experiment, *Q. J. R. Meteorol. Soc.*, *135*, 1950–1967, doi:10.1002/qj.455.

Pickart, R. S., M. A. Spall, M. H. Ribergaard, G. Moore, and R. F. Milliff (2003a), Deep convection in the Irminger Sea forced by the Greenland tip jet, *Nature*, *424*(6945), 152–156, doi:10.1038/nature01729.

Pickart, R. S., F. Straneo, and G. Moore (2003b), Is Labrador Sea Water formed in the Irminger basin?, *Deep Sea Res. Part Oceanogr. Res. Pap.*, *50*(1), 23–52.

Pickart, R. S., K. Våge, G. Moore, I. A. Renfrew, M. H. Ribergaard, and H. C. Davies (2008), Convection in the western North Atlantic subpolar gyre: Do small-scale wind events matter, in *Arctic-subarctic ocean fluxes: defining the role of the northern seas in climate*, edited by R. R. Dickson, J. Meincke, and P. B. Rhines, pp. 629–652, Springer: Dordrecht, The Netherlands.

Reeve, M. A., and E. W. Kolstad (2011), The Spitsbergen South Cape tip jet, *Q. J. R. Meteorol. Soc.*, *137*(660), 1739–1748, doi:10.1002/qj.876.

Renfrew, I. A., and G. W. K. Moore (1999), An extreme cold-air outbreak over the Labrador Sea: Roll vortices and air-sea interaction, *Mon. Weather Rev.*, *127*(10), 2379–2394.

Renfrew, I. A., G. Moore, P. S. Guest, and K. Bumke (2002), A comparison of surface layer and surface turbulent flux observations over the Labrador Sea with ECMWF analyses and NCEP reanalyses, *J. Phys. Oceanogr.*, *32*(2), 383–400, doi:10.1175/1520-0485(2002)032<0383:ACOSLA>2.0.CO;2.

Renfrew, I. A. et al. (2008), The Greenland Flow Distortion Experiment, *Bull. Am. Meteorol. Soc.*, *89*, 1307–1324, doi:10.1175/2008BAMS2508.1.

Renfrew, I. A., G. N. Petersen, D. A. J. Sproson, G. W. K. Moore, H. Adiwidjaja, S. Zhang, and R. North (2009a), A comparison of aircraft-based surface-layer observations over Denmark Strait and the Irminger Sea with meteorological analyses and QuikSCAT winds, *Q. J. R. Meteorol. Soc.*, *135*, 2046–2066, doi:10.1002/qj.444.

Renfrew, I. A., S. D. Outten, and G. W. K. Moore (2009b), An easterly tip jet off Cape Farewell, Greenland. I: Aircraft observations, *Q. J. R. Meteorol. Soc.*, *135*, 1919–1933, doi:10.1002/qj.513.

Reusch, D. B., R. B. Alley, and B. C. Hewitson (2005), Relative Performance of Self-Organizing Maps and Principal Component Analysis in Pattern Extraction from Synthetic Climatological Data, *Polar Geogr.*, *29*(3), 188–212, doi:10.1080/789610199.

Roberts, A., J. J. Cassano, R. Doscher, L. Hinzman, M. M. Holland, H. Mitsudera, A. Sumi, and J. E. Walsh (2010), A Science Plan for Regional Arctic System Modeling: A report by the Arctic Research Community for hte National Science Foundation Office of Polar Programs, *Tech Pap 10-0001 Int. Arct. Res. Cent.*

Roberts, A., A. Craig, W. Maslowski, R. Osinski, A. DuVivier, M. Hughes, B. Nijssen, J. Cassano, and M. Brunke (2015), Simulating transient ice–ocean Ekman transport in the Regional Arctic System Model and Community Earth System Model, *Ann. Glaciol.*, *56*(69), 211–228, doi:10.3189/2015AoG69A760.

Sampe, T., and S.-P. Xie (2007), Mapping High Sea Winds from Space: A Global Climatology, *Bull. Am. Meteorol. Soc.*, *88*, 1965–1978, doi:10.1175/BAMS-88-12-1965.

Serreze, M. C., A. P. Barrett, A. G. Slater, M. Steele, J. Zhang, and K. E. Trenberth (2007), The large-scale energy budget of the Arctic, *J Geophys Res*, *112*, D11122.

Sheridan, S. C., and C. C. Lee (2011), The self-organizing map in synoptic climatological research, *Prog. Phys. Geogr.*, *35*, 109–119, doi:10.1177/0309133310397582.

Shkolnik, I. M., and S. V. Efimov (2013), Cyclonic activity in high latitudes as simulated by a regional atmospheric climate model: added value and uncertainties, *Environ. Res. Lett.*, *8*(4), 045007, doi:10.1088/1748-9326/8/4/045007.

Skamarock, W. C. (2004), Evaluating Mesoscale NWP Models Using Kinetic Energy Spectra, *Mon. Weather Rev.*, *132*, 3019–3032, doi:10.1175/MWR2830.1.

Skamarock, W. C., J. B. Klemp, J. Dudhia, D. Gill, D. M. Barker, M. G. Duda, X.-Y. Huang, W. Wang, and J. G. Powers (2008), *A Description of the Advanced Research WRF Version 3 (NCAR Technical Note)*, NCAR: Mesoscale and Microscale Meteorology Division.

Smith, S. A., J. D. Doyle, A. R. Brown, and S. Webster (2006), Sensitivity of resolved mountain drag to model resolution for MAP case-studies, *Q. J. R. Meteorol. Soc.*, *132*(618), 1467–1487, doi:10.1256/qj.05.67.

Smith, S. D. (1988), Coefficients for Sea Surface Wind Stress, Heat Flux, and Wind Profiles as a Function of Wind Speed and Temperature, *J. Geophys. Res.*, *93*(C12), PP. 15,467–15,472, doi:198810.1029/JC093iC12p15467.

Spall, M. A., and R. S. Pickart (2003), Wind-Driven Recirculations and Exchange in the Labrador and Irminger Seas*, *J. Phys. Oceanogr.*, *33*(8), 1829–1845, doi:10.1175/2384.1.

Sproson, D. A. J., I. A. Renfrew, and K. J. Heywood (2008), Atmospheric conditions associated with oceanic convection in the south-east Labrador Sea, *Geophys. Res. Lett.*, *35*(6), doi:10.1029/2007GL032971.

Sproson, D. A. J., I. A. Renfrew, and K. J. Heywood (2010), A parameterization of Greenland's tip jets suitable for ocean or coupled climate models, *J. Geophys. Res. Oceans*, *115*, doi:10.1029/2009JC006002.

Stroeve, J. C., M. C. Serreze, M. M. Holland, J. E. Kay, J. Malanik, and A. P. Barrett (2011), The Arctic's rapidly shrinking sea ice cover: a research synthesis, *Clim. Change*, *110*, 1005–1027, doi:10.1007/s10584-011-0101-1.

Strong, C., and I. G. Rigor (2013), Arctic marginal ice zone trending wider in summer and narrower in winter, *Geophys. Res. Lett.*, doi:10.1002/grl.50928.

Tao, W.-K., and J. Simpson (1993), Goddard Cumulus Ensemble Model. Part I: Model Description, *Terr. Atmospheric Ocean. Sci.*, *4*(1), 35–71.

Tilinina, N., S. K. Gulev, and D. H. Bromwich (2014), New View of Arctic Cyclone Activity from the Arctic System Reanalysis, *Geophys. Res. Lett.*, doi:10.1002/2013GL058924.

Tsukernik, M., D. N. Kindig, and M. C. Serreze (2007), Characteristics of winter cyclone activity in the northern North Atlantic: Insights from observations and regional modeling, *J Geophys Res*, *112*, D03–101.

Våge, K., R. S. Pickart, V. Thierry, G. Reverdin, C. M. Lee, B. Petrie, T. A. Agnew, A. Wong, and M. H. Ribergaard (2008a), Surprising return of deep convection to the subpolar North Atlantic Ocean in winter 2007–2008, *Nat. Geosci.*, *2*, 67–72, doi:10.1038/ngeo382.

Våge, K., R. S. Pickart, G. W. K. Moore, and M. H. Ribergaard (2008b), Winter Mixed Layer Development in the Central Irminger Sea: The Effect of Strong, Intermittent Wind Events, *J. Phys. Oceanogr.*, *38*, 541–565, doi:10.1175/2007JPO3678.1.

Våge, K., T. Spengler, H. C. Davies, and R. S. Pickart (2009), Multi-event analysis of the westerly Greenland tip jet based upon 45 winters in ERA-40, *Q. J. R. Meteorol. Soc.*, *135*, doi:10.1002/qj.488.

Våge, K., R. S. Pickart, M. A. Spall, H. Valdimarsson, S. Jónsson, D. J. Torres, S. Østerhus, and T. Eldevik (2011a), Significant role of the North Icelandic Jet in the formation of Denmark Strait overflow water, *Nat. Geosci.*, *4*, 723–727, doi:10.1038/ngeo1234.

Våge, K., R. S. Pickart, A. Sarafanov, Ø. Knutsen, H. Mercier, P. Lherminier, H. M. van Aken, J. Meincke, D. Quadfasel, and S. Bacon (2011b), The Irminger Gyre: Circulation, convection, and interannual variability, *Deep Sea Res. Part Oceanogr. Res. Pap.*, *58*(5), 590–614, doi:10.1016/j.dsr.2011.03.001.

Våge, K., R. S. Pickart, M. A. Spall, G. W. K. Moore, H. Valdimarsson, D. J. Torres, S. Y. Erofeeva, and J. E. Ø. Nilsen (2013), Revised circulation scheme north of the Denmark Strait, *Deep Sea Res. Part Oceanogr. Res. Pap.*, *79*, 20–39, doi:10.1016/j.dsr.2013.05.007.

Webb, E. K. (1970), Profile relationships: The log-linear range, and extension to strong stability, *Q. J. R. Meteorol. Soc.*, *96*(407), 67–90, doi:10.1002/qj.49709640708.

Zhang, J., R. Lindsay, M. Steele, and A. Schweiger (2008), What drove the dramatic retreat of arctic sea ice during summer 2007?, *Geophys. Res. Lett.*, *35*(11), L11505, doi:10.1029/2008GL034005.

Supplementary Figures

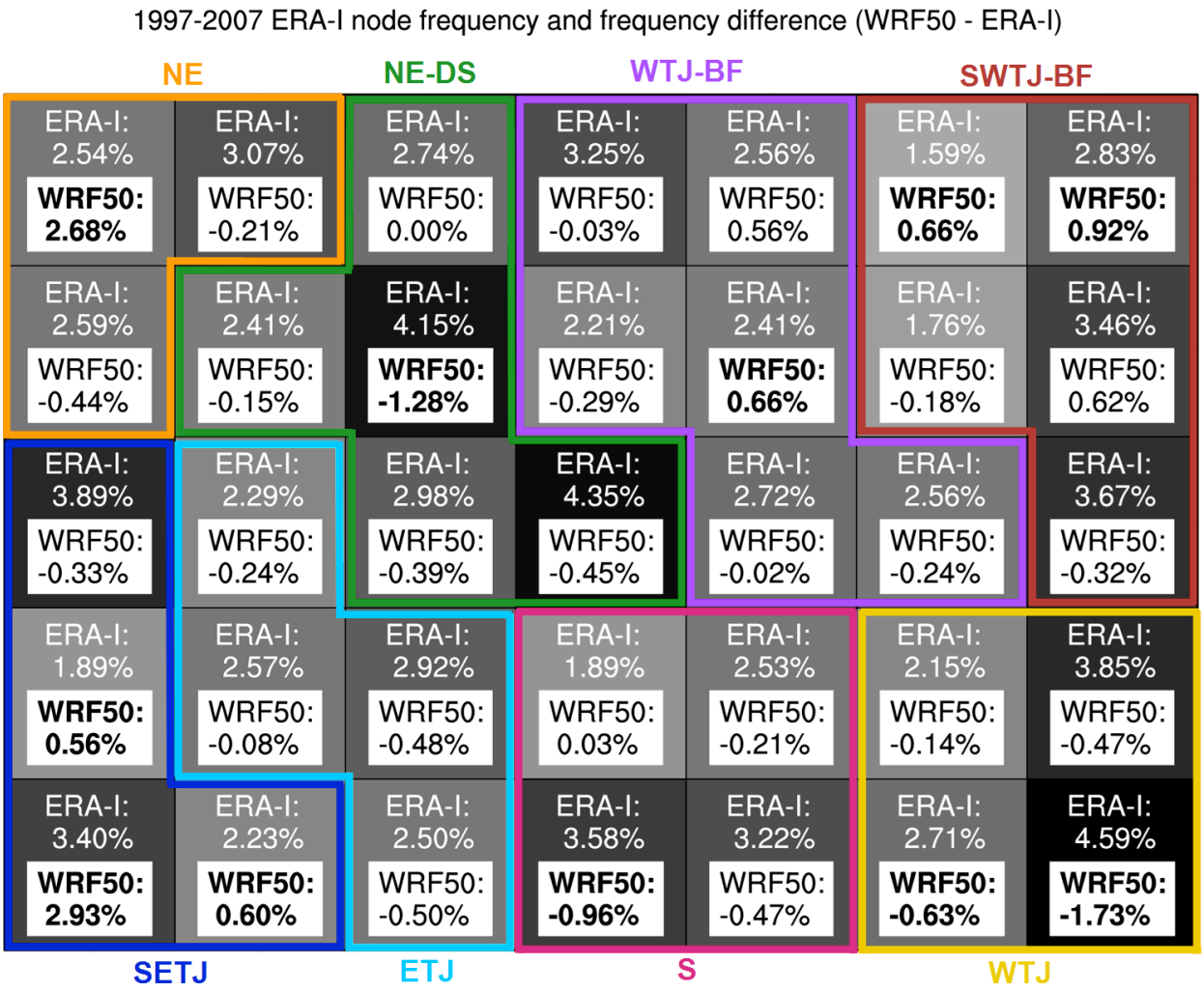

Supplementary Figure 1: 1997-2007 winter (NDJFM) (a) ERA-I pattern frequencies and group frequency difference (WRF50-ERA). Grey shading indicates the relative ERA-I frequency for each pattern; the difference in group frequency between WRF50 and ERA-I is shown below the ERA-I frequency and bold text indicates statistically significant differences. Colored lines around the patterns and labels at the top and bottom of the SOM indicate groupings mentioned in the text.

1997-2007 ERA-I and WRF50 correlation with the NAO monthly index

NE		NE-DS	WTJ-BF		SWTJ-BF	
ERA-I: -0.41 WRF50: -0.29	ERA-I: -0.30 WRF50: -0.30	ERA-I: **-0.24** WRF50: **0.03**	ERA-I: **0.21** WRF50: 0.27	ERA-I: **0.19** WRF50: **-0.03**	ERA-I: 0.27 WRF50: 0.32	ERA-I: 0.49 WRF50: 0.40
ERA-I: -0.48 WRF50: **-0.25**	ERA-I: **0.01** WRF50: -0.32	ERA-I: **0.14** WRF50: **0.15**	ERA-I: 0.33 WRF50: **-0.09**	ERA-I: **0.25** WRF50: **0.20**	ERA-I: 0.34 WRF50: **0.15**	ERA-I: 0.46 WRF50: 0.55
ERA-I: -0.50 WRF50: -0.50	ERA-I: -0.31 WRF50: **-0.25**	ERA-I: **-0.09** WRF50: **0.12**	ERA-I: **0.21** WRF50: 0.35	ERA-I: **-0.08** WRF50: **0.12**	ERA-I: **0.06** WRF50: **0.05**	ERA-I: **0.26** WRF50: 0.46
ERA-I: -0.41 WRF50: -0.27	ERA-I: -0.50 WRF50: -0.29	ERA-I: **-0.03** WRF50: **-0.16**	ERA-I: **0.02** WRF50: **0.10**	ERA-I: **-0.01** WRF50: **0.07**	ERA-I: **0.12** WRF50: **0.13**	ERA-I: 0.46 WRF50: 0.37
ERA-I: **-0.08** WRF50: **-0.12**	ERA-I: **-0.20** WRF50: -0.32	ERA-I: **-0.23** WRF50: -0.28	ERA-I: **-0.05** WRF50: **-0.02**	ERA-I: **0.07** WRF50: **0.05**	ERA-I: **0.18** WRF50: **0.04**	ERA-I: **0.23** WRF50: **0.24**
SETJ		ETJ	S		WTJ	

Supplementary Figure 2: 1997-2007 winter (NDJFM) correlation between ERA-I and WRF50 pattern frequency and NAO monthly index. Bold text indicates correlations that are statistically significant at the 95% level. Colored lines around the patterns and labels at the top and bottom of the SOM indicate groupings mentioned in the text.

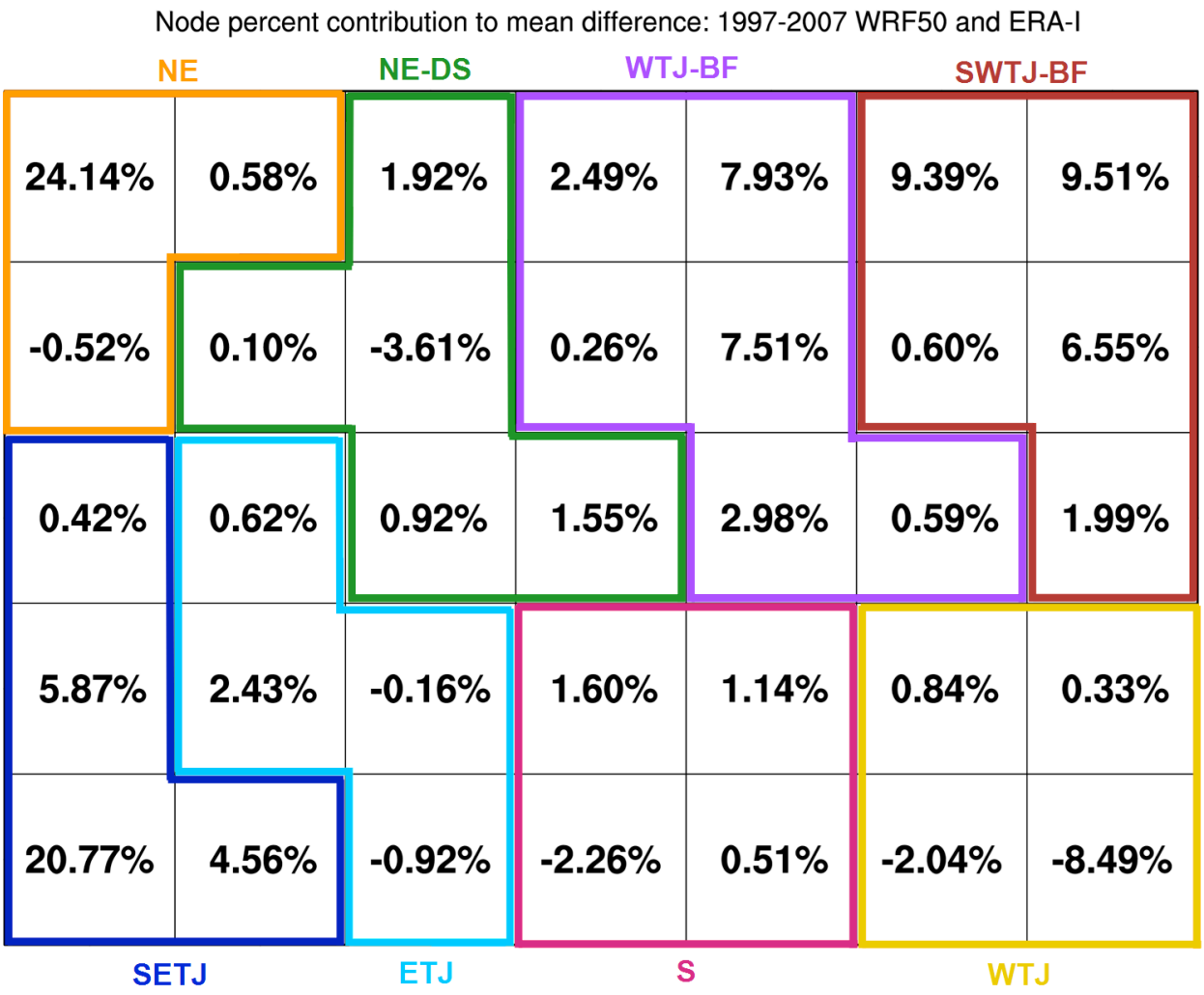

Supplementary Figure 3: 1997-2007 winter (NDJFM) pattern percent (%) contribution to the mean wind speed difference between WRF50 and ERA-I. Colored lines around the patterns and labels at the top and bottom of the SOM indicate groupings mentioned in the text.

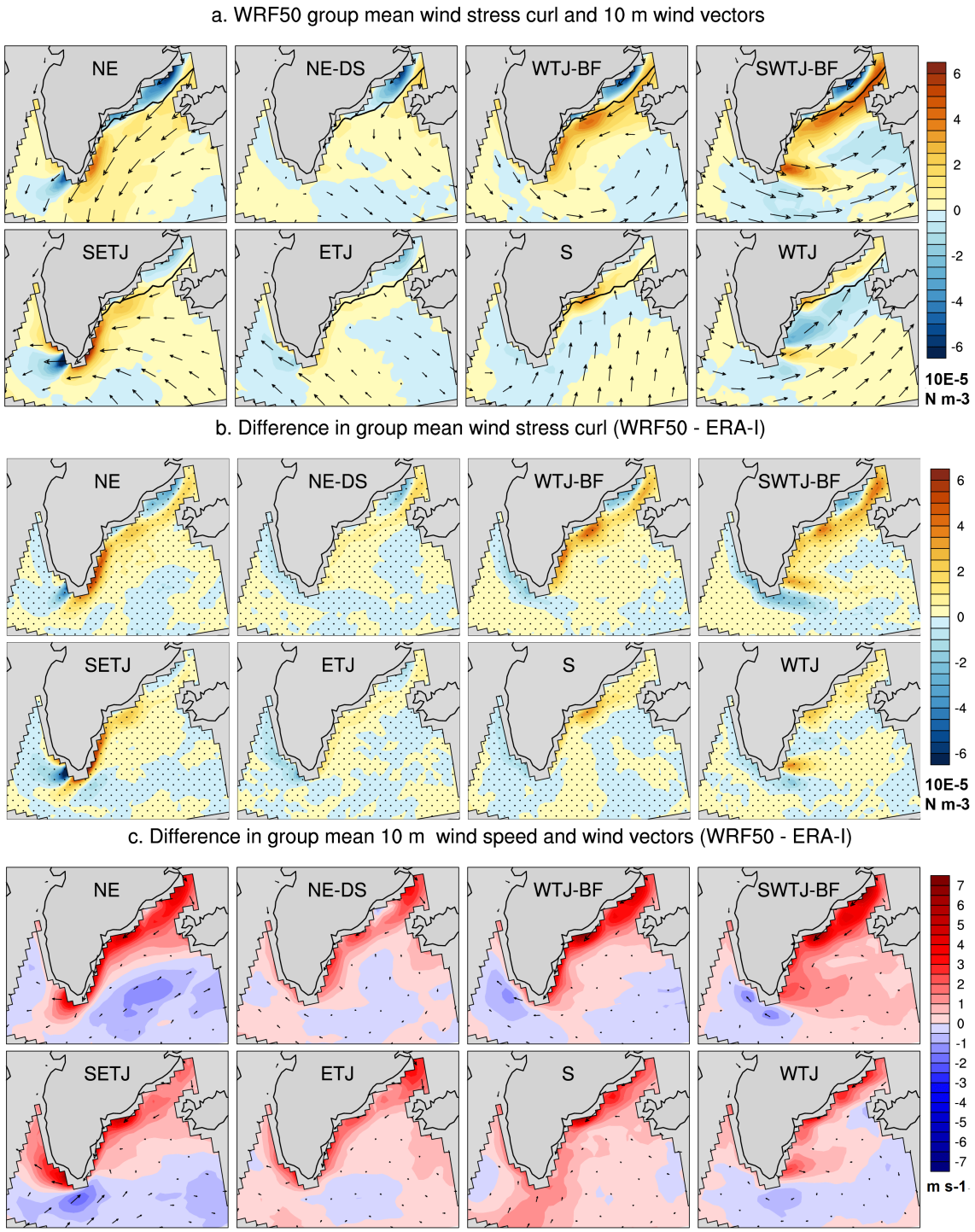

Supplementary Figure 4: Group (a) WRF wind stress curl (10^{-5} N m^{-3}) and wind speed vectors, (b) difference in WRF and ERA-I wind stress curl, and (c) WRF and ERA-I 10 m wind speed (m s^{-1}) and wind vector difference. The dark black contour on the mean figures is the 15% sea ice concentration line and the MIZ is located between the 15% sea ice contour and the Greenland coast. Stippling on the difference figures indicates areas with statistically significant difference between the two datasets at the 95% confidence level.

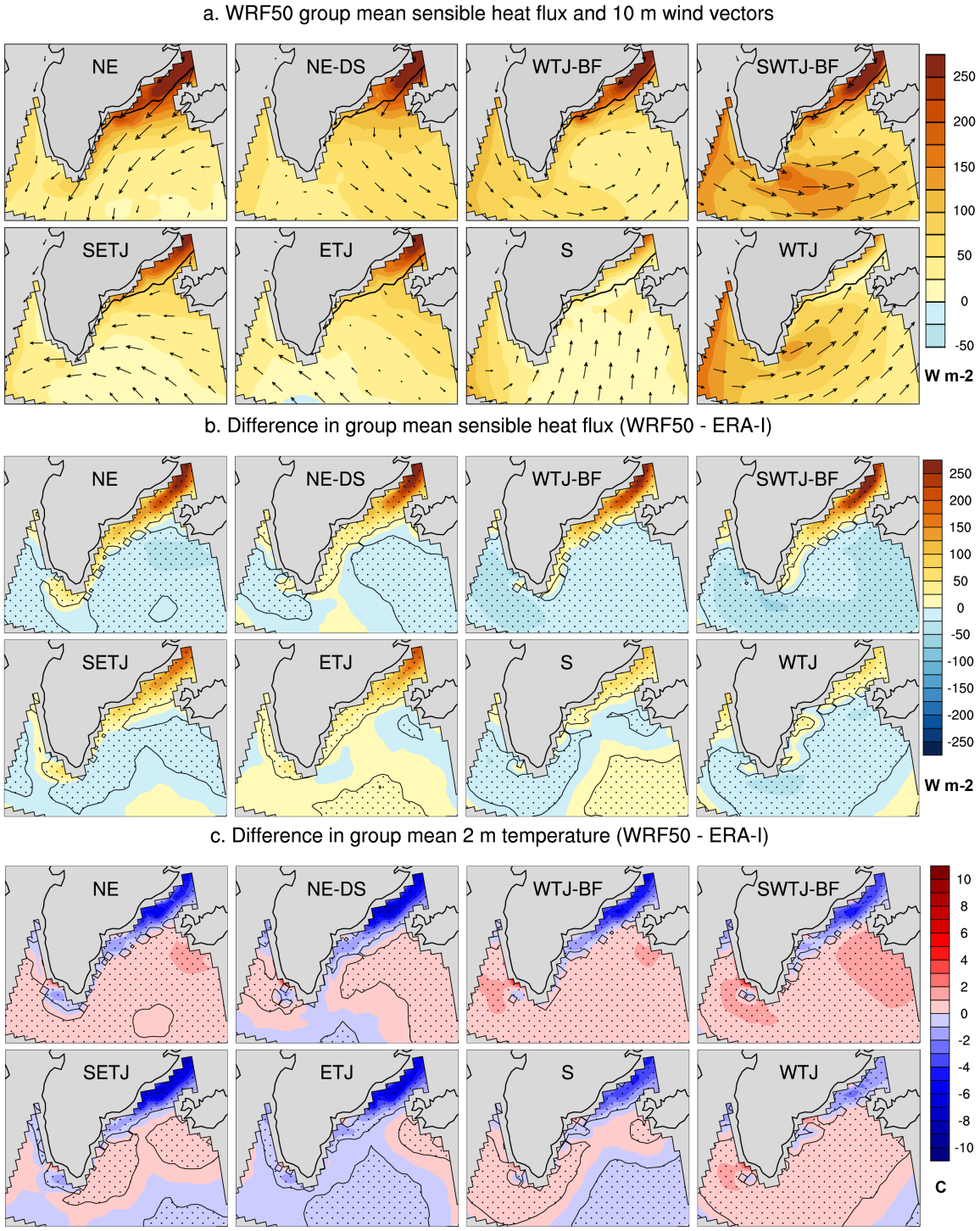

Supplementary Figure 5: Group (a) WRF sensible heat flux (W m^{-2}) and wind vectors, (b) difference in WRF and ERA-I sensible heat flux, and (c) WRF and ERA-I 2 m temperature difference (°C). The dark black contour on the mean figures is the 15% sea ice concentration line and the MIZ is located between the 15% sea ice contour and the Greenland coast. Stippling on the difference figures indicates areas with statistically significant difference between the two datasets at the 95% confidence level.

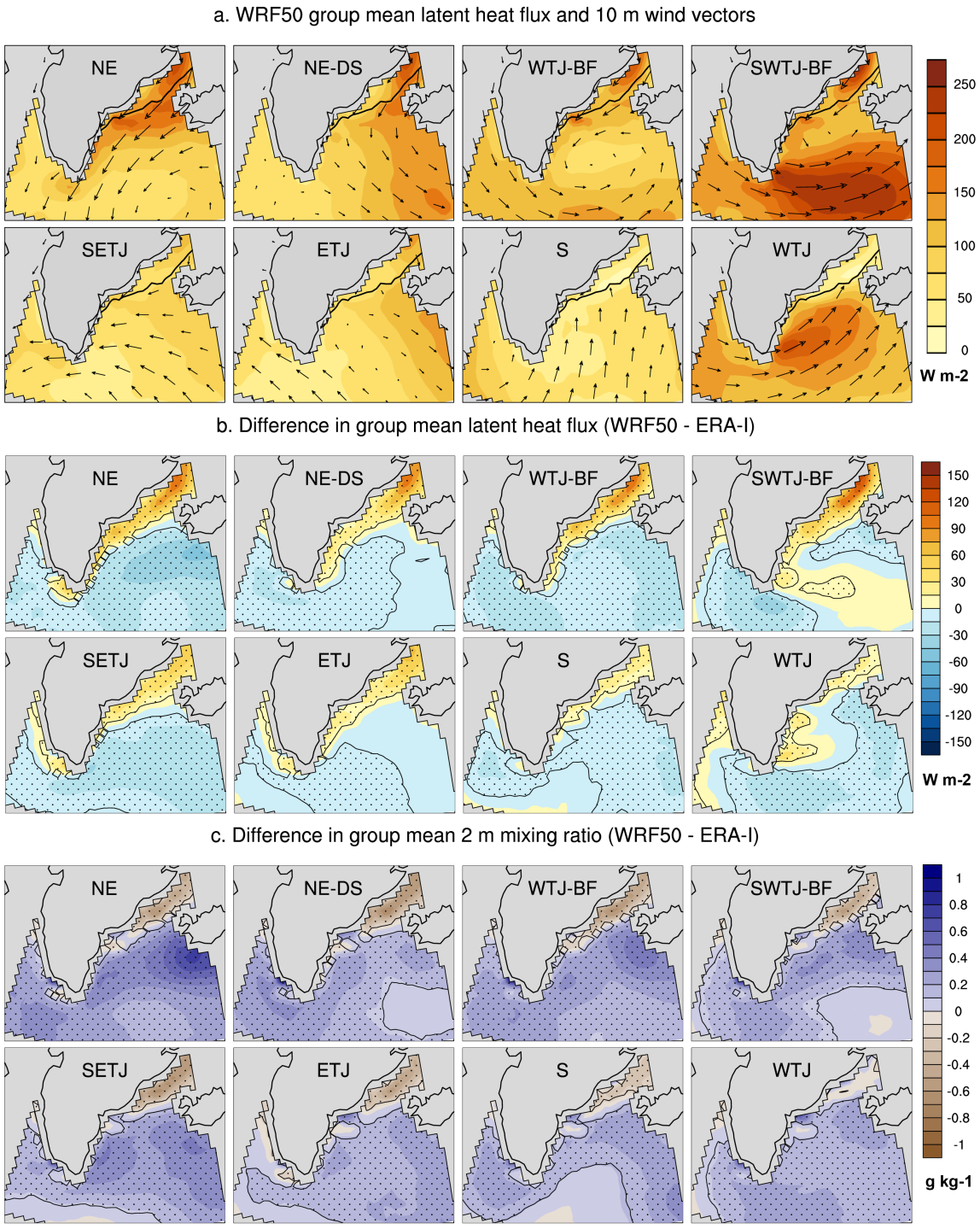

Supplementary Figure 6: Group (a) WRF latent heat flux (W m^{-2}) and wind vectors, (b) difference in WRF and ERA-I latent heat flux, and (c) WRF and ERA-I 2 m mixing ratio difference (g kg^{-1}). The dark black contour on the mean figures is the 15% sea ice concentration line and the MIZ is located between the 15% sea ice contour and the Greenland coast. Stippling on the difference figures indicates areas with statistically significant difference between the two datasets at the 95% confidence level.

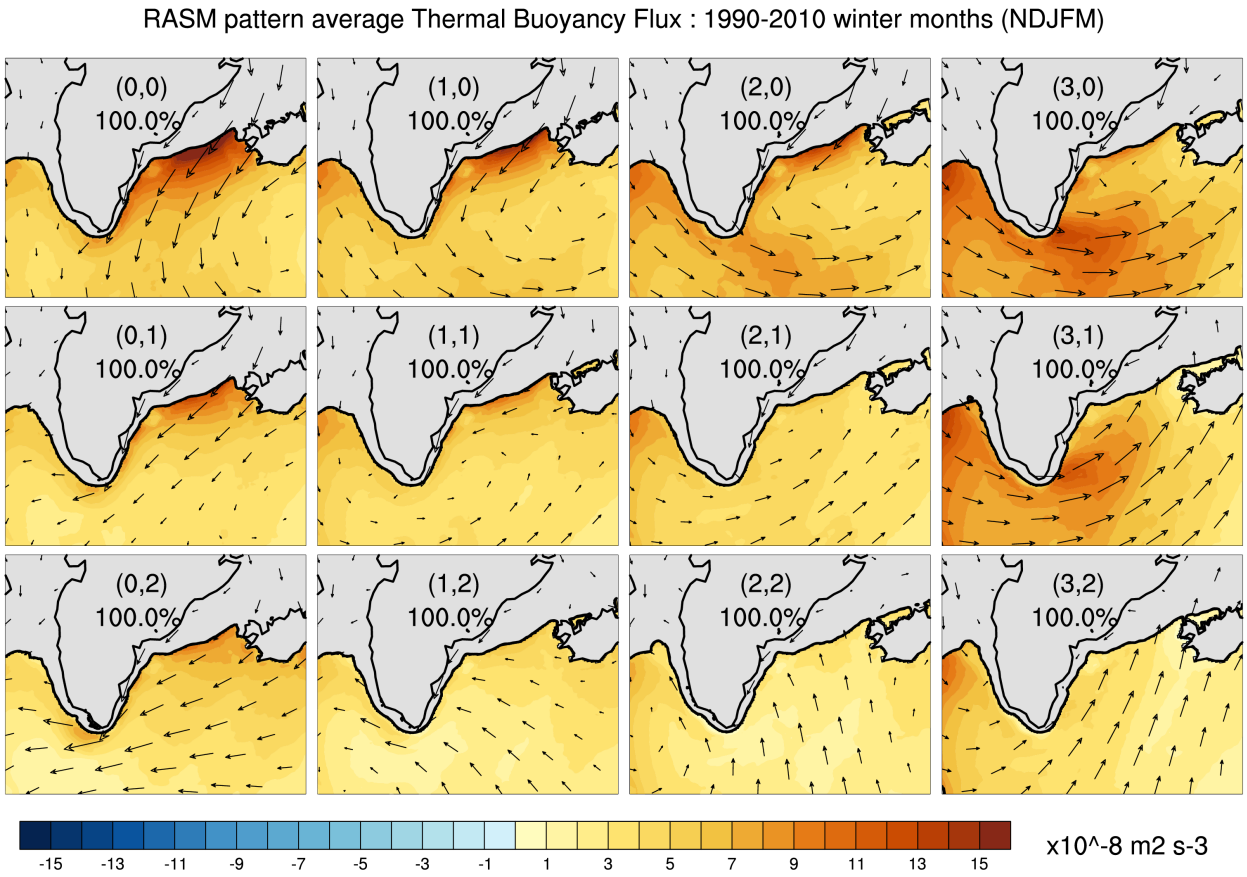

Supplementary Figure 7: Composite thermal term contribution to the buoyancy flux (m^2 s^{-3}) for each of the 12 representative wintertime wind patterns identified by the SOM. Percentages on each pattern are the percent contribution of each pattern to the total buoyancy flux for that pattern (Figure 3) and can be found in Table 1. The wind vectors are included to remind readers of the representative wind field, and the dark black contour represents the average 15% sea ice contour predicted by CICE in RASM for each pattern.

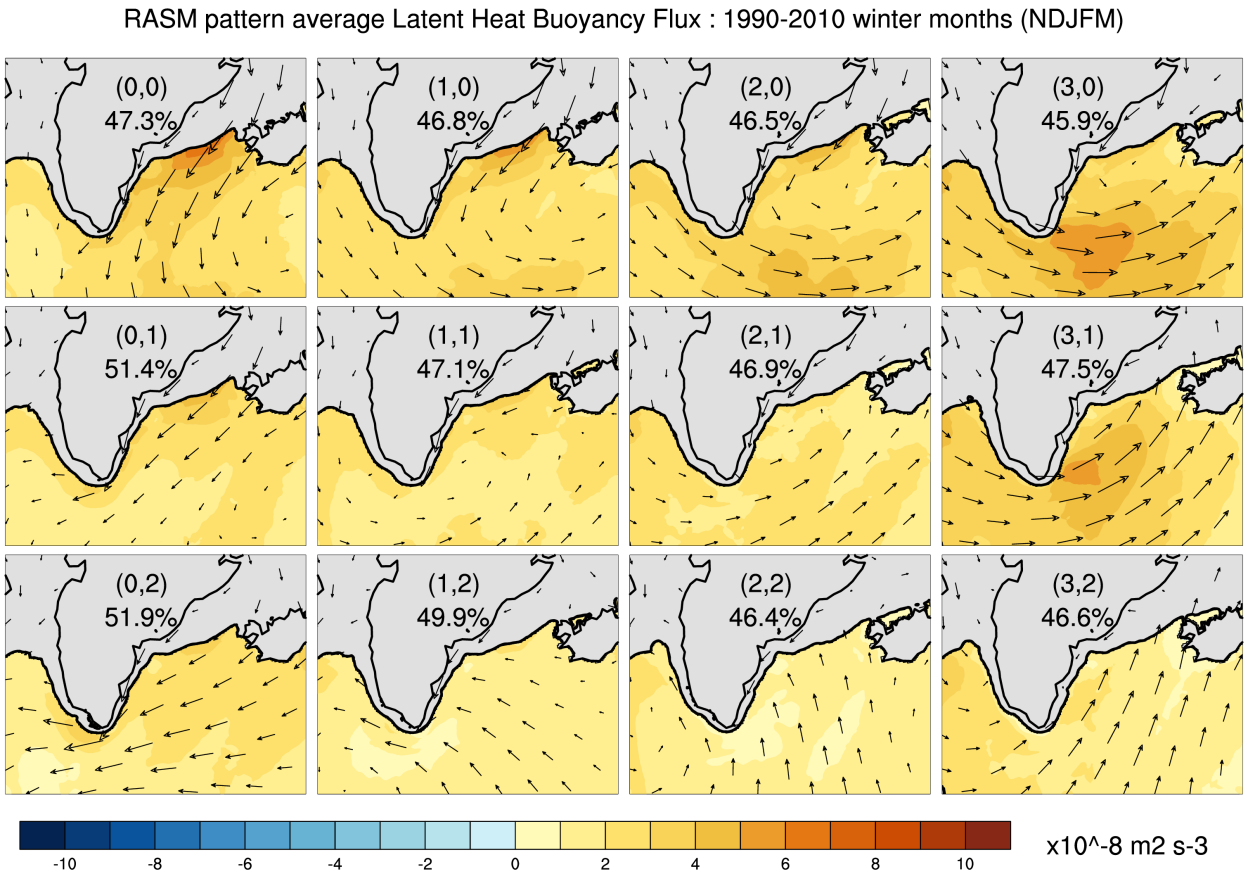

Supplementary Figure 8: Composite latent heat flux term contribution to the buoyancy flux (m^2 s^{-3}) for each of the 12 representative wintertime wind patterns identified by the SOM. Percentages on each pattern are the percent contribution of each pattern to the total thermal term for that pattern (Supplementary Figure 1) and can be found in Table 1. The wind vectors are included to remind readers of the representative wind field, and the dark black contour represents the average 15% sea ice contour predicted by CICE in RASM for each pattern.

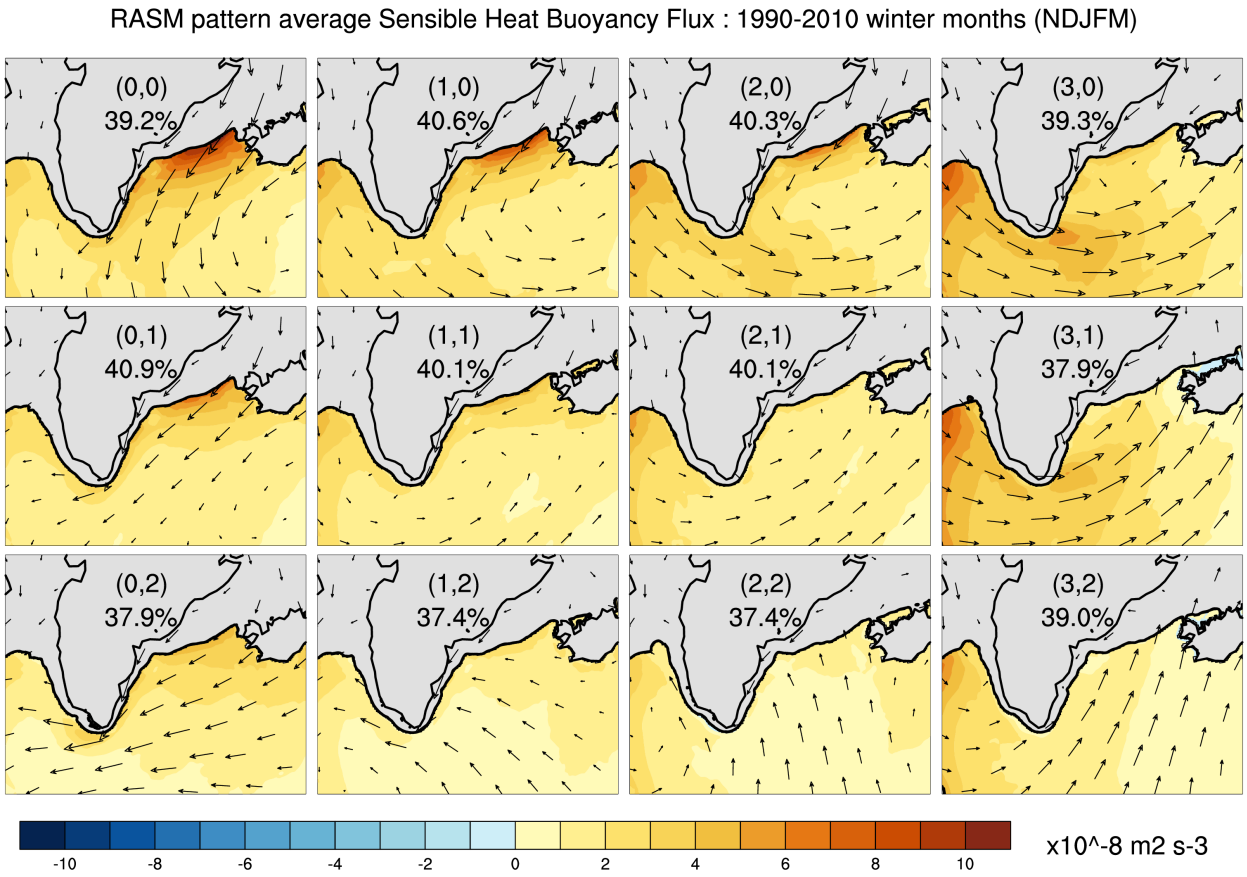

Supplementary Figure 9: Composite sensible heat flux term contribution to the buoyancy flux (m^2 s^{-3}) for each of the 12 representative wintertime wind patterns identified by the SOM. Percentages on each pattern are the percent contribution of each pattern to the total thermal term for that pattern (Supplementary Figure 1) and can be found in Table 1. The wind vectors are included to remind readers of the representative wind field, and the dark black contour represents the average 15% sea ice contour predicted by CICE in RASM for each pattern.

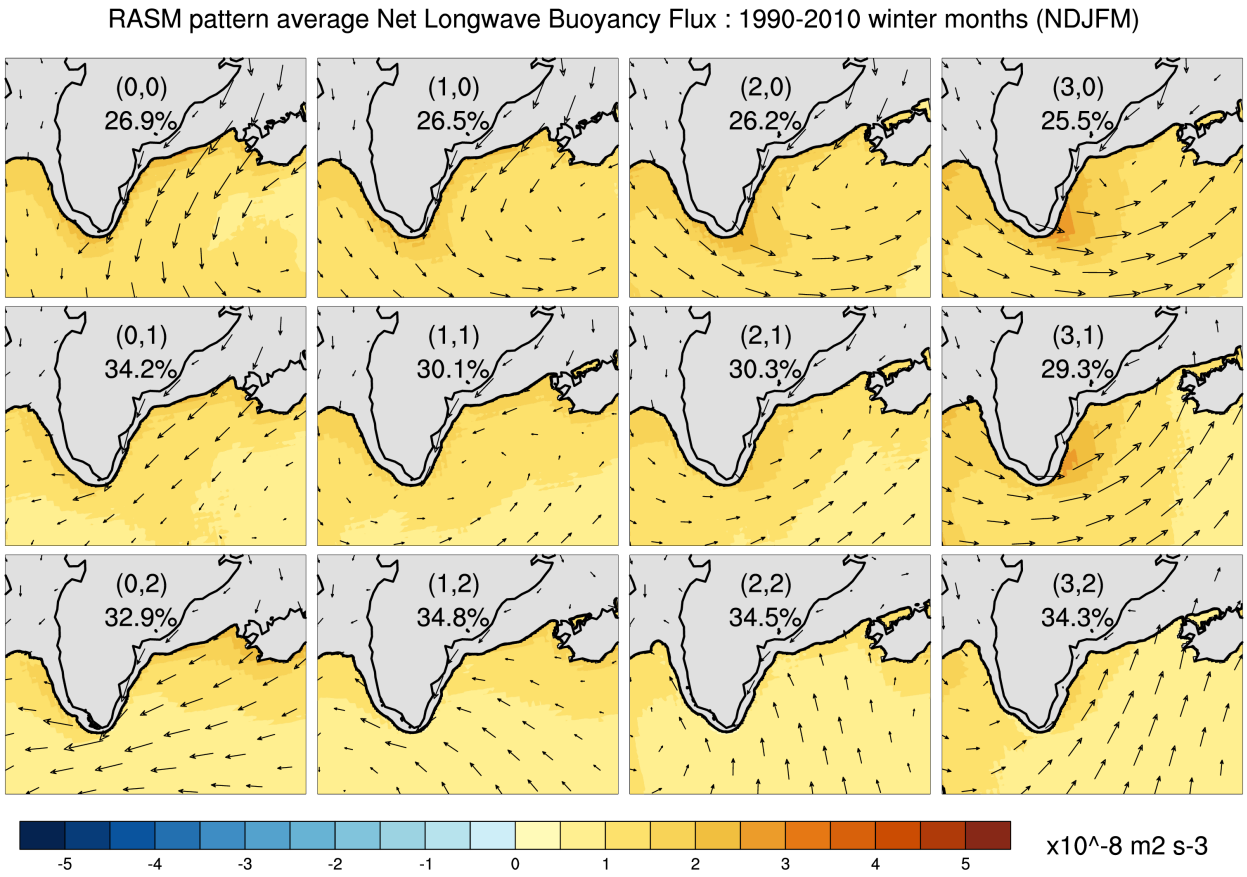

Supplementary Figure 10: Composite net longwave term contribution to the buoyancy flux (m^2 s^{-3}) for each of the 12 representative wintertime wind patterns identified by the SOM. Percentages on each pattern are the percent contribution of each pattern to the total thermal term for that pattern (Supplementary Figure 1) and can be found in Table 1. The wind vectors are included to remind readers of the representative wind field, and the dark black contour represents the average 15% sea ice contour predicted by CICE in RASM for each pattern.

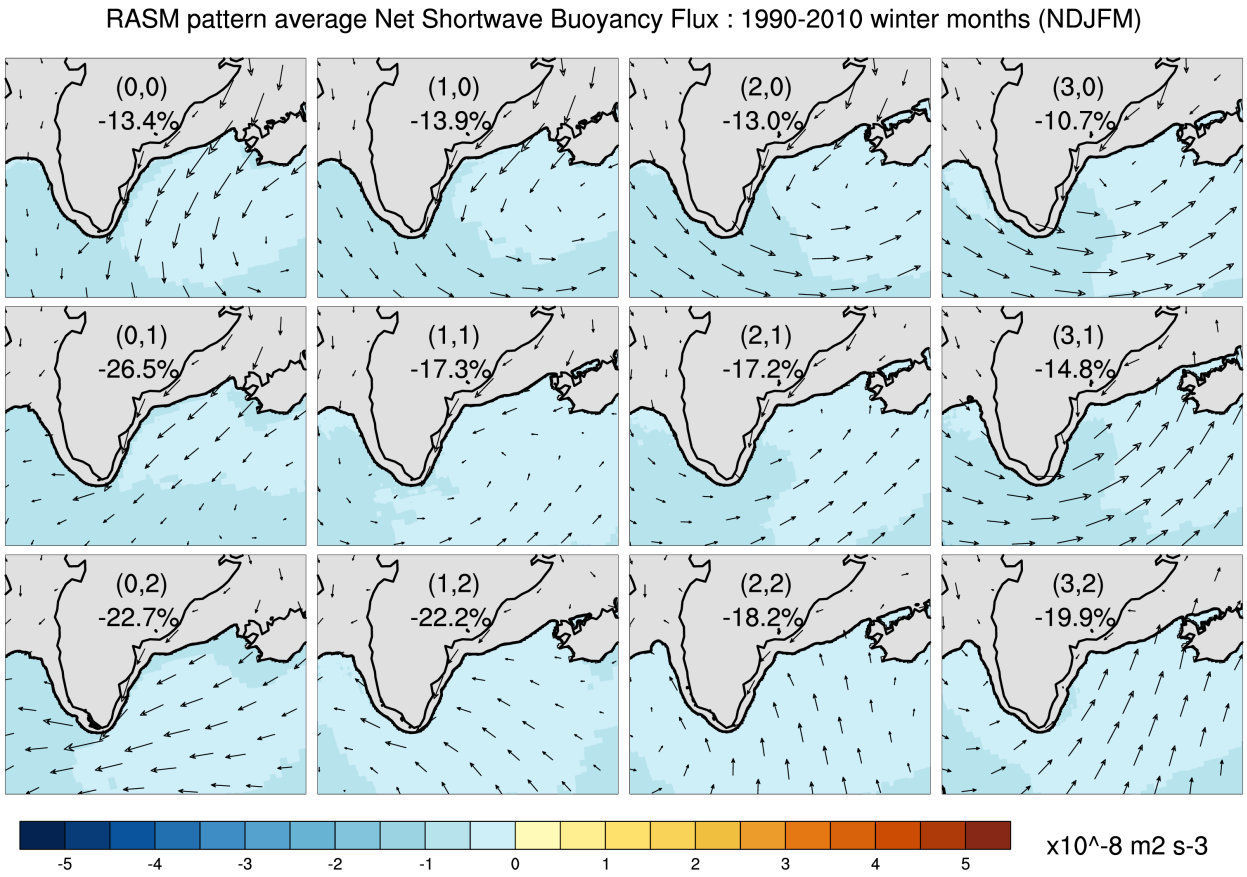

Supplementary Figure 11: Composite net shortwave term contribution to the buoyancy flux (m^2 s^{-3}) for each of the 12 representative wintertime wind patterns identified by the SOM. Percentages on each pattern are the percent contribution of each pattern to the total thermal term for that pattern (Supplementary Figure 1) and can be found in Table 1. The wind vectors are included to remind readers of the representative wind field, and the dark black contour represents the average 15% sea ice contour predicted by CICE in RASM for each pattern.

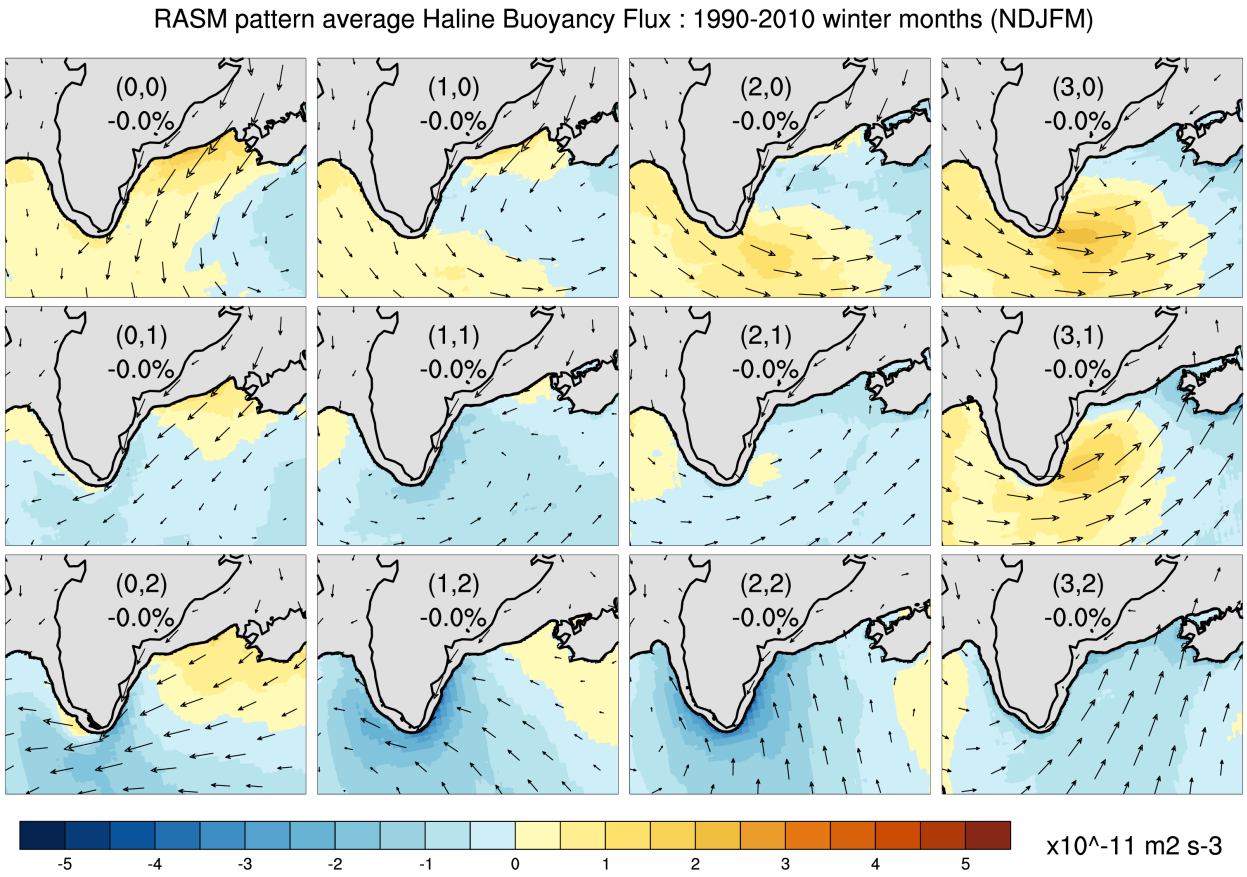

Supplementary Figure 12: Composite haline term contribution to the buoyancy flux (m^2 s^{-3}) for each of the 12 representative wintertime wind patterns identified by the SOM. Note that the color bar is three orders of magnitude smaller than for the thermal terms. Percentages on each pattern are the percent contribution of each pattern to the total buoyancy flux for that pattern (Figure 3) and can be found in Table 1. The wind vectors are included to remind readers of the representative wind field, and the dark black contour represents the average 15% sea ice contour predicted by CICE in RASM for each pattern.

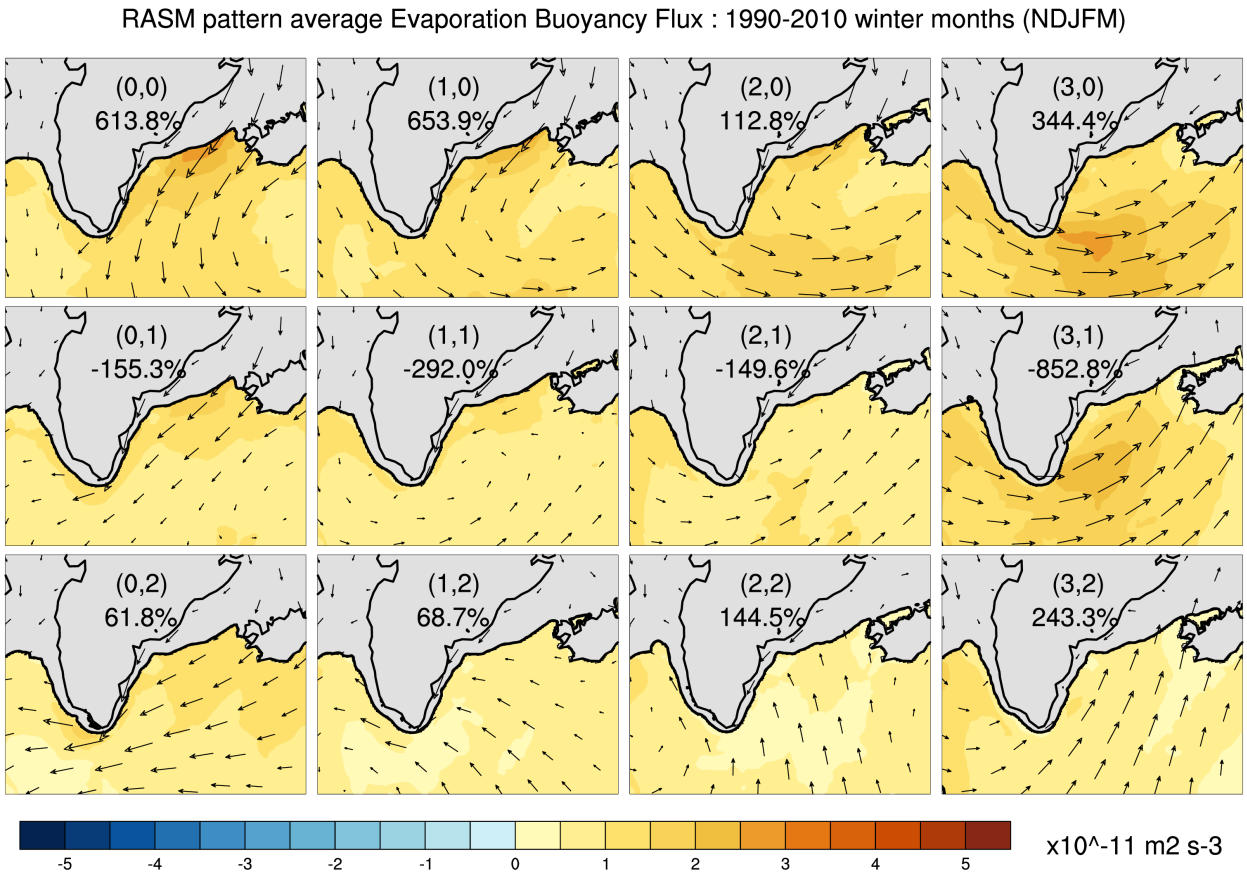

Supplementary Figure 13: Composite evaporation term contribution to the buoyancy flux (m^2 s^{-3}) for each of the 12 representative wintertime wind patterns identified by the SOM. Note that the color bar is three orders of magnitude smaller than for the thermal terms. Percentages on each pattern are the percent contribution of each pattern to the total haline term for that pattern (Supplementary Figure 6) and can be found in Table 1. The wind vectors are included to remind readers of the representative wind field, and the dark black contour represents the average 15% sea ice contour predicted by CICE in RASM for each pattern.

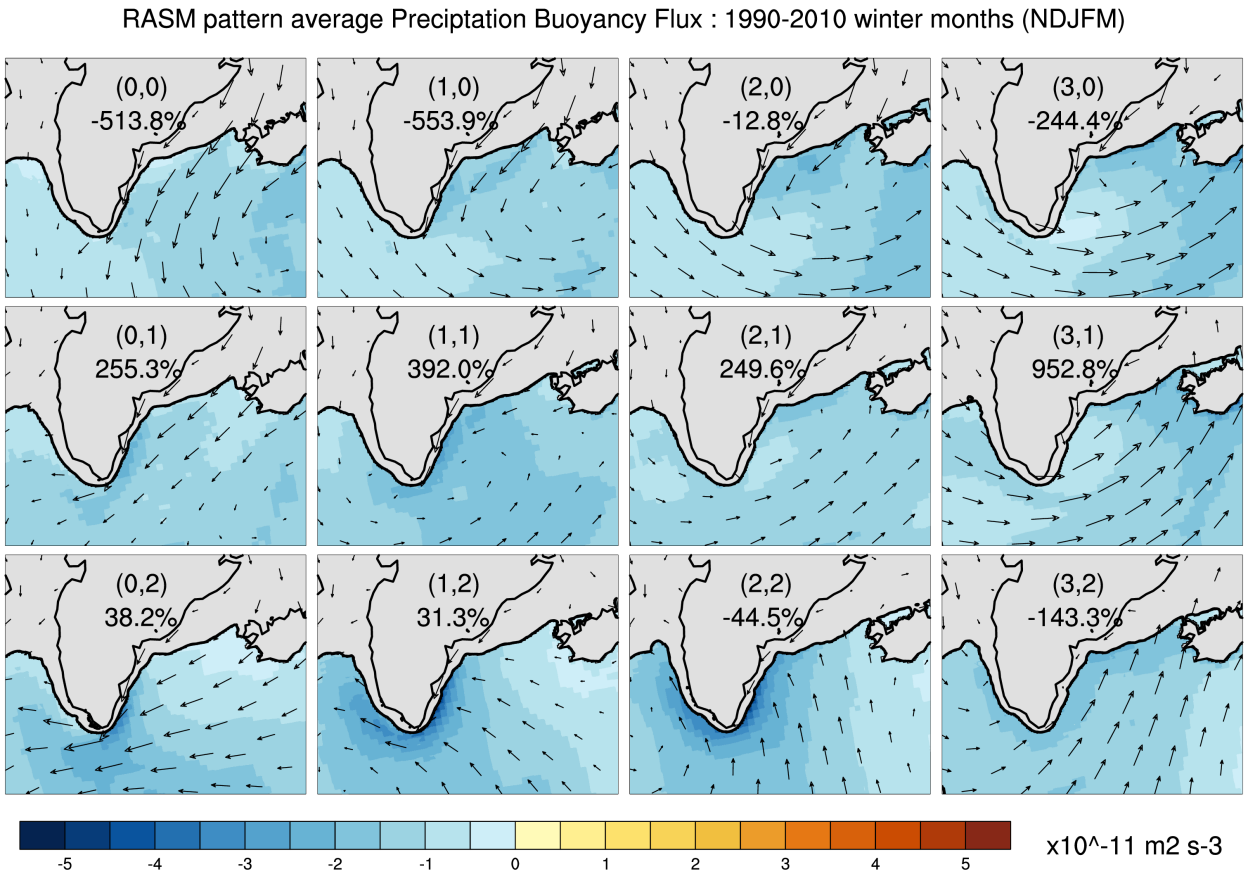

Supplementary Figure 14: Composite precipitation term contribution to the buoyancy flux (m^2 s^{-3}) for each of the 12 representative wintertime wind patterns identified by the SOM. Note that the color bar is three orders of magnitude smaller than for the thermal terms. Percentages on each pattern are the percent contribution of each pattern to the total haline term for that pattern (Supplementary Figure 6) and can be found in Table 1. The wind vectors are included to remind readers of the representative wind field, and the dark black contour represents the average 15% sea ice contour predicted by CICE in RASM for each pattern.

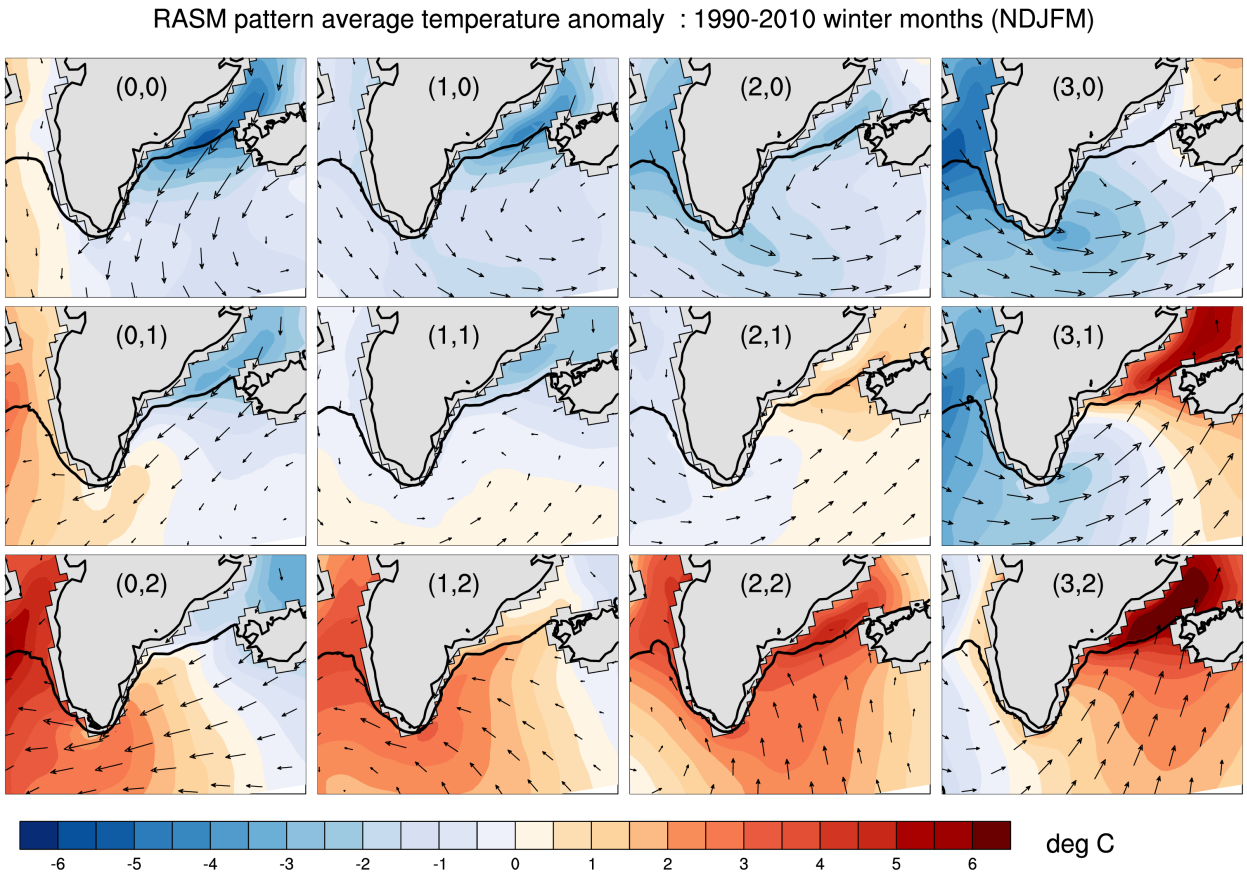

Supplementary Figure 15: Composite lowest model level (~12 m) atmospheric temperature anomaly (°C) for each of the 12 representative wintertime wind patterns identified by the SOM. The wind vectors are included to remind readers of the representative wind field, and the dark black contour represents the average 15% sea ice contour predicted by CICE in RASM for each pattern.

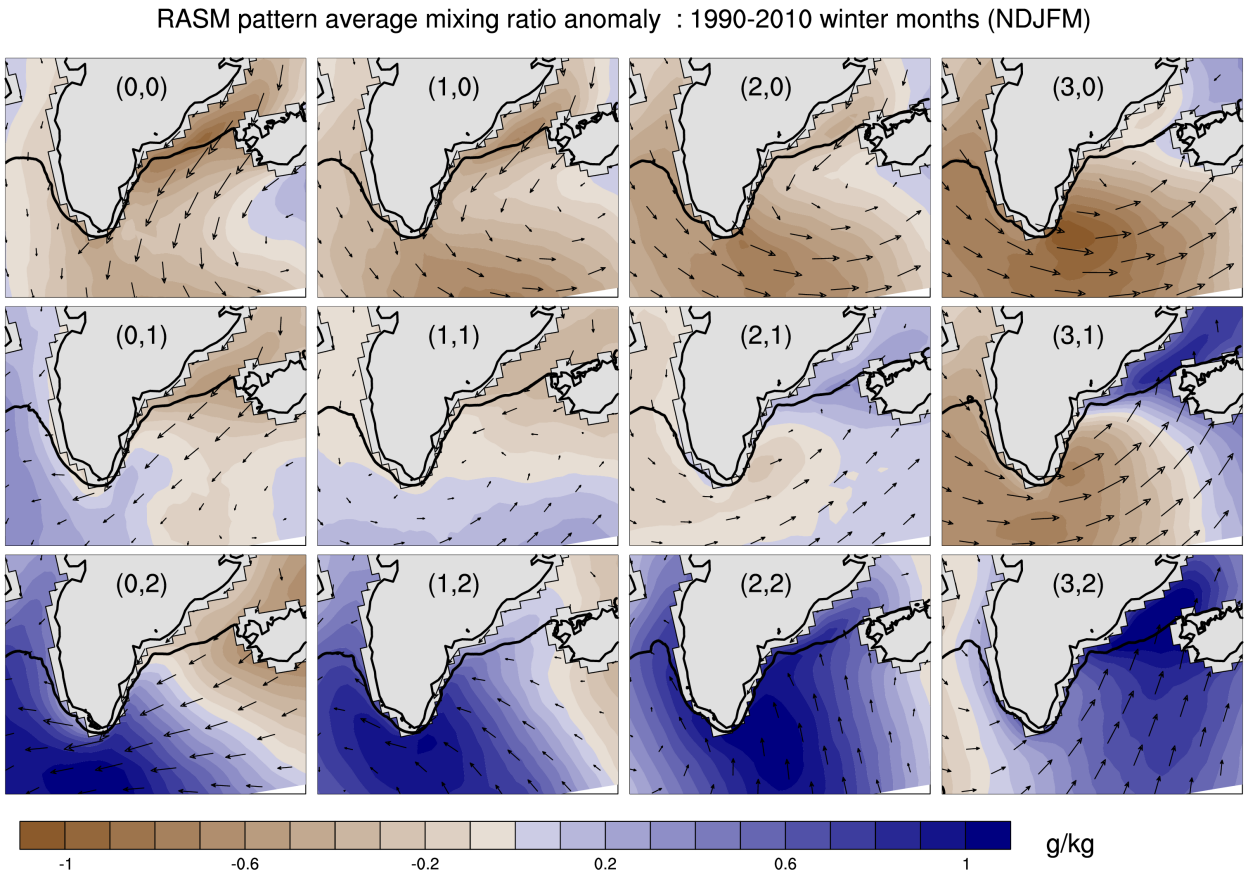

Supplementary Figure 16: Composite lowest model level (~12 m) atmospheric moisture anomaly (g kg^{-1}) for each of the 12 representative wintertime wind patterns identified by the SOM. The wind vectors are included to remind readers of the representative wind field, and the dark black contour represents the average 15% sea ice contour predicted by CICE in RASM for each pattern.

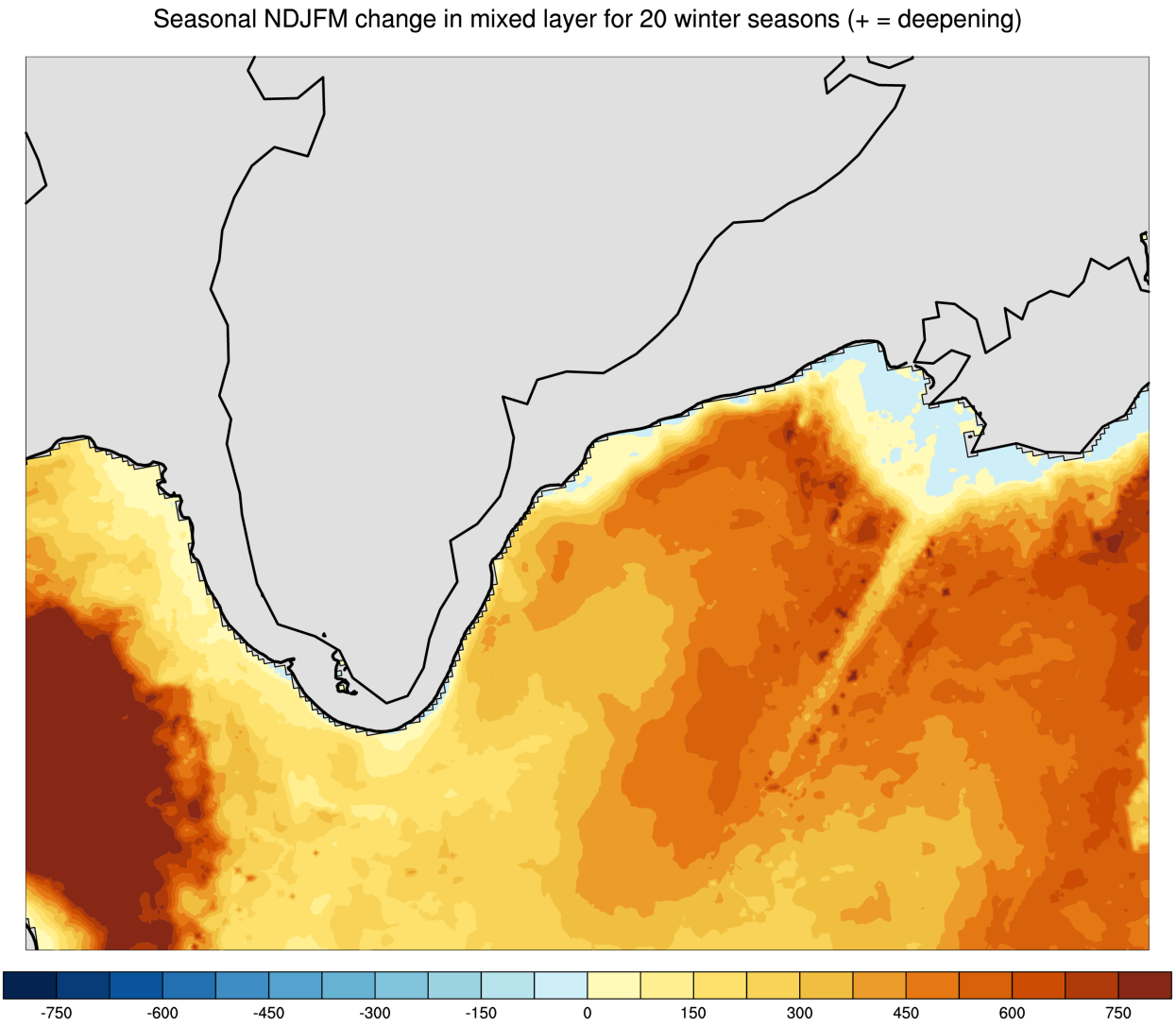

Supplementary Figure 17: 1990-2010 mean change in mixed layer depth from November 1 to March 31. Positive values indicate mixed layer deepening. The dark black contour represents the average 15% sea ice contour predicted by CICE.